

AD-A137 610

SPECTROSCOPIC EVALUATION OF ND(3+): CAMGAR AND
HO(3+): YLF AS 094 MICROMETERS LASERS(U) MASSACHUSETTS
INST OF TECH CAMBRIDGE A LINZ ET AL. 12 DEC 83

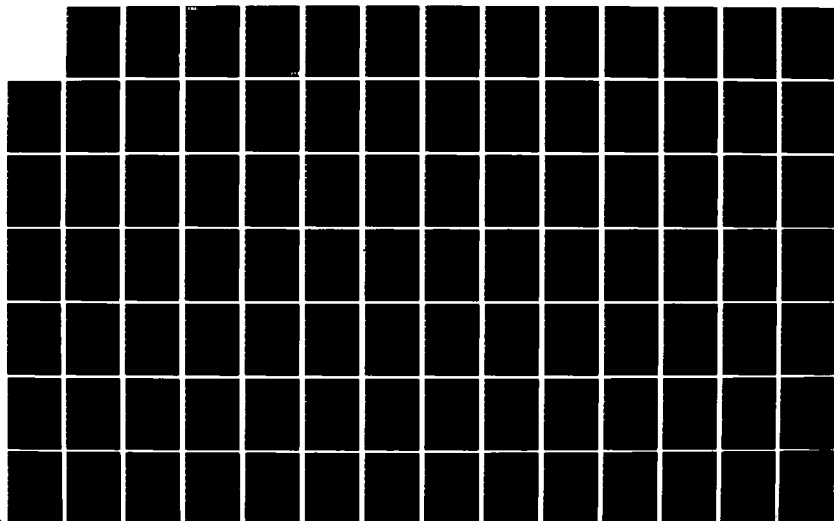
1/2

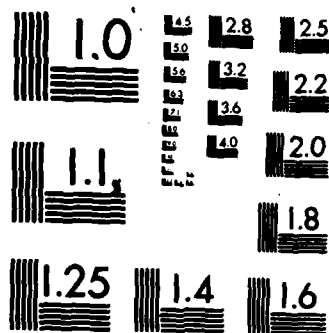
UNCLASSIFIED

OSP86111 N00014-78-C-0133

F/G 20/5

NL





MICROCOPY RESOLUTION TEST CHART
NATIONAL BUREAU OF STANDARDS-1963-A

2

MASSACHUSETTS INSTITUTE OF TECHNOLOGY

DEPARTMENT OF ELECTRICAL ENGINEERING AND COMPUTER SCIENCE
CENTER FOR MATERIALS SCIENCE AND ENGINEERING

Crystal Physics and Optical Electronics Laboratory

Cambridge, Massachusetts 02139

SPECTROSCOPIC EVALUATION OF Nd^{3+} :CAMGAR and Ho^{3+} :YLF AS
0.94 μm LASERS

BY

A. LINZ and H. P. JENSSEN

FINAL REPORT

Department of the Navy
Office of Naval Research
Boston
Massachusetts 02210

Scientific Officer: Dr. Matthew White
Contract Number: OSP 86111, N00014-78-C-0133
Date of Contract: December 1, 1977
Project Supervisor: Dr. A. Linz
(617) 253-3208, Rm. 13-3154

FEB 7 1984

A

This document has been classified for public release and a review of its contents is being conducted.

DTIC FILE COPY

83 12 16 093

UNCLASSIFIED

SECURITY CLASSIFICATION OF THIS PAGE (When Data Entered)

REPORT DOCUMENTATION PAGE		READ INSTRUCTIONS BEFORE COMPLETING FORM
1. REPORT NUMBER N00014-78-C-0133	2. GOVT ACCESSION NO.	3. RECIPIENT'S CATALOG NUMBER
4. TITLE (and Subtitle) Spectroscopic Evaluation of Nd ³⁺ :CAMGAR and Ho ³⁺ :YLF as 0.94 μ m Lasers		5. TYPE OF REPORT & PERIOD COVERED Final Report
		6. PERFORMING ORG. REPORT NUMBER OSP86111
7. AUTHOR(s) A. Linz & H. P. Jenssen		8. CONTRACT OR GRANT NUMBER(s) same as #1
9. PERFORMING ORGANIZATION NAME AND ADDRESS Massachusetts Institute of Technology Dept. of Electrical Engineering & Computer Science Crystal Physics & Optical Electronics Laboratory		10. PROGRAM ELEMENT, PROJECT, TASK AREA & WORK UNIT NUMBERS
11. CONTROLLING OFFICE NAME AND ADDRESS Office of Naval Research 495 Summer Street Boston, MA 02210		12. REPORT DATE December 12, 1983
		13. NUMBER OF PAGES 20 + 101
14. MONITORING AGENCY NAME & ADDRESS (if different from Controlling Office)		15. SECURITY CLASS. (of this report) Unclassified
		15a. DECLASSIFICATION/DOWNGRADING SCHEDULE
16. DISTRIBUTION STATEMENT (of this Report) Scientific Officer - 1/0; ONR Branch Office - 1/0; ACO - 1/0; NRL Code 2627 - 1/0; ONR Code 1021P - 6/0; DDC - 2/0 This document has been approved for public release and sale; its distribution is unlimited.		
17. DISTRIBUTION STATEMENT (of the abstract entered in Block 20, if different from Report)		
18. SUPPLEMENTARY NOTES FEB 7 1984		
19. KEY WORDS (Continue on reverse side if necessary and identify by block number) 0.94 μ m Laser Nd:CAMGAR Ho:YLF 480 nm laser stimulated emission coefficient (micrometer) (3+)		
20. ABSTRACT (Continue on reverse side if necessary and identify by block number) An efficient laser operating near the 0.94 μ m wavelength is of interest because with frequency doubling one can have a 470 nm laser with potentially higher overall efficiency than any primary laser at this wavelength. Nd ³⁺ in most oxide garnet host crystals has a 0.94 μ m transition. What is required for 0.94 μ m transition and a large branching ratio of 0.94 μ m emission relative to the 1.06 μ m emission. Detailed spectroscopy was performed on Nd:CAMGAR in order to determine the relevant cross sections. The results show that the 1.06 μ m cross section in CAMGAR is about 0.25 of the		

20 (continued) → the 1.06 μm cross section in YAG whereas the ratio of the 0.94 μm cross sections is 0.5. Laser experiments on both Nd:YAG and Nd:CAMGAR by longitudinal pumping with an Ar laser substantially verified the relative cross sections of the two materials. The 0.94 μm results were limited however and the resulting cross section for Nd:CAMGAR is higher than the spectroscopically determined value.

(3+)

5I7 level

ϵ_{3+} is an alternate ion for a 0.94 μm laser. The Ho 5F_5 to 5I_7 has been reported lased at 0.9 μm both in 2% in LiYF₄ and in LiHoF₄. An analysis of Ho:YLF has been done to evaluate its potential as a useful laser material. Even though the transition is apparently a four level transition (the terminal level being at 5000 cm^{-1}), the terminal level has a long fluorescent lifetime and is also efficiently pumped simultaneously with the upper 5F_5 level, severely limiting the usefulness of this laser material.



letter in file

A1

EVALUATION OF LASER MATERIALS FOR 0.94 μ m OPERATION

1. Introduction and Summary

An efficient laser operating near the 0.94 μ m wavelength is of interest because with frequency doubling one can have a 470 nm laser with potentially higher overall efficiency than any primary laser at this wavelength. The requirements for the 0.94 μ m laser material are that it can be efficiently pumped, that it has a four level laser transition and that the host crystal is capable of handling high average power.

Nd³⁺ in most oxide garnet host crystals has a 0.94 μ m transition. The terminal level for this transition is the upper level of the ground manifold, $^4I_{9/2}$, at about 800 cm⁻¹ or 4kT at room temperature. This is generally not enough to satisfy the conditions for a four level laser in that the main contribution to the threshold is overcoming the terminal level population. In Nd:YAG for example the necessary upper level population to yield $\Delta N=0$ for the 0.94 μ m transition is high enough to make it difficult to prevent the high gain 1.06 μ m transition from lasing. What is required for 0.94 μ m lasing is a low stimulated emission cross section for the 1.06 μ m transition and a large branching ratio of 0.94 μ m emission relative to the 1.06 μ m emission. That the 0.94 μ m cross section also would be lower than in YAG is of less importance as long as the thermal population is the main contributor to the threshold. It was on the basis of these considerations that the garnet CAMGAR (CaY₂Mg₂Ge₃O₁₂) was chosen as a candidate for investigation. Detailed spectroscopy was performed on Nd:CAMGAR in order to determine the relevant

cross sections. The results show that the 1.06 μm cross section in CAMGAR is about 0.25 of the 1.06 μm cross section in YAG whereas the ratio of the 0.94 μm cross sections is 0.5. Section II of this report describes in detail the spectroscopy and analysis of Nd:CAMGAR.

Laser experiments on both Nd:YAG and Nd:CAMGAR by longitudinal pumping with an Ar laser substantially verified the relative cross sections of the two materials. The 0.94 μm results were limited however and the resulting cross section for Nd:CAMGAR is higher than the spectroscopically determined value. The details of the experimental laser work are presented in the form of a thesis as an appendix. Ho^{3+} is an alternate ion for a 0.94 μm laser. The $\text{Ho } ^5\text{F}_5$ to $^5\text{I}_7$ has been reported lased at 0.98 μm both in 2% in LiYF_4 and in LiHoF_4 . An analysis of Ho:YLF has been done to evaluate its potential as a useful laser material. Even though the transition is apparently a four level transition (the terminal level being at 5000 cm^{-1}), the terminal level has a long fluorescent lifetime and is also efficiently pumped simultaneously with the upper $^5\text{F}_5$ level. This severely limits the usefulness of this laser material. Details of the analysis are given in Section 3.

2.1. Determination of the $^4F_{3/2}$, $^4I_{15/2}$ and $^4I_{13/2}$ energy levels from absorption

A 5.6 mm thick sample of Nd:CAMGAR was cooled to liquid nitrogen temperature (77°K). The infrared optical absorption lines were measured using a Cary 14 spectrophotometer in the 0.8 - 2.6 μm range. Absorption from the ground state revealed the locations of the $^4F_{3/2}$, $^4I_{15/2}$, and $^4I_{13/2}$ energy levels of the trivalent dopant. Figure 1 depicts these levels. Many groups of strong absorption lines were observed above the $^4F_{3/2}$. The wavelengths for the $^4F_{3/2}$ levels were calibrated by comparison to known Nd:YAG lines.

2.2. Determination of the $^4I_{9/2}$, $^4I_{11/2}$ energy levels from emission

A room temperature sample of Nd:CAMGAR was pumped with a 0.5145 μm argon laser. The spectrum of the emitted light was measured with a Model 218 McPherson scanning monochromator which uses a rotating diffraction grating to scan through the frequency ranges of interest. A photomultiplier was used as a detector of spectral intensity. Wavelength calibration was implemented by detecting a known line from a mercury arc source. Computer analysis normalized the data by dividing out the measured spectral response of the grating and photomultiplier.

The measured emission lines in Nd^{+3} for 0.8 to 1.2 μm come from transitions from the $^4F_{3/2}$ levels (R_1 and R_2) to the $^4I_{9/2}$ and $^4I_{11/2}$ levels. By subtracting the energies of the emitted photons from the energies of the initial states (R_1 and R_2), two sets of figures were obtained for the energies of the terminal levels. In cases where discrepancies existed, it was noted that some of the emission lines

overlapped, creating some uncertainty as to their exact peak wavelengths. Therefore the terminal levels in doubt were determined by using only the emission lines that were less affected by overlap.

There has been some confusion in the determination of the four lowest levels of the $^4I_{11/2}$ multiplet arising from the difficulty in deciding whether the initial level for a given transition is R_1 or R_2 . Sharp, Miller and Horowitz¹ of the Night Vision Laboratory at Fort Belvoir, Virginia, assumed that the $R_1 \rightarrow Y_4$ and $R_2 \rightarrow Y_3$ transitions were too weak to be seen and attributed the strong $1.059 \mu\text{m}$ line solely to an $R_1 \rightarrow Y_1$ transition. Table 1 lists the emission lines measured with the McPherson Monochromator along with the Sharp et al. interpretation, due to transitions to Y_1 , Y_2 , Y_3 , and Y_4 .

Table 1
 $^4F_{3/2} \rightarrow Y_1, Y_2, Y_3, Y_4$

Line No.	Sharp et al.	$\lambda_{\text{air}} (\mu\text{m})$	$\frac{1}{\lambda_{\text{air}}} (\text{cm}^{-1})$	$E (\text{cm}^{-1})$
1	$R_2 \rightarrow Y_1$	1.0470	9551.1	9548.5
2	$R_2 \rightarrow Y_2$	1.0532	9494.9	9492.3
3	$R_1 \rightarrow Y_1$	1.0590	9492.9	9440.3
4	$R_1 \rightarrow Y_2$	1.0658	9382.6	9380.1
5	$R_2 \rightarrow Y_4$	1.0718	9330.1	9327.5
6	$R_1 \rightarrow Y_3$	1.0776	9279.9	9277.3

The Sharp model shows two inconsistencies. R_1 and R_2 are known to be separated by 121 cm^{-1} . Yet lines 1 and 3 show only 108 cm^{-1} separation and 2 and 4 show only 112 cm^{-1} separation, which is not accountable for by experimental errors. In addition, the Sharp interpreta-

tion of lines 5 and 6 is arbitrary and impossible to verify with room temperature data.

In order to resolve the issue, emission from the sample was measured at liquid helium temperature so that only $R_1 \rightarrow {}^4I_{11/2}$ transitions were detectable. It was found that lines 1 and 2 disappeared completely. Lines 4, 5 and 6 were present with the same relative strength as at room temperature. Line 3 was still the most intense line, but only half as strong relative to 4, 5 and 6 as at room temperature. Neglecting the thermal shift in the energy of R_1 (which by comparison to YAG should be small), the energies of levels Y_1 through Y_4 at liquid helium temperature are 2002, 2059, 2109, and 2156 cm^{-1} , respectively. As in YAG, the shifts in these levels as the temperature approaches 300°K should be uniform and on the order of 10 cm^{-1} .

Table 2 depicts a more sensible interpretation of the room temperature data. The "wrong" energy spacing between lines 1 and 3 and between 2 and 4 can be explained by a shift in the $R_1 \rightarrow Y_1$ and $R_1 \rightarrow Y_2$

Table 2

${}^4F_{3/2} \rightarrow Y_1, Y_2, Y_3, Y_4$

<u>Line Number</u>	<u>Aull, Jenssen</u>
1	$R_2 \rightarrow Y_1$
2	$R_2 \rightarrow Y_2$
3	$R_1 \rightarrow Y_1, R_2 \rightarrow Y_3$
4	$R_1 \rightarrow Y_2, R_2 \rightarrow Y_4$
5	$R_1 \rightarrow Y_3$
6	$R_1 \rightarrow Y_4$

lines due to close overlap with the $R_2 \rightarrow Y_3$ and $R_2 \rightarrow Y_4$ lines, respectively. The energies of Y_1 through Y_4 are determined from lines 1, 2, 5 and 6 as 2013, 2069, 2115 and 2165, respectively. This shows a uniform upward shift of about 10 cm^{-1} with respect to the liquid helium temperature values.

Figure 1 also depicts the $^4I_{9/2}$ and $^4I_{11/2}$ levels. The energies shown for $^4F_{3/2}$ are averages between the values determined by emission to the ground state and those obtained by absorption. In each case these two figures were consistent to within experimental accuracy. Figure 2 is a computer generated plot of the emission spectrum of Nd:CAMGAR and Nd:YAG in the $0.8 - 1.1 \mu\text{m}$ range.

2.3. Determination of the neodymium concentration in the CAMGAR host crystal

The neodymium concentration in CAMGAR was determined by comparing with a calibration curve the optical absorbance at 575 nm of a hydrochloric acid solution of a weighed amount of sample.

One gram of CAMGAR crystal chips was dissolved in 12 ml of concentrated HCl at 150°C in a 25 ml Parr Teflon-lined pressure reactor. Thirty-six to forty-eight hours is required for complete reaction. Calcium, Mg and Y are converted to soluble chlorides, while Ge is converted to liquid GeCl_4 , insoluble in concentrated HCl. The GeCl_4 was separated by distillation from the concentrated HCl solution, leaving CaCl_2 , MgCl_2 and YCl_3 dissolved in roughly 6 M HCl. Evaporation was carried out by heating the Parr Teflon cup in a water bath. The Ge-free CAMGAR solution was then transferred to a 10 ml volumetric flask. Absorbance was measured in a 5 cm cell.

Calibration solutions were made up to contain about the same

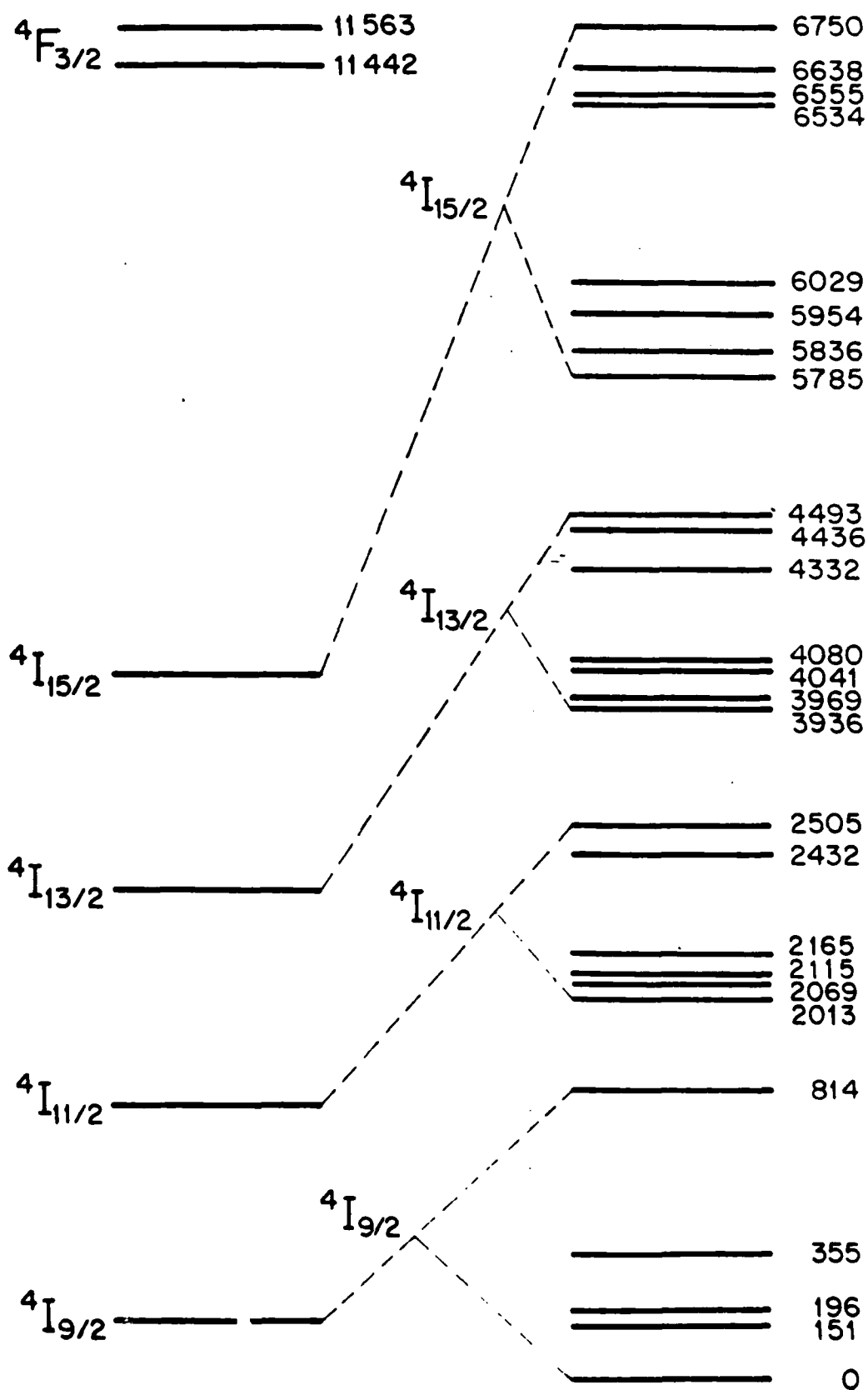
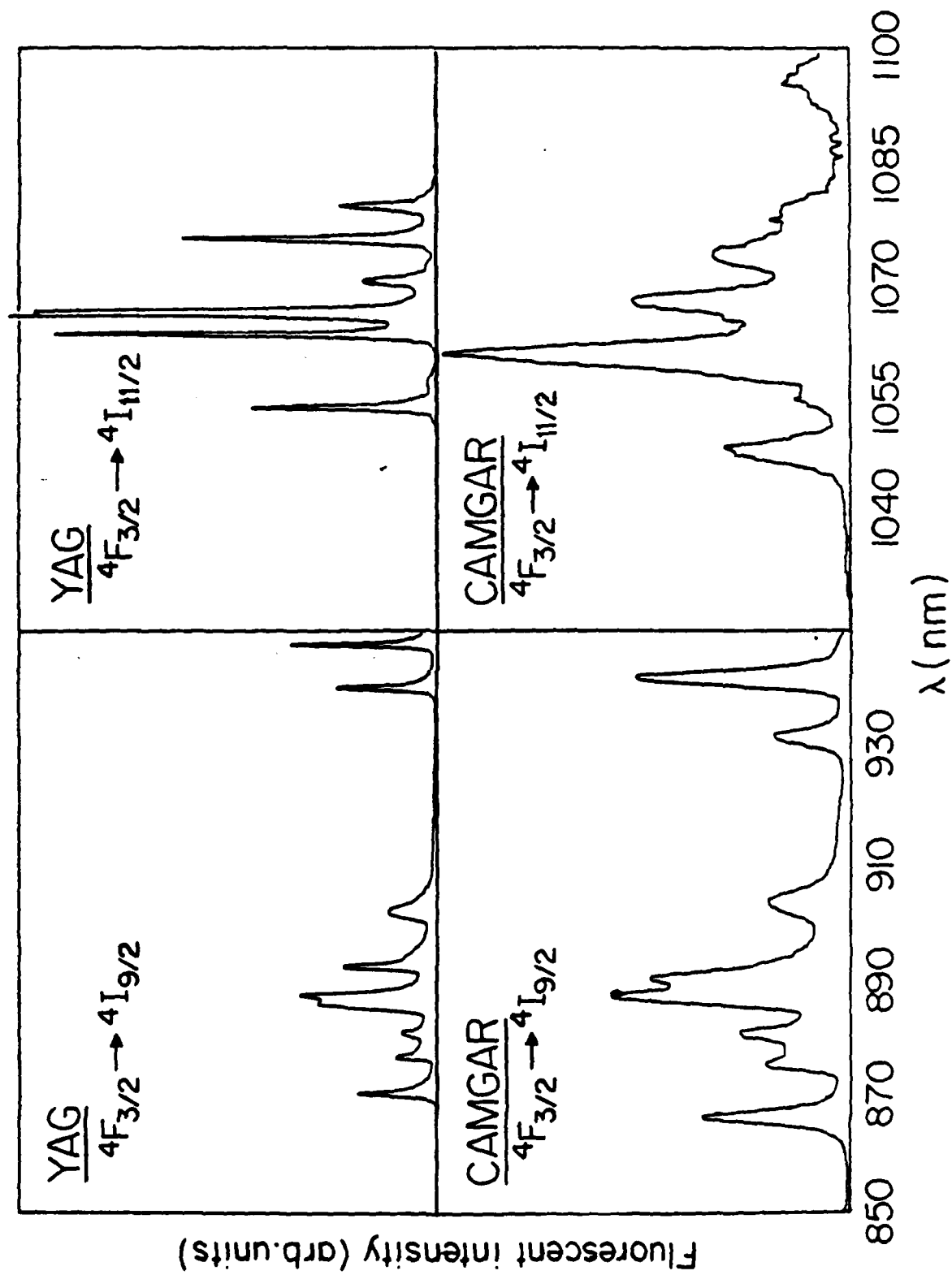


Fig. 1. Energy levels of Nd:CAMGAR.



concentration of HCl , CaCl_2 , MgCl_2 and YCl_3 as the unknown and accurately measured amounts of Nd chosen to bracket the unknown concentration. The absorbance of these solutions was also measured in a 5 cm cell. A calibration curve was then constructed from which the concentration of the unknown solution could be read. This in turn yields the weight of Nd_2O_3 in the sample. From the weight of the sample and Nd_2O_3 contained therein, the fraction of Y replaced by Nd was calculated.

The foregoing chemical analysis yielded a concentration of 2.236×10^{20} ions/cm³. This information is necessary to calculate absorption cross sections.

2.4. $^4\text{I}_{9/2} \rightarrow ^4\text{F}_{3/2}$ absorption cross sections

The Cary spectrophotometer was used to measure the peak absorption coefficients of a room temperature 5.6 mm sample of $\text{Nd}:\text{CAMGAR}$ in the 0.85 - 0.95 μm range. For each line the initial level in the $^4\text{I}_{9/2}$ group and the terminal $^4\text{F}_{3/2}$ level was identified. The cross section for each transition was calculated by dividing the peak absorption coefficient by the population of ions in the initial level. This population was calculated by multiplying the total concentration $[\text{Nd}^{+3}]$ by the appropriate normalized room temperature Boltzmann factor. Table 3 summarizes the results obtained.

Table 3

<u>Transition</u>	<u>$\lambda_{\text{air}} (\mu\text{m})$</u>	<u>$\sigma (10^{-20} \text{ cm}^2)$</u>
$Z_5 \rightarrow R_1$	0.9403	2.4
$Z_5 \rightarrow R_2$	0.9300	1.5
$Z_4 \rightarrow R_1$	0.9018	0.6
$Z_3 \rightarrow R_1$	0.8888	1.9
$Z_2 \rightarrow R_1$	0.8855	2.3
$Z_3 \rightarrow R_2$	0.8795	1.7
$Z_1 \rightarrow R_1$	0.8738	0.7
$Z_1 \rightarrow R_2$	0.8645	2.8

2.5. Stimulated emission cross sections and gains of the
1.0590 μm and 0.9403 μm laser transitions

The stimulated emission cross section of the 0.9403 μm transition ($R_1 \rightarrow Z_5$) is the same as its absorption cross section since these quantities are proportional to the Einstein B coefficients. The emission cross sections of two transitions from the same upper level are related by the formula

$$\frac{\sigma_1}{\sigma_2} = \frac{(dI/d\lambda)_1}{(dI/d\lambda)_2} \left(\frac{\lambda_1}{\lambda_2}\right)^5 \left(\frac{n_2}{n_1}\right)^2$$

where the σ_1 and σ_2 denote the peak cross sections, $(dI/d\lambda)_1$ and $(dI/d\lambda)_2$ denote relative peak intensities of the emission lines, and n_2/n_1 is the ratio of refractive indices at the wavelengths of emission, λ_2 and λ_1 .

If the cross section of one transition in the emission spectrum is already known from absorption data, the cross sections of other transitions from the same upper level can be determined from this formula.

Any such straightforward calculation of the 1.059 μm cross section

is impossible because this emission line is the sum of two closely overlapping lines ($R_1 \rightarrow Y_1$ and $R_2 \rightarrow Y_3$), and it must be determined what proportion of the emitted intensity comes from each transition. Because the lineshapes are not exactly Gaussian or exactly Lorentzian, mathematical curve-fitting was difficult and did not produce a close approximation to the data. Since the $1.059 \mu\text{m}$ line doubles in peak intensity with respect to other $R_1 \rightarrow {}^4I_{11/2}$ emission lines when the temperature is raised from 4°K to 300°K , it can be estimated that this emission at room temperature is due 50% to $R_1 \rightarrow Y_1$ and 50% to $R_2 \rightarrow Y_3$. The relative peak intensity of the $1.059 \mu\text{m}$ line was found to be 4.8, so a peak value of 2.4 is assigned to each of the two contributing transitions.

Table 4 lists the relative peak intensities of the ${}^4F_{3/2} \rightarrow {}^4I_{9/2}$ emission lines and the $R_1 \rightarrow Y_1$ and $R_2 \rightarrow Y_3$ lines. From the data in Tables 3 and 4, two figures for the $R_2 \rightarrow Y_3$ cross section and four for the

Table 4

<u>Transition</u>	<u>$\lambda_{\text{air}} (\mu\text{m})$</u>	<u>$dI/d\lambda$</u>
$R_2 \rightarrow Z_5$	0.9300	0.9
$R_2 \rightarrow Z_3$	0.8795	1.3
$R_2 \rightarrow Y_3$	1.0590	2.4
$R_1 \rightarrow Z_5$	0.9403	2.6
$R_1 \rightarrow Z_4$	0.9018	1.0
$R_1 \rightarrow Z_3$	0.8888	2.4
$R_1 \rightarrow Z_2$	0.8855	2.9
$R_1 \rightarrow Y_1$	1.0590	2.4

$R_1 \rightarrow Y_1$ cross section can be calculated, and each set of figures averaged. Data for transitions to Z_1 were not included in the analysis since the thermal population in Z_1 is large and a significant error in the value of $\frac{dI}{d\lambda}$ occurs due to reabsorption of the emitted light. The average values obtained for the emission cross sections are

$$\sigma_{R_1 \rightarrow Y_1} = 4.1 \times 10^{-20} \text{ cm}^2$$

$$\sigma_{R_2 \rightarrow Y_3} = 7.8 \times 10^{-20} \text{ cm}^2.$$

The emitted intensity for each line is proportional to the emission cross section and to the population in the upper level. At room temperature 64% of the $^4F_{3/2}$ population is in R_1 and 36% is in R_2 . This yields a weighted average for the effective cross section for $1.059 \mu\text{m}$ emission from the $^4F_{3/2}$ multiplet,

$$\begin{aligned} \sigma_{\text{eff}} &= [0.36 (7.8) + 0.64 (4.1)] \times 10^{-20} \text{ cm}^2 \\ &= 5.4 \times 10^{-20} \text{ cm}^2. \end{aligned}$$

Table 5 compares the $0.94 \mu\text{m}$ and $1.06 \mu\text{m}$ cross sections in CAMGAR to those obtained for YAG. These are effective cross sections based on the entire $^4F_{3/2}$ population, that is, they are gains divided by the total

Table 5		
Host	$\sigma_{0.94} (10^{-20} \text{ cm}^2)$	$\sigma_{1.06} (10^{-20} \text{ cm}^2)$
CAMGAR	1.4	5.4
YAG	3.0	20.0

population in R_1 and R_2 . For YAG, the results of Singh, Smith and Van Uitert² were corrected to be consistent with this averaging procedure.

2.6. Conclusion

Laser operation of Nd:CAMGAR at $0.94\text{ }\mu\text{m}$ seems much more practical than in Nd:YAG. The gain of the $1.06\text{ }\mu\text{m}$ line in CAMGAR is lower than the corresponding YAG line by a factor of 4.3. The ratio of the $1.06\text{ }\mu\text{m}$ gain to the $0.94\text{ }\mu\text{m}$ gain is also lower by a factor of 2.0.

¹E. J. Sharp, J. E. Miller, and D. J. Horowitz, J. Appl. Phys. 45, 4974 (1974).

²S. Singh, R. G. Smith, and L. G. Van Uitert, Phys. Rev. 10, 2566 (1974).

3. LiHoF₄ - a 980 nm Laser candidate

3.1. Introduction

Ho³ doped LiYF₄ has successfully been lased at several wavelengths ranging from the 750 nm $^5S_2 \rightarrow ^5I_7$ transition to the 3900 nm $^5I_5 \rightarrow ^5I_6$ transition. Laser action involving the $^5F_5 \rightarrow ^5I_7$ transition at 979 nm has also been reported both in 2% Ho in YLF and in LiHoF₄.^{1,2} In this work an evaluation of this laser transition has been performed. Spectroscopic measurements to determine relevant parameters such as the stimulated emission cross section, the fluorescent lifetimes and the excitation mechanisms indicate that LiHoF₄ is a potential efficient 980 nm laser candidate when operated at low temperature, ~100 K. Room temperature operation should under certain conditions also be possible.

3.2. Description of the system.

Figure 1 shows the energy multiplets of Ho³⁺. The laser transition of interest is from the 5F_5 multiplet to the 5I_7 multiplet. This constitutes a four level laser where the pump bands are the (5S_2 , 5F_4) multiplets and all the higher lying multiplets. With low concentration Ho in YLF, the 5S_2 levels fluoresce with high quantum efficiency and only 40% of the relaxation rate is due to multiphonon relaxation to the 5F_5 multiplet. Thus the pumping efficiency of the upper laser level (5F_5) is low. With increasing Ho concentration the 5S_2 fluorescence is rapidly quenched and in

LiHoF₄ no emission from 5S_2 is observed. The 5F_5 emission is not seriously quenched however, even when the levels above (5F_2 , 5F_4) are pumped. This means that with high Ho concentration the excitation mechanism at the 5F_5 multiplet involves energy transfer between neighboring Ho-ions. The most likely transfer process is the resonant 5F_3 , $^5I_8 \rightarrow ^5F_5$, 5I_7 as indicated in Fig. 1. The pumping efficiency at the 5F_5 levels should therefore be much higher in LiHoF₄ than for low concentration Ho in YLF.

Laser threshold and efficiency depends on, in addition to pumping efficiency, the stimulated emission cross section and the terminal level population. For each excitation in the 5F_5 multiplet there also is one in the 5I_7 multiplet due to the transfer process. There is therefore no net population difference between the 5F_5 and the 5I_7 multiplets. The thermal distribution within the multiplets, given by Boltzmann statistics, still makes it possible to achieve inversion between the lower level of 5F_5 and the upper level of 5I_7 . The occupation factor for the 5F_5 and 5I_7 levels at 300 K and 77 K are indicated in Fig. 1.

Referring to Fig. 1 we can now evaluate the performance of the $^5F_5 \rightarrow ^5I_7$ 980 nm LiHoF₄ laser. The pump bands are assumed to be the multiplets 5F_3 and above. There will also be some direct pumping of the 5F_5 multiplet. 5F_3 relaxes by energy transfer to 5F_5 by energy transfer simultaneously exciting an equal number of ions to 5I_7 . This transfer process is very fast with a rate greater than 10^7 sec^{-1} . The 5F_5

fluorescent lifetime in LiHoF_4 was measured to be 16 μsec at 300K and 33 μsec at 77 K. The energy storage time is therefore relatively short as compared to, for example, Nd:YAG.

For a total of N excitations, the inversion, ΔN , can be expressed as:

$$\Delta N = (f_u - f_l) N \quad 1$$

where f_u and f_l are the occupation factors for the upper and lower laser levels. Thus as long as $f_u > f_l$ there will be a net gain given by:

$$g = \sigma(f_u - f_l) N \quad 2$$

and the effect of the transfer is to yield an effective lower stimulated emission cross section σ'

$$\sigma' = (f_u - f_l) \sigma \quad 3$$

The fluorescent lifetime of the 5I_7 multiplet is long, 15 ms. High repetition rate operation will therefore be limited by population buildup in 5I_7 . However, only small amounts of quenching centers, either intentionally or unintentionally introduced can drastically reduce the 5I_7 lifetime. In reference 1 the lifetime of 5I_7 is given to be 270 μs in LiHoF_4 .

3.3. Spectroscopy

The spectroscopy of LiHoF_4 was performed with the intention of obtaining the stimulated emission cross section

for the 980 nm laser transition. In addition time resolved fluorescence measurements were performed to obtain the relaxation rates of the levels involved. The relevant lifetimes are indicated in Fig. 1.

There are several different methods available to determine the stimulated emission cross section. The peak stimulated emission cross section is related to the peak absorption cross section by the relation

$$\sigma_{em} = g_l/g_u \sigma_{ab}$$

where g_l and g_u are the degeneracies of the upper and lower levels. Thus if these are known and σ_{ab} can be measured σ_{em} can be found. In a four level laser transition σ_{ab} can normally not be measured. σ_{em} can then be found by comparing the emission intensity with a line with known cross section. Very often however there are several overlapping transitions in a fluorescent line. In this case the best result is obtained by deducing the gain directly from the fluorescence spectra. In this case the cross section obtained is one that when multiplied by the total multiplet population gives the proper gain. For the ${}^5F_5 \rightarrow {}^5I_7$ transition in LiHoF_4 we have the problem of overlapping transitions. In addition, and because of the overlapping lines, the exact positions of the energy levels are not known. The above gain vs wavelength can be obtained as described, however, the problem of population in the terminal

levels are then not included. At low temperature the thermal population in the upper 5I_7 levels is low enough to result in only a small error by omission. Figure 2 shows a relative plot of the room temperature cross section for the $^5F_5 \rightarrow ^5I_8$ and $^5F_5 \rightarrow ^5I_7$ transitions.

The actual value of the cross section has been omitted from the figure because of the unknown factors. These are, first, as mentioned above, the 5I_7 population, second the radiative quantum efficiency of the 5F_5 manifold and third, the emission to the 5I levels above 5I_7 has not been measured. The peak cross section for the 980 nm transition is estimated to be in the range of $(2 \text{ to } 10) \times 10^{-20} \text{ cm}^2$.

References

1. A. M. Morozov et al. Opt. Spectrosc., Vol. 39, No. 3, Sept. 75, p. 338.
2. I. G. Podkolzina et al., Opt. Spectrosc., Vol. 40, No. 1, Jan. 76, p. 111.
3. L. Esterowitz et. al., Appl. Phys. Letters., Vol. 35, 1 Aug. 79, p. 236.
4. N. Karayianis et al., J. Phys. Chem. Solids., Vol. 37 (1976), p. 675.

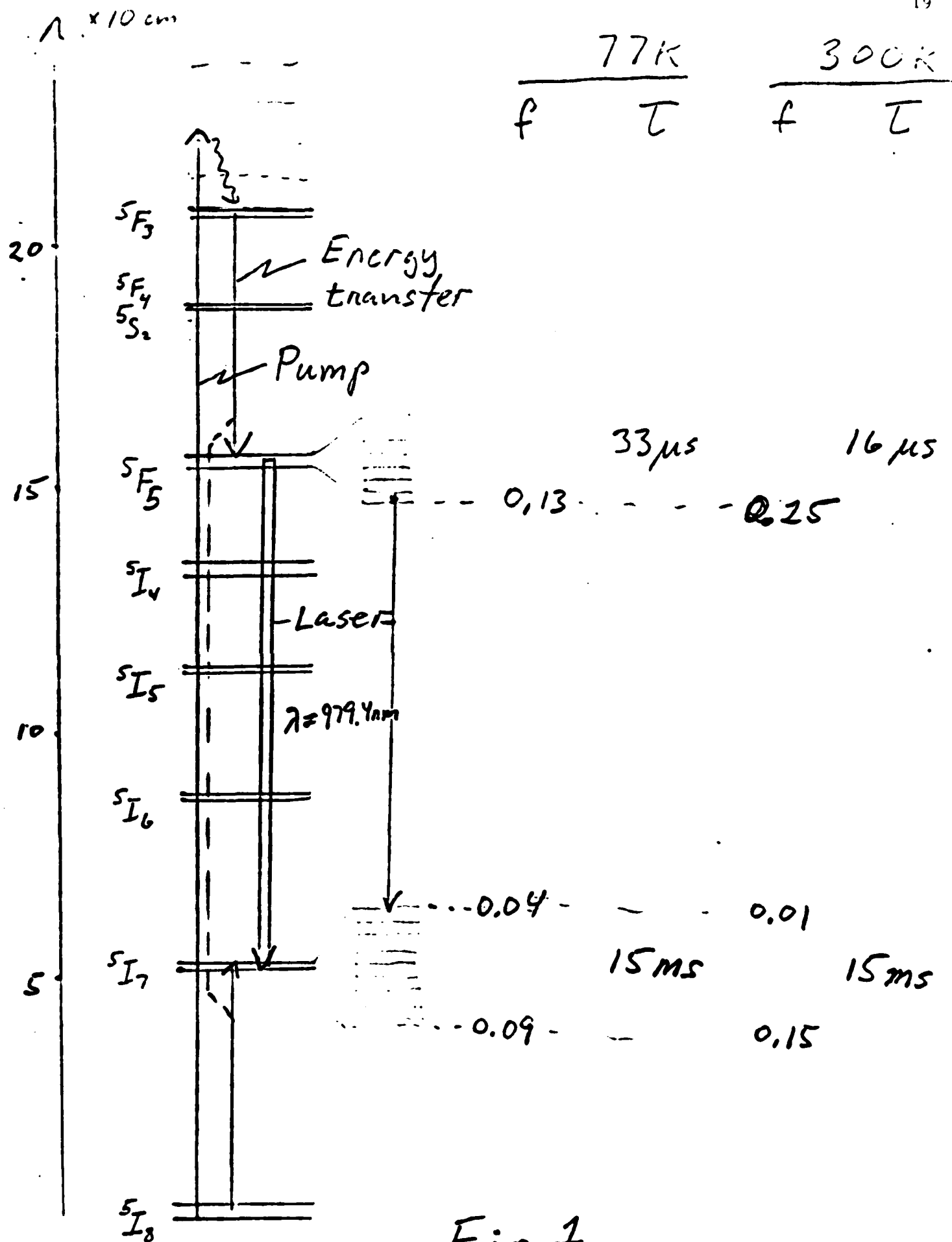
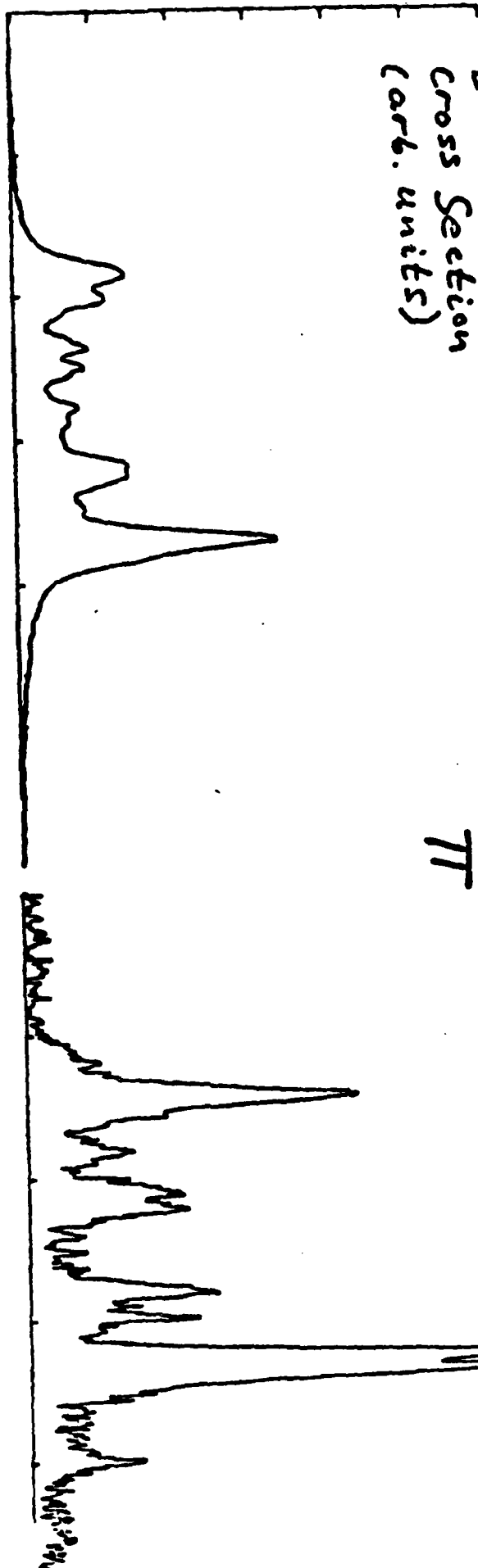


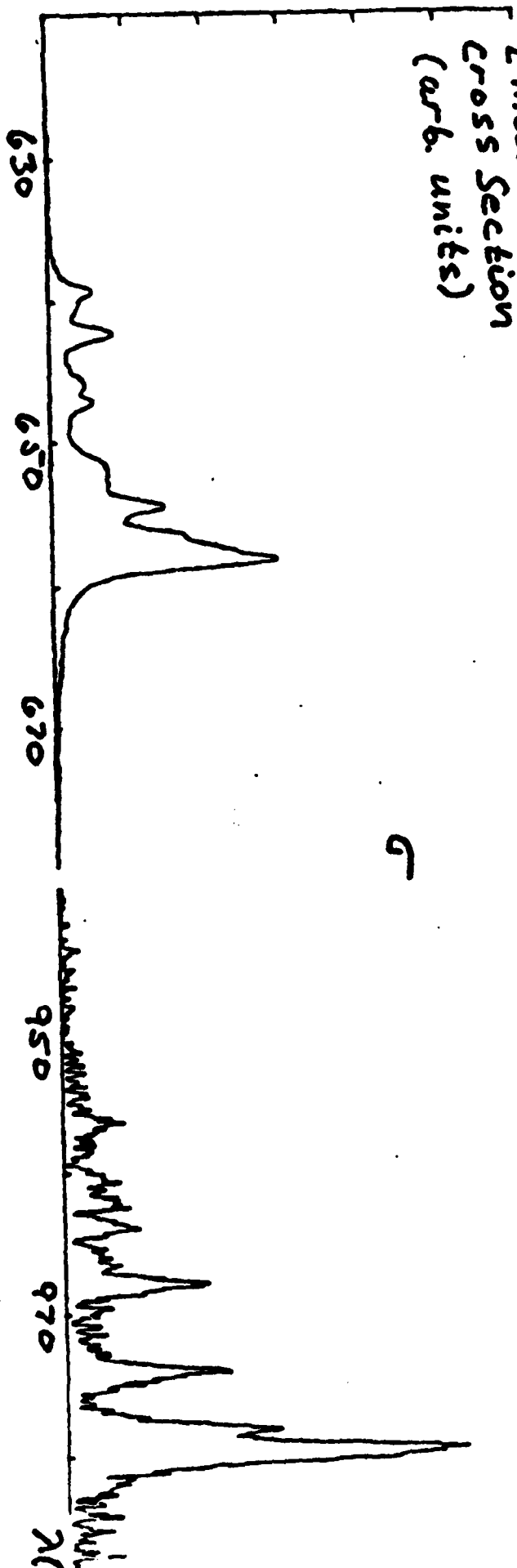
Fig. 1

Fig. 2

Emission
Cross Section
(arb. units)

 π 

Emission
Cross Section
(arb. units)

 σ 

Appendix I

THE TECHNIQUE OF LASER END PUMPING AS A METHOD OF
EVALUATION OF OPTICALLY PUMPED SOLID-STATE
LASER MATERIALS

by

FERNANDO SOBREVILLA CALVO

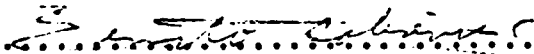
Licenciate in Physics, Universidad Nacional Autonoma de Mexico
(1974)

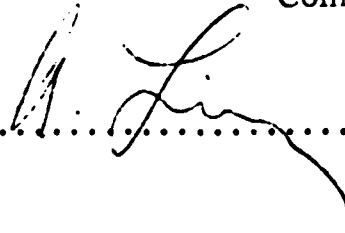
SUBMITTED IN PARTIAL FULFILLMENT OF THE
REQUIREMENTS FOR THE DEGREES OF
MASTER OF SCIENCE IN ELECTRICAL ENGINEERING AND
COMPUTER SCIENCE AND IN PHYSICS

at the

MASSACHUSETTS INSTITUTE OF TECHNOLOGY

February 1979

Signature of Author: 
Department of Electrical Engineering and
Computer Science and Department of
Physics, January 18, 1979

Certified by: 
Thesis Supervisor

Accepted by:
Chairman, Department Committee

THE TECHNIQUE OF LASER END PUMPING AS A METHOD
OF EVALUATION OF OPTICALLY PUMPED
SOLID-STATE LASER MATERIALS

by

Fernando Sobrevilla Calvo

Submitted to the Department of Electrical Engineering and
Computer Science and the Department of Physics on January 18, 1979,
in partial fulfillment of the requirements for the Degrees of Master of
Science in Electrical Engineering and Computer Science and in Physics.

ABSTRACT

The technique of laser end pumping as a method of evaluation of
optically pumped solid-state laser materials has been studied. Nd:YAG,
a well characterized material operated at the 1.06 μm wavelength, was
used as a standard to evaluate the technique.

It has been shown that the technique is better for lasing solid-state
materials in the cw mode and to measure the effective cross section of
the laser transition than techniques where a lamp is used as a pump.
The pump laser characteristics and laser rod length required for use
with this technique were obtained. It was found that the confocal cavity
is the best one for use with this technique.

Nd:CAMGAR was lased at 1.06 μm and 0.94 μm . The measured
effective cross sections for these transitions were $3.4 \pm 3 \times 10^{-20} \text{ cm}^2$
and $6 \pm 10 \times 10^{-20} \text{ cm}^2$, respectively. For Nd:YAG it was $2.1 \pm 2 \times$
 10^{-19} cm^2 .

Nd:CAMGAR has been proposed as a potential candidate for a high
power, frequency doubled, Q-switched laser at 0.47 μm . It has been
shown that it looks like a good candidate for this application.

Thesis Supervisor: Arthur Linz

Title: Senior Research Associate

ACKNOWLEDGEMENTS

The author is indebted to Dr. Arthur Linz, who supervised this work, and to Dr. Hans P. Jenssen for his continuous interest, helpful ideas and constant encouragement.

The author would also like to thank Dr. David Gabbe, who grew the Nd:CAMGAR crystal, all the members of the Crystal Physics group and fellow students for their friendship and assistance throughout this work.

He is grateful to Ms. Delphine Radcliffe for her competent typing of the manuscript and to Mr. John Mara for his skillful drawing of the illustrations.

TABLE OF CONTENTS

	Page
ABSTRACT	2
ACKNOWLEDGEMENTS	3
LIST OF FIGURES	6
LIST OF TABLES	7
 CHAPTER I INTRODUCTION	 8
1.1 Foreword	8
1.2 Energy Level Model of an Optically Pumped Solid-State Laser Material .	9
1.3 CW and Q-switched Laser Operation .	15
 CHAPTER II THE LASER END PUMPING TECHNIQUE .	 18
2.1 Description of the Laser End Pumping Technique	18
2.2 Theoretical Analysis of the Technique .	26
 CHAPTER III EXPERIMENTAL RESULTS	 42
3.1 Experimental Technique	42
3.2 Properties of Nd:YAG and Nd:CAMGAR .	52
3.3 Results	57
 CHAPTER IV DISCUSSION	 65
4.1 Thermal Effects in Laser Rods . . .	65
4.2 Measurement of the Effective Cross Section of the Laser Transition and Losses	75
4.3 Stability and Sensitivity of Laser Cavities	82

TABLE OF CONTENTS (continued)

	Page
4.4 Evaluation of Nd:CAMGAR as a potential high power, Q-switched laser at 0.94 μm	89
CHAPTER V SUMMARY AND CONCLUSIONS	94
REFERENCES	100

LIST OF FIGURES

Figure No.		Page
1.1	Simplified energy level diagram of a solid-state laser material.	10
2.1	Contour of a gaussian beam.	21
2.2	Longitudinally pumped laser.	23
2.3	Transversely pumped laser.	24
2.4	Enlarged view of the transverse excitation at the laser material.	25
2.5	Energy level diagram of Nd:YAG.	29
2.6	Resonator configurations giving uniphase wave fronts.	37
2.7	Diffraction loss per transit for the TEM ₀₀ mode of various symmetrical and stable cavities. .	40
3.1	Experimental set-up.	43
3.2	Fabry-Perot Resonator.	45
3.3	Experimental set-up for measuring the dependence of transmission on angle of incidence. . .	48
3.4	Transmission versus frequency for the input mirror for an incident beam at the 514.5 nm wavelength.	49
3.5	Experimental plot of the transmitted power versus the angle of incidence.	50
3.6	Power absorbed at threshold versus $-\ln R_1 R_2$ for a plane-parallel cavity.	61
3.7	Power absorbed at threshold versus $-\ln R_1 R_2$ for a hemispherical cavity.	62
3.8	Power absorbed at threshold versus $-\ln R_1 R_2$ for a confocal cavity.	63
4.1	Geometry of a cavity containing a thin positive lens.	74
4.2	Stability diagram for the passive laser cavity. .	86

LIST OF TABLES

Table Number		Page
I	Spectroscopic Parameters of Nd:YAG and Nd:CAMGAR	54
II	Nd:YAG and Nd:CAMGAR Rod Specifications.	55
III	Laser Cavity Specifications.	58
IV	Slope and Intercept of the Line Fit to the Experimental P_{ath} versus $-\ln R_1 R_2$ for Nd:YAG and Nd:CAMGAR lased at $1.06 \mu m$. .	64
V	Effective Cross Section of the $1.06 \mu m$ Transition of Nd:YAG and the $1.06 \mu m$ and $0.94 \mu m$ Transitions of Nd:CAMGAR. . . .	77
VI	Total Losses for the Plane-Parallel, Hemi- spherical and Confocal Cavities.	78
VII	Ratio of the Cross Section of Nd:YAG to Nd:CAMGAR at $1.06 \mu m$ for the Plane-Parallel, Hemispherical and Confocal Cavities. . . .	83

CHAPTER I

INTRODUCTION

1.1 Foreword

Optically pumped solid-state laser materials offer several advantages over other types of lasers. Laser action has been demonstrated in many materials covering the spectral wavelength range from $0.48\text{ }\mu\text{m}$ (Pr:YLF)⁽¹⁾ to $3\text{ }\mu\text{m}$ (Dy³⁺:BaY₂F₈).⁽²⁾ They are better suited for Q-switched operation than other types of lasers due to their relatively low gain and high density of active ions. For applications in which specific wavelength is not required, they offer advantages in size and ruggedness over other types of lasers. The most important practical optically pumped solid-state laser devices are the ruby laser at $0.69\text{ }\mu\text{m}$ and the Nd:YAG laser at $1.06\text{ }\mu\text{m}$.

Novel solid-state laser materials continue to be developed, so that it is important to have a system that will permit a simple and quick characterization of these materials. The laser end-pumping technique was studied as such a possible system. Nd:YAG at $1.06\text{ }\mu\text{m}$ was used as a standard to evaluate the technique, and Nd:CAMGAR at $0.94\text{ }\mu\text{m}$ and $1.06\text{ }\mu\text{m}$ as examples of its use. The importance of Nd:CAMGAR at $0.94\text{ }\mu\text{m}$ is that it has been proposed as a potential, high power, Q-switched, frequency doubled laser for underwater applications.

In this chapter a description will be given of the basic theory necessary to understand the operation of an optically pumped solid-state laser and will indicate the important laser parameters for its operation in different modes. A description of the laser end-pumping technique and its advantages over other methods of evaluation of solid-state laser

materials is given in the second chapter. In the third chapter the experimental results are presented. The discussion of the results obtained and an evaluation of Nd:CAMGAR in the mode of operation indicated before is given in the fourth chapter. The summary and conclusions are presented in the fifth chapter.

1.2 Energy Level Model of an Optically Pumped Solid-State Laser Material

The different modes of operation of an optically pumped laser material can be understood using a four energy level model, as shown in Fig. 1.1. The grosser features of operation in the different modes, such as average and peak powers, threshold conditions, etc., can be predicted with this model. On the other hand, this approach ignores longitudinal and radial variation of radiation inside the laser material, the spectral distribution of the laser emission, and the physical properties of the host material. Fortunately these factors can often be accounted for independently.

Optical amplification through stimulated emission of light of energy $h\nu = E_2 - E_1$ occurs when the population in the second level N_2 is bigger than in the first N_1 . That is, the population inversion defined as

$$\Delta N = N_2 - N_1 \quad (1.1)$$

is positive.

If the relaxation time from level (3) to level (2) occurs with a time constant τ_{32} , much shorter than the fluorescent lifetime of level (2) τ_2 , i. e., $\tau_{32} \ll \tau_2$, the population N_2 can be described by a simple rate equation involving only the pump rate and the fluorescent lifetime:

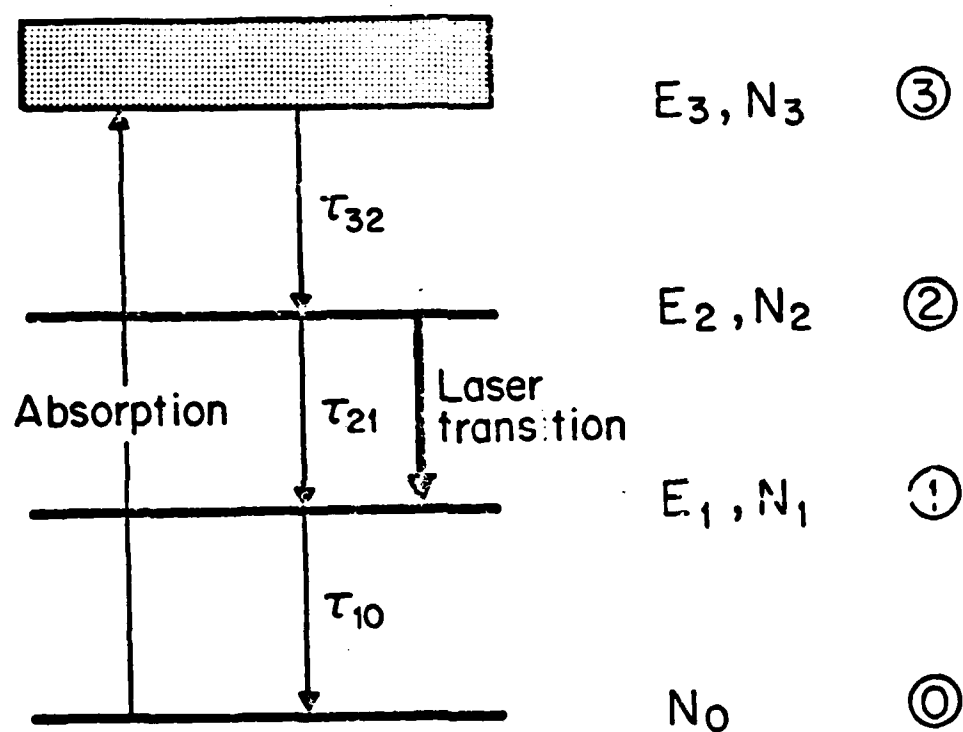


Fig. 1.1 Simplified energy level diagram of a solid-state laser material.

$$\frac{dN_2}{dt} = W_{03} - \frac{N_2}{\tau_2} \quad (1.2)$$

where W_{03} is the pump rate. In equilibrium

$$N_2 = W_{03} \tau_2 \quad (1.3)$$

If the material is excited by a pulse of duration T , short compared to τ_2 , from equation (1.2) we find that N_2 is given by

$$N_2 = W_{03} E e^{-t/\tau_2} \quad (1.4)$$

This equation allows the determination of τ_2 by measuring the radiated light as a function of time. Typically, the fluorescence lifetime is on the order of milliseconds. For example, for ruby it is 3.0 msec,⁽³⁾ for Nd:YAG it is 0.24 msec (0.73% Nd concentration), and for Nd:CAMGAR it is 0.31 msec (1.06% Nd concentration). The technique used to obtain these last two values is given in a later chapter.

The pump rate W_{03} is proportional to the pump source intensity and the effective absorption coefficient of the pump band. Only the latter is a function of the laser material and can be determined from the absorption coefficient of the material.

If the relaxation time from level (1) to the ground level occurs with a time constant, τ_{10} , much shorter than the relaxation from (2) to (1), τ_{21} , i. e., $\tau_{10} \ll \tau_{21}$, then N_1 is equal to the thermal population of this level, i. e.,

$$N_1 = \left[\beta_1 / \sum_i \beta_i \right] N_t = \beta N_t \quad (1.5)$$

where $\beta_i = \exp \left(\frac{E_i}{KT} \right)$ is the Boltzmann factor and N_t is the active ion concentration. The populations in these levels are related by the equation:

$$N_t = N_0 + N_1 + N_2 \quad (1.6)$$

where N_0 is the ground level population.

The ΔN required for laser threshold operation can be found from the relation:

$$R_1 R_2 \exp [2L(\sigma_{21} \Delta N - \delta)] = 1 \quad (1.7)$$

where L is the length of the laser medium confined between two mirrors of reflectivities R_1 and R_2 , σ_{21} is the peak stimulated cross section for the transition and δ the total distributed loss coefficient.

For many laser materials it is possible to simplify this model even further. One possibility is to have $E_1 \gg kT$, $\Delta N \approx N_2$, and $\tau_{10} \ll \tau_{21}$. This is the so-called four-level laser. For example, for Nd:YAG, $E_1 = 2.1 \times 10^3 \text{ cm}^{-1}$,⁽³⁾ which is much larger than kT at room temperature and $\Delta N \approx 2 \times 10^{16} \text{ ions/cm}^3$. The population inversion was obtained from equation (1.7) with $\sigma_{21} = 5 \times 10^{-19} \text{ cm}^2$,⁽⁴⁾ high reflectivity mirrors (99.9%) and $\delta \approx 10^{-2} \text{ cm}^{-1}$. For a typical 1% Nd concentration ($N_t \approx 10^{20} \text{ ions/cm}^3$) $N_1 \approx 2 \times 10^{15} \text{ ions/cm}^3$; therefore $\Delta N \approx N_2$.

The other extreme case is when the lower laser level is the ground state. In this approximation N_2 is at least $N_t/2$. It is called a three-level laser model. The ruby laser operated at $0.69 \mu\text{m}$ is an example of a three-level laser. From equation (1.7), with $\sigma_{21} = 2.5 \times 10^{-20} \text{ cm}^2$ ⁽³⁾ at room temperature, and the same value for the losses and mirror reflectivities as in the preceding example, we obtain $\Delta N = N_2 - N_0 \approx 10^{17} \text{ ions/cm}^3$. For a 0.04 weight % doping with Cr_2O_3 , the chromium concentration is $N_t \approx 10^{19} \text{ ions/cm}^3$. Since $N_t = N_2 + N_0$, then $N_2 \geq \frac{1}{2} N_t$.

The case when E_1 is equal to a few kT is between these two extreme cases. If either the losses are high or the mirror reflectivities

low, so that $\Delta N \approx N_2$, then we have a quasi-four-level laser. That is, the upper level population is used to overcome the losses. If the losses are low and the mirror reflectivities high so that $\Delta N \leq N_1$, then we have a quasi-three-level laser. In this case most of the upper level population is used to overcome the lower thermal population. Note that if the temperature is increased, the quasi-four-level laser becomes a quasi-three-level laser and vice versa. For example, Nd:CAMGAR operated at $0.94 \mu\text{m}$ has $E_1 = 814 \text{ cm}^{-1}$. If it is lased at room temperature, it is a quasi-three-level laser. From equation (1.7) we obtain $\Delta N \approx 10^{17}$ ions/ cm^3 , with $\sigma = 3.2 \times 10^{-20} \text{ cm}^2$, (5) and the same value for the other parameters as in the preceding examples. For a 1% Nd concentration ($N_t \approx 10^{20}$ ions/ cm^3), $N_1 \approx 10^{18}$ ions/ cm^3 . But if it is operated at liquid nitrogen temperatures (77°K), it becomes a quasi-four-level laser, since $N_1 \approx 2 \times 10^{13}$ ions/ cm^3 .

We can see from equation (1.7) that the ΔN required for threshold is inversely proportional to the material parameter σ , with everything else assumed independent of the laser material. For the model we are considering the stimulated emission cross section at the center of the atomic transition is given by:

$$\sigma_{21} = a \left(\frac{\lambda_0^2}{4\pi^2 n^2} \right) \frac{1}{(\tau_{21})_r \Delta\nu} \quad (1.8)$$

where a is a constant that depends on the transition lineshape, n the refractive index of the material, λ_0 is the vacuum wavelength at the transition peak, $\Delta\nu$ the linewidth, and $1/(\tau_{21})_r$ is the radiative transition probability per unit time from level (2) to level (1).

Since $(\tau_{21})_r$ cannot be measured directly, the following spectroscopic methods are used to measure σ . (4, 6)

1. Direct measurement of the cross section in absorption; this method is only possible if N_1 is appreciable.
2. Using equation (1.8) with the calculated value of $(\tau_{21})_r$. This value is obtained from the measurement of the branching ratio, fluorescence decay time and fluorescence quantum efficiency of the fluorescing state.
3. Comparing the emission intensity associated with the given transition with that of another emission line for which the cross section is already known from another method.

Summarizing, according to this model the important laser parameters are: the stimulated emission cross section, pump band absorption, fluorescence lifetime, losses and lower level laser population.

With the exception of the losses δ , all the laser parameters mentioned before can be measured with spectroscopic methods. In particular, σ can be calculated with these methods but it requires the measurement of several quantities and therefore it is a lengthy process. Even if an evaluation of the material with these methods predicts that it will lase, this does not guarantee that it will indeed do so. There might be other effects, which were either neglected or unknown, that could turn out to be important.

Therefore it is important to develop a technique that would allow a simple and quick method of lasing a material and an estimate of its laser parameters, including the losses δ .

In the next section the requirements on the laser parameters for the different modes of operation will be given. Only two modes will be discussed, cw and Q-switched. The requirements for long pulse operation are the same as for the cw case, and for a laser amplifier the same

as for the Q-switched case. The laser end-pumping technique, as applied here, operates in the cw mode. Thus, with the information obtained in this mode, the material performance can be evaluated in other modes.

1.3 CW and Q-switched Laser Operation

For cw laser operation it is important to have a low threshold and high gain for high efficiency operation. From equation (1.7), we see that for low threshold a large σ_{21} and small δ and N_1 are needed. For example, for Nd:YAG operated in this mode at the 1.06 μm wavelength, typically $\delta = 0.003 \text{ cm}^{-1}$, $R_1 = 1$, $R_2 = 0.9$, and $l = 5 \text{ cm}$. From Eq. (1.7):

$$\Delta N = \frac{1}{2l\sigma_{21}} \ln\left(\frac{1}{R_1 R_2}\right) + \frac{\delta}{\sigma} = 2.7 \times 10^{16} \text{ cm}^{-3} \quad (1.9)$$

In Nd:YAG the upper laser level is the upper level of the $^4F_{3/2}$ manifold and has 40% of the total $^4F_{3/2}$ population at room temperature. The thermal N_1 population is typically $2 \times 10^{15} \text{ cm}^{-3}$. The N_2 population at threshold is then $N_2 = 7 \times 10^{16} \text{ cm}^{-2}$. From (1.3) we get the pump rate at threshold $W_{03} = 3 \times 10^{20} \text{ sec}^{-1} \text{ cm}^{-3}$.

If a lamp is used for pumping, the pump power absorbed by the rod is the integral over frequency of the product of three factors: the lamp power output per unit frequency, the absorption coefficient of the rod, and the efficiency with which the light output is coupled into the rod. This calculation is too involved, but experiments done with Nd:YAG pumped by a krypton arc lamp have shown that approximately 7.5% of the electrical input to the lamp is absorbed by the crystal and 40% of the absorbed pump power leaves the crystal as stimulated emission.⁽⁷⁾ With these values, the absorbed pump power at threshold is 140 W/cm^3 and the lamp input at threshold is 1.9 kW/cm^3 . Typically, cw-pumped Nd:YAG

is pumped by krypton arc lamps with a maximum rating of about 3 kW/cm^3 . Thus the threshold power is a substantial part of the total available power.

In the Q-switching technique, energy is stored in the amplifying medium by optical pumping while the cavity Q is lowered to prevent the onset of laser emission. Although the energy stored and gain in the material are high, the cavity losses are also high, lasing action is prohibited, and the population inversion reaches a level far above the threshold for normal lasing action. When a high cavity Q is restored, the stored energy is suddenly released in the form of a very short pulse of light.

Thus in Q-switching a low threshold is insignificant. The limiting factor is the maximum energy that can be obtained in one pulse. From the threshold equation (1.7), neglecting the losses, we obtain:

$$2\ell\sigma_{21}\Delta N = \ln\left(\frac{1}{R_1R_2}\right) \quad (1.10)$$

In terms of the stored energy $E_{st} = V\Delta N h\nu$ we obtain:

$$2\ell \frac{E_{st}}{V E_s} = \ln\left(\frac{1}{R_1R_2}\right) \quad (1.11)$$

where $E_s = \frac{h\nu}{\sigma_{21}}$ is the saturation flux and V is the volume of the laser material. The purpose of the Q-switch is to reduce R_1R_2 as far as possible before switching. A problem that might appear is the competition between two laser transitions that share the same upper laser population. Then the onset of lasing would be determined by the transition which has higher gain. For Nd:YAG the gain at $1.06 \mu\text{m}$ is higher than at $0.94 \mu\text{m}$; ⁽³⁾ thus a mechanism has to be provided to suppress the first transition if Q-switched operation at $0.94 \mu\text{m}$ is desired.

In practice $R_1 R_2$ cannot be made to be much less than 0.01. That means that the maximum stored energy is limited to:

$$\frac{l}{V} E_{st} (\max) = \frac{E_s}{2} \times 4.6 \quad (1.12)$$

For Nd:YAG at $1.06 \mu\text{m}$ we have $E_s = 0.38 \text{ J/cm}^2$; thus the maximum stored energy is $\frac{l}{V} E_{st} (\max) = 0.87 \text{ J/cm}^2$. Thus the total maximum stored energy is independent of the length of the material and is only a function of the cross section area of the rod.

Summarizing, we see that for Q-switched operation high gain is not desirable and therefore a high σ is not wanted. In addition, a long fluorescence lifetime is desired since the pumping efficiency is higher for a long pulse than for a short pulse of the same energy. Finally, we want the competing transition to have as low a gain as possible.

CHAPTER II

THE LASER END-PUMPING TECHNIQUE

2.1 Description of the Laser End-Pumping Technique

Optical pumping of the solid state laser materials has been done using two different sources of optical radiation: broadband and laser. Pumping of a laser rod with a broadband source is done by enclosing both elements in a cavity that concentrates the light from the source onto the rod. A detailed discussion of this scheme can be found in the book by W. Koechner.⁽³⁾ With a laser source the pumping is done by focusing the beam into the rod. It can strike the rod either longitudinally or transversely to its axis. The choice is determined by the absorption coefficient of the laser material.

For most practical laser devices broadband sources are used. For our purposes a laser source is more convenient. Its advantages are the following:

1. For a laser source the absorption rate, W_{03} , of the material is easier to relate to the pump power incident on the material. In the direction of propagation of the pump beam, assuming a homogeneous material, the absorption rate is related to the incident intensity I_0 by the equation:

$$W_{03}(z) = \frac{\eta}{h\nu} I_0 [\sigma_0 N_0(z) + \sigma_1 N_1(z)] e^{-\int_0^z [\sigma_0 N_0(\ell) + \sigma_1 N_1(\ell)] d\ell} \quad (2.1)$$

where z is the distance from the point of incidence, σ_0 and σ_1 the absorption cross sections from the ground and lower laser level to an excited level, respectively, at the pump frequency, $h\nu$ the energy of a photon of the pump, and η the quantum efficiency, which accounts for the fact that not all of the atoms raised to the pump bands subsequently decay to the

upper laser level. In the transverse direction, assuming a gaussian pump beam and an isotropic material, the absorption rate distribution is a gaussian. It is given by the equation:

$$W_{03}(r) = W_{03} \exp [-2r^2/\omega^2] \quad (2.2)$$

where r is the distance to the axis of the beam and ω is the parameter that characterizes the radius of the pump beam.

On the other hand, for a broadband source, the absorption rate distribution over the cross section of the active material is the result of the combination of several effects: the spectral output of the source, the absorption spectra of the material, the illumination properties of the pump cavity, the refractive focusing occurring in the rod itself, and the nonuniform absorption of the pump radiation. Thus, even under idealized assumptions, calculation of the absorption rate is very tedious.

2. Since most of the energy input into the lamp is dissipated as heat, a cooling system has to be built into the system. For laser pumping, only a heat sink for the rod has to be provided. For example, the rod can be cemented to a copper block.

3. Due to requirements on the lamp, the shortest rods that can be pumped are 7 cm in length. For laser pumping, very short rods can be used. For example, laser rods of 1 mm in length have been lased,⁽⁸⁾ the limitation in size being imposed by the absorption of pump power in the material.

4. For broadband pumping, the rod has to be shaped in the form of a cylinder with an optically finished surface to obtain efficient transmission of light. For laser pumping, the rod can be shaped as a parallelepiped, which is easier to cut than a cylindrical rod. Only if transverse pumping

is used has one of the faces to be optically polished (naturally, the end faces still need to be polished).

Before starting the discussion of laser pumping, the properties of a propagating laser beam will be summarized. The light emitted by most lasers contains several discrete optical frequencies, separated from each other by frequency differences which can be associated with different modes of the optical resonator. It is common practice to distinguish two types of resonator modes: "longitudinal" modes differ from one another only in their oscillation frequency; "transverse" modes differ from one another not only on their oscillation frequency, but also in their field distribution in a plane perpendicular to the direction of propagation. Corresponding to a given transverse mode are a number of longitudinal modes which have the same field distribution as the given transverse mode but which differ in frequency.

We will assume that the pump and solid-state lasers are operating in only one transverse mode, the fundamental mode. The output of this mode is called a gaussian beam. For this type of beam the intensity distribution in every cross section is a gaussian, that is,

$$I(r) = I_0 \exp [-2r^2/\omega^2] \quad (2.3)$$

where r is the distance from the axis of the beam and ω , a parameter we mentioned before, is the radial distance at which the power density is decreased to $1/e^2$ of its axial value. The parameter ω is called the beam radius or "spot size". For a propagating gaussian beam, the width of the intensity profile changes along the axis (see Fig. 2.1). The gaussian beam contracts to a minimum diameter $2\omega_0$ at the beam waist where the phase front is planar. The spot size at a distance z from the beam waist

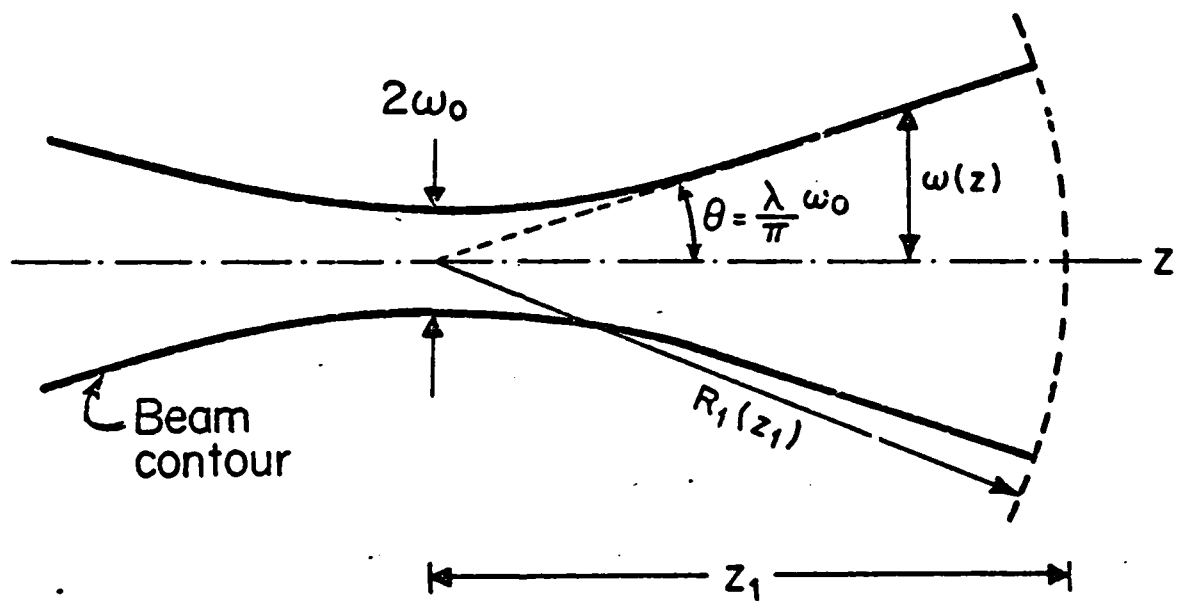


Fig. 2.1 Contour of a gaussian beam.

expands as a hyperbola. The asymptote of the hyperbola defines the half angle beam divergence, $\theta = \lambda/\pi\omega_0$, as shown in Fig. 2.1. It is important to point out that the smaller the spot size ω_0 at the beam waist, the greater the divergence. At sufficiently large distances from the beam waist, the wave has a spherical wavefront appearing to emanate from a point on the beam axis at the waist; the radius of curvature R is indicated in Fig. 2.1.

There are two schemes to pump a laser material with a laser source: longitudinal and transverse. The choice of scheme depends on the absorption coefficient of the material at the pump wavelength. The basic geometries for the two schemes are shown in Figs. 2.2 and 2.3.

For transverse excitation, the pump beam is focused by two crossed cylindrical lenses to form a narrow-line image on one side of the sample. An enlarged sketch of the resulting excitation at the sample is shown in Fig. 2.4; the laser beam radius is denoted by ω . From the figure it is clear that for efficient pumping an appreciable amount of the pump power has to be absorbed in a distance 2ω . Typically ω is on the order of tens of microns; therefore a large absorption coefficient is required. For example, neodymium pentaphosphate (NdPP) has been lased using this geometry.⁽⁸⁾ It was excited with a cw laser tuned at the absorption peak at $0.58 \mu\text{m}$; at this wavelength the absorption coefficient is $\alpha = 1.4 \times 10^2 \text{ cm}^{-1}$. For the concentric cavity with 5 cm, radius of curvature mirrors used by Chinn et al.,⁽³⁾ the beam radius was $\omega = 15 \mu\text{m}$. The power absorbed in the length 2ω is 44% of the incident power. On the other hand, for Nd:YAG with a 0.7% Nd concentration pumped with an argon ion laser at 514.5 nm , the absorption coefficient is $\alpha = 0.40 \text{ cm}^{-1}$. Thus, the power absorbed is 0.01% of the power incident. Obviously this configuration is not suitable for Nd:YAG.

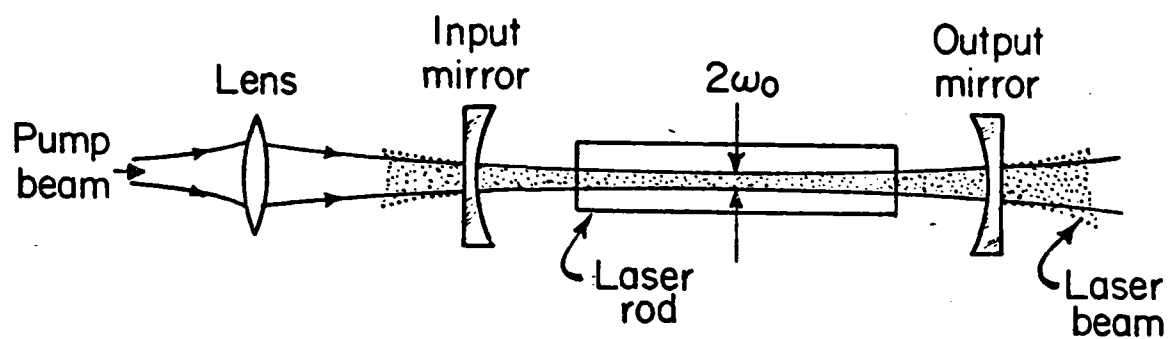


Fig. 2.2 Longitudinally pumped laser. The lens is used to match the pump and laser beams in the laser rod. ω_0 is the minimum beam radius of the beams.

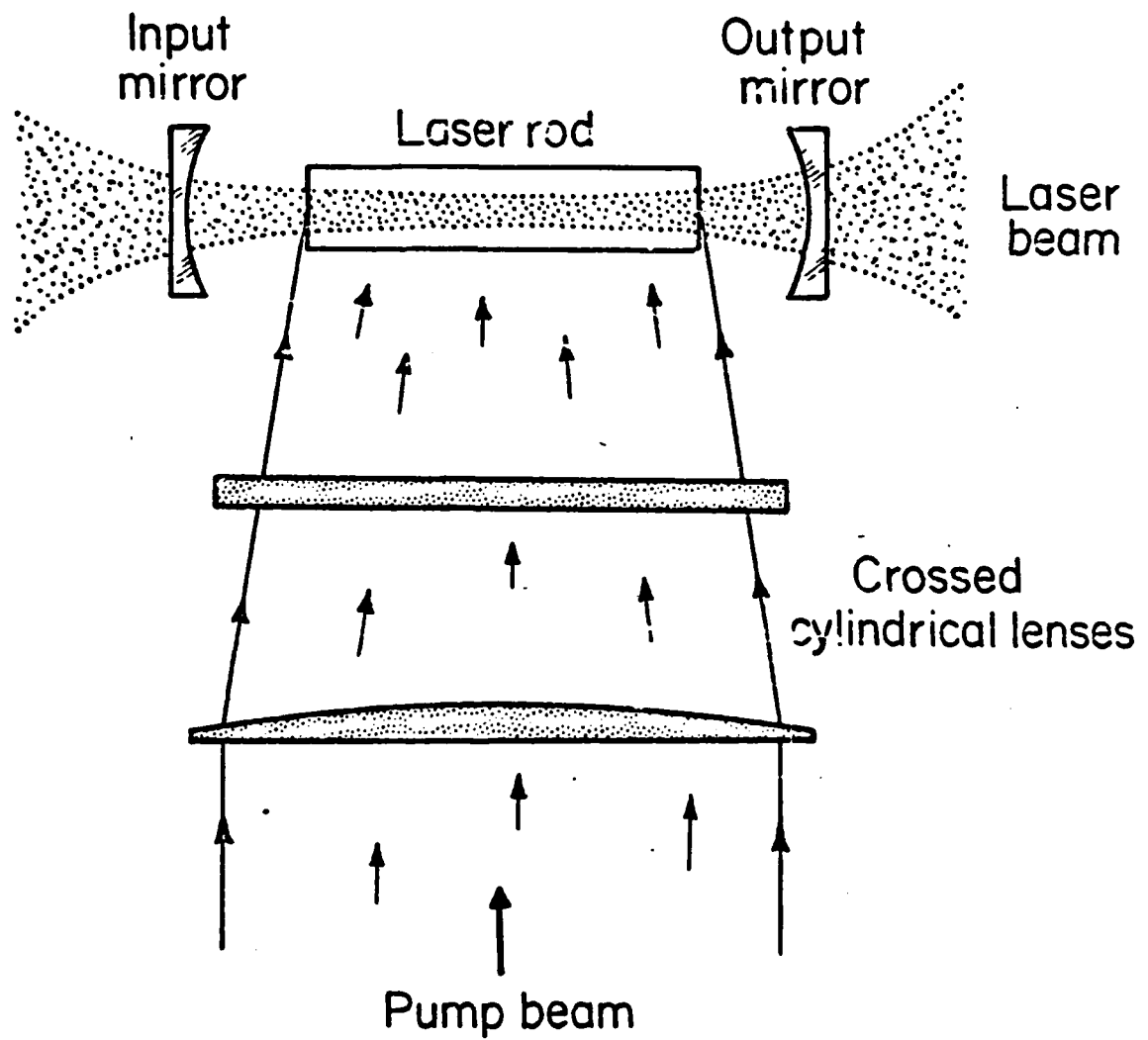


Fig. 2.3 Transversely pumped laser. The crossed cylindrical lenses are used to form a narrow-line image of the pump beam on one side of the sample.⁽⁸⁾

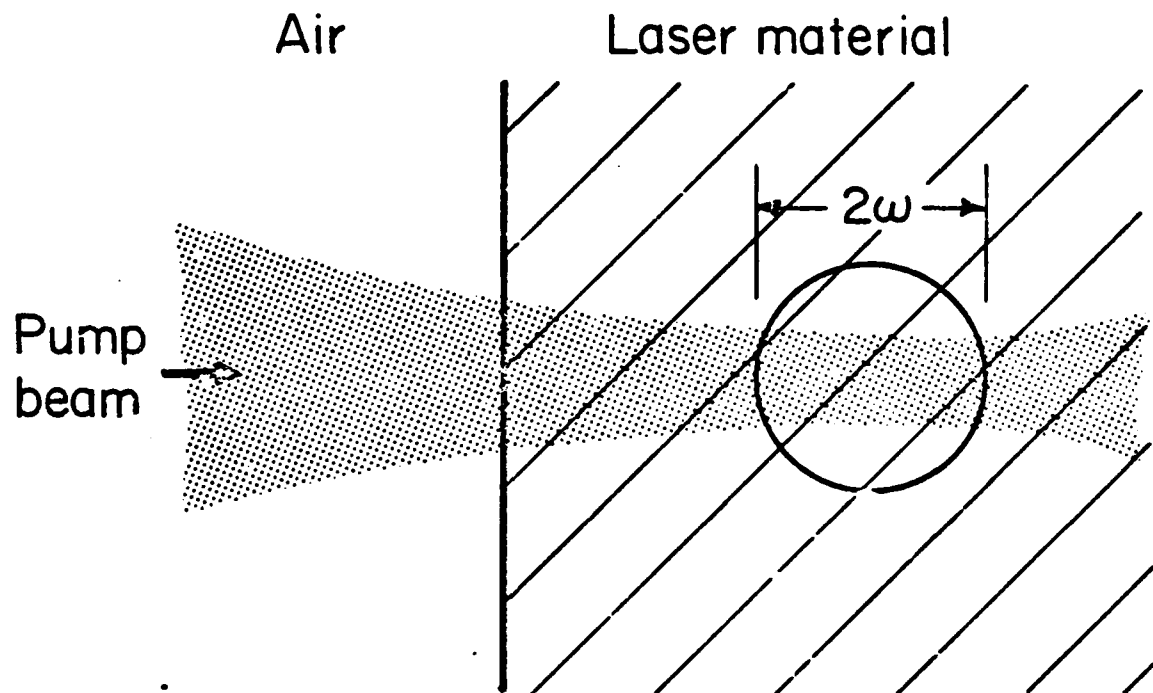


Fig. 2.4 Enlarged view of transverse excitation at the laser material.
 ω is the characteristic radius of the laser beam.⁽⁸⁾

If the absorption coefficient is small, longitudinal excitation is necessary to absorb an appreciable fraction of the pump power. For example, for Nd:YAG, using the same source as before, for a 2.17 cm length crystal, the absorbed power is 58% of the incident power. In this case, a close match of the two beams in the material is desirable for efficient pumping. Assuming that both are gaussian, this means that they should have the same radius. The laser beam radius is determined by the geometry of the resonator cavity, the pump beam radius by the beam divergence of the pump beam before it crosses the lens and by the optical elements it has to cross before reaching the crystal.

A theoretical analysis of this technique will be given in the next section.

2.2 Theoretical Analysis of the Technique

As mentioned in the preceding section, for efficient pumping it is necessary to have a close match between the pump and laser beams. From Fig. 2.2 it is clear that matching depends on the alignment of the beams and the equality of their radiuses. Alignment is the most important of these two factors. It depends on the choice of laser resonator and the mechanical characteristics of the experimental set-up. The equality of radiuses is achieved by a proper choice of the lens that focuses the pump beam into the laser rod.

This section will be divided into three parts. In the first one we will study the cw operation of the laser, assuming perfect matching of pump and laser beams, in the second, the procedure to match the beam radiuses, and in the third part, the fundamental mode characteristics of laser resonators.

Laser Operation Assuming Perfect Matching

In this case the gain region of the laser beam will coincide with

the pumped volume; therefore all the power absorbed will be used to pump the laser beam. The pump power absorbed per unit volume is a function of the distance along the rod axis; therefore the population inversion will also be a function of this distance. The laser threshold equation (1.7) becomes:

$$2\sigma \int_0^L \Delta N(x) dx = 2L\delta - \ln R_1 R_2 \quad (2.4)$$

where σ is assumed to be constant, L is the length of the rod, and 2 that of the cavity. In the next paragraphs we will derive an expression for this equation in terms of the absorbed intensity.

The upper laser level population is obtained from equations (2.1) and (1.3)

$$N_2(z) = [\sigma_0 N_0(z) + \sigma_1 N_1(z)] \left[\frac{\eta \tau_2 I_0}{h\nu} \right] \exp \left[- \int_0^z [\sigma_0 N_0(\ell) + \sigma_1 N_1(\ell)] d\ell \right] \quad (2.5)$$

Substituting equations (1.5) and (1.6) in (2.4), we obtain:

$$N_2(z) = \alpha \left[\frac{\eta \tau_2 I_0}{h\nu} \right] \left[1 - \frac{N_2}{N_t} \right] \exp \left[- \alpha \left(z - \int_0^z \frac{N_2(\ell)}{N_t} d\ell \right) \right] \quad (2.6)$$

$$\alpha = \left[\frac{\sigma_0 + \sigma_1 \beta}{1 + \beta} \right] N_t$$

where α is the absorption coefficient for small incident intensities, i.e., $N_2 \ll N_t$.

With the expressions for ΔN , N_1 , N_t and N_2 given by equations (1.1), (1.5), (1.6) and (2.6), respectively, it is possible to obtain an expression for ΔN as a function of z . This calculation will not be done since we can express the equations in a simpler form with approximations that are valid for many solid state laser materials. Besides, this solution will give more physical insight than a general solution.

Before starting with a discussion of the particular cases, we would like to point out that there is a further consideration that has to be made regarding the laser levels. In general, the laser levels are degenerated. For example, for Nd:YAG at $1.06 \mu\text{m}$ the upper laser manifold ${}^4F_{3/2}$ is split into two levels; the lower laser manifold ${}^4I_{11/2}$ is also split into several laser levels (see Fig. 2.5). The relaxation time between these levels is very short, on the order of a nanosecond or less. Therefore the populations of the levels in the manifold are in thermal equilibrium. There are several transitions between the degenerate levels of the upper and lower manifolds with different cross sections. It is customary to define the effective cross section for the transition in terms of the population of the upper degenerate level for which there is higher gain. The upper level, N_u , is related to N_2 by the equation

$$N_u = \frac{e^{\Delta E/kT}}{1 + e^{\Delta E/kT}} N_2 = f_B N_2 \quad (2.7)$$

where f_B is the Boltzmann factor and ΔE is the energy difference between the two levels.

Four-Level Laser

Using the approximations indicated in the introduction, L and $N_2 \ll N_t$, we obtain from equations (2.4), (2.6) and (2.7) the laser threshold equation:

$$2\sigma\tau_2 f_B \gamma (1 - e^{-\alpha L}) = 2L\delta_s + 2L\delta_d - \ln R_1 R_2 \quad (2.8)$$

where γ is a parameter that characterizes the laser pump. The losses have been expressed in terms of the scattering losses, δ_s , and the diffraction losses, δ_d .

From this equation we see that there is an optimum length for

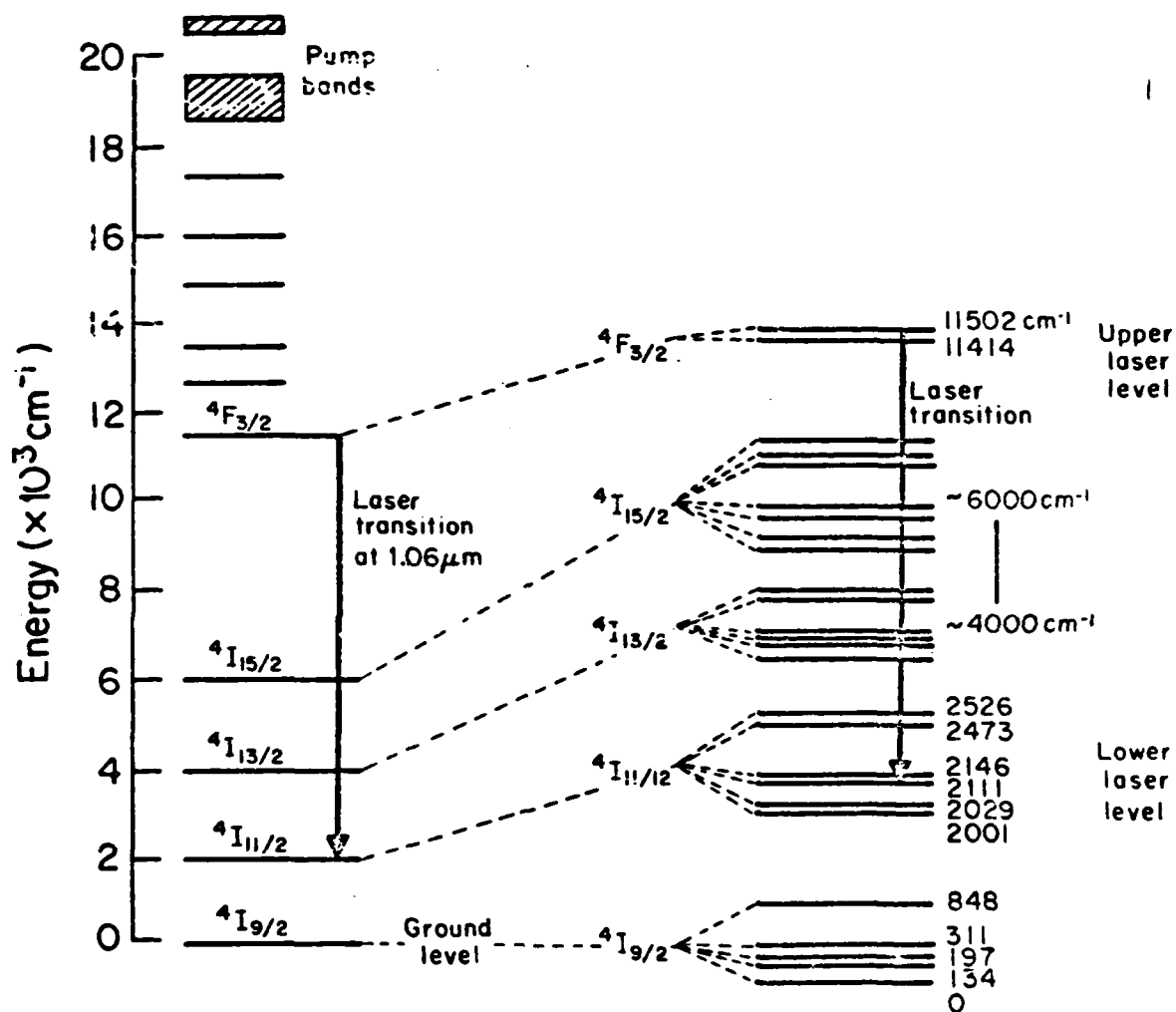


Fig. 2.5 Energy level diagram of Nd:YAG. The transition $^4F_{3/2} \rightarrow ^4I_{11/2}$ at 1.06 μm is indicated by the arrow. (3)

which γ is a minimum. If l is large, all the incident intensity will be absorbed, but the scattering losses will also be large. Therefore a large value for the incident intensity is required. On the other hand, if l is small the scattering losses are small but the absorbed intensity is also small. Therefore, once more, a large incident intensity is necessary.

To obtain the optimal length, l_{op} , we express γ as a function of l using equation (2.8)

$$\gamma(l) = \left(\frac{1}{2\sigma_2 f_B} \right) (2l\delta_s + 2L\delta_d - \ln R_1 R_2)$$

The minimum $\gamma(l)$ is given by $l = l_{op}$, which satisfies the equation:

$$e^{\alpha l_{op}} - \alpha l_{op} = 1 + \frac{\alpha}{2\delta_s} (2L\delta_d - \ln R_1 R_2) \quad (2.9)$$

As an example of a four level laser we take Nd:YAG with a 0.73% Nd concentration. It has a strong absorption band in the 0.56 - 0.60 μm region with a strong peak at 0.589 μm with $\alpha = 7.4 \text{ cm}^{-1}$. Therefore, it is reasonable to think that a cw dye laser tuned to this absorption peak is a suitable pump. At this wavelength the quantum efficiency is unity⁽⁹⁾ and the maximum power input on the laser rod is 0.3 watts (losses due to reflections from the optical elements have been taken into account). Assume that high reflectivity mirrors are used for the laser cavity, i.e., $R_1 = R_2 = 99.9\%$, no diffraction losses and scattering losses of $\delta_s = 0.007 \text{ cm}^{-1}$. Substituting these values in equation (2.9) we obtain $l_{op} = 0.16 \text{ cm}$. And $(I_0/h\nu) (1 - e^{-\alpha l_{op}}) = 6.1 \times 10^{17} \frac{1}{\text{sec}} \frac{1}{A}$, where A is the cross section area of the pump beam.

Another possible pump source is an argon ion laser which, although the absorption coefficient at the pump wavelength is smaller, has

a higher power output than a cw dye laser. In particular for the $0.5145 \mu\text{m}$ wavelength, $\alpha = 0.40 \text{ cm}^{-1}$, and the maximum power output on the laser rod is 4 watts. Using the same values for the laser cavity as before, we find that $l_{\text{op}} = 0.83 \text{ cm}$ and $(\eta I_0 / h\nu)(1 - e^{-\alpha l_{\text{op}}}) = 2.9 \times 10^{18} \frac{1}{\text{sec}} \frac{1}{\text{A}}$. Thus we see that the argon laser is better than the cw dye laser.

Another example of a four-level laser is Nd:CAMGAR operated at $1.06 \mu\text{m}$. For a sample with 0.76% Nd concentration operated at $1.06 \mu\text{m}$, $N_t = 10^{20} \text{ ions/cm}^3$, $E_1 = 2 \times 10^3 \text{ cm}^{-1}$, $\beta = 7.3 \times 10^{-5}$, $N_1 = 7.3 \times 10^{15} \text{ ions/cm}^3$, and $\sigma = 8.5 \times 10^{-20} \text{ cm}^2$.⁽⁵⁾ Thus for $\delta \approx 10^{-2} \text{ cm}^{-1}$, and high mirror reflectivities, $N = 10^{14} \text{ ions/cm}^3$. Thus we have a four-level laser once more. The peak in the absorption coefficient in the $0.56 - 0.60 \mu\text{m}$ region occurs at $0.584 \mu\text{m}$ with $\alpha = 4.5 \text{ cm}^{-1}$. The absorption coefficient for the $0.515 \mu\text{m}$ wavelength is $\alpha = 0.42 \text{ cm}^{-1}$. Repeating the same calculations as for the Nd:YAG case we find that for the cw dye laser $l_{\text{op}} = 0.21 \text{ cm}$ and $(I_0 / h\nu)(1 - e^{-\alpha l_{\text{op}}}) = 3.0 \times 10^{18} \frac{1}{\text{sec}} \frac{1}{\text{A}}$. Thus the argon ion laser is a better pump.

Quasi-Three-Level Laser

With the approximation indicated in the introduction, L and $N_1, N_2 < N_t$, we find that N_1 is independent of z and given by:

$$N_1 = \beta N_t \quad (2.10)$$

and the laser threshold equation by:

$$2\sigma\tau_2 f_p \gamma (1 - e^{-\alpha l_{\text{op}}}) = 2L[\delta_s + \sigma N_1] + 2L\delta_d - \ln R_1 R_2 \quad (2.11)$$

This is the same as equation (2.8) for a four-level laser, but an extra term has been added to the scattering losses. This loss is due to reabsorption from the thermally populated lower laser level.

As an example, consider AMGAR with a 1.05% Nd concentration. At the 0.94 μm transition in the introduction, $N_1 = 2 \times 10^{17}$ ions/cm³, so $\sigma N_1 = 0.064 \text{ cm}^{-1}$. The scattering losses are negligible and the resonator does not have high reflectivities, the $\ell_{\text{op}} = 0.08 \text{ cm}$ for a cw dye laser. For the $(1 - e^{-\alpha \ell_{\text{op}}}) = 1.1 \times 10^{-18} \frac{1}{\text{sec}} \frac{1}{\text{A}}$.

Three-Level Laser

Using the approximation

$$N_1 = N_t + \frac{1}{2} N_t \quad (2.12)$$

If we also require $\Delta N \ll N_t$,

$$\sigma N_t (1 - e^{-\frac{\alpha}{2} \ell})$$

Note that the absorption coefficient is half of its value for low intensities. This result is expected since only half of the active ions in the ground level are excited. Besides the scattering losses there is a loss due to

As shown before, rubidium ions with an argon ion laser. Birnbaum et al. (10) have put a value of 1.3×10^{19} ions/cm³ for a sample of Cr^{3+} in an absorption coefficient at the 0.69 μm transition. The cross section at the 0.69 μm transition is $2.5 \times 10^{-20} \text{ cm}^2$. (3) The absorption due to the ground level is negligible. For high reflectivities, we find that $\ell_{\text{op}} = 0.12 \text{ cm}$.

AMGAR with a 1.05% Nd concentration. $\sigma = 3.2 \times 10^{-20} \text{ cm}^2$. (5) As shown in the introduction we find that $\sigma N_1 = 0.064 \text{ cm}^{-1}$. The scattering losses are negligible and the resonator does not have high reflectivities, the $\ell_{\text{op}} = 0.08 \text{ cm}$ for a cw dye laser. For the $(1 - e^{-\alpha \ell_{\text{op}}}) = 1.1 \times 10^{-18} \frac{1}{\text{sec}} \frac{1}{\text{A}}$. The argon laser pump is better.

in the introduction we find that

laser threshold equation is given by:

$$\frac{\sigma N_t}{2} + 2L\delta_d = \ln R_1 R_2 \quad (2.13)$$

half of its value for low intensities. Only half of the active ions in the ground level are excited. Besides the scattering losses there is a loss due to the emission of radiation by the ground level. Cr^{3+} is a three-level laser.

material with an argon ion laser. The ion concentration was 1.3×10^{19} ions/cm³ with a μm wavelength of 0.63 μm . The cross section at the 0.63 μm transition is $2.5 \times 10^{-20} \text{ cm}^2$. (3) The emission dominates over the scattering losses, and assuming no diffraction

Finally, note that the stimulated emission cross section and losses can be measured using the laser threshold equation. If the power absorbed at threshold, P_{ath} , is measured for different mirror reflectivities we obtain a straight line whose equation is:

$$P_{ath} = \left[\frac{h\nu A}{2\sigma\tau_2 f_B \eta} \right] (-\ln R_1 R_2) + \left[\frac{h\nu A}{\sigma\tau_2 f_B \eta} \right] \Delta \quad (2.14)$$

where Δ is the total loss per transit in the material. The value of σ can be determined from the slope if all the other quantities are known. The total losses can be obtained by extrapolation of the line to $\ln R_1 R_2 = 0$.

Matching of Pump and Laser Beams

The shape and beam waist of the laser beam are determined by the choice of laser cavity. By a suitable choice of optics the pump beam can be matched to the laser beam, that is, the two beam waists coincide. The beam radius $\omega(z)$ depends not only on the beam waist but also on the wavelength. Therefore even if the beams coincide at the beam waist, it will not be true for other points along the axis of the rod. The equation that relates this quantity is:

$$\omega(z) = \omega_0 \left[1 + \left(\frac{\lambda z}{\pi \omega_0^2 n} \right)^2 \right]^{\frac{1}{2}} \quad (2.15)$$

where n is the index of refraction of the material.

The mismatch produced by this effect is negligible for the wavelengths and cavities used in this thesis. For example, Nd:YAG was lased at $1.06 \mu\text{m}$ using an argon ion laser at $0.515 \mu\text{m}$ as a pump. The beam waist at the center of a 2 cm rod was on the order of $100 \mu\text{m}$. The index of refraction of Nd:YAG is 1.8. From equation (2.15) we find that the beam waist at the end face of the rod is 4% bigger at $1.06 \mu\text{m}$ than at $0.515 \mu\text{m}$.

The output of the pump laser can be transformed by a suitable choice of optical elements into a beam that matches the laser beam position and size in the rod. A discussion of the transformation of gaussian beams can be found in Yariv's book.⁽¹¹⁾ The pump beam is focused into the laser cavity with a lens whose position and focal length are chosen to match the laser beam waist and position. The specifications required for the lens can be found in the following way.

The pump beam waist ω_0 , after being focused, is given by

$$\omega_0 = f_e \theta \quad (2.16)$$

where θ is the half angle beam divergence and f_e is the equivalent focal length of the optical system formed by the focusing lens, input mirror and laser rod. This equation is valid in the far field approximation $(\frac{\lambda z}{n} / \pi \omega_0^2) \gg 1$. Let l_3 be the distance from the beam waist to the end face of the rod, l_2 from the end face to the input mirror and l_1 from this mirror to the lens (see Fig. 3.1). For a given l_3 and ω_0 the focal length f_1 of the lens and l_1 are given by:

$$\frac{1}{f_1} = \frac{\theta}{\omega_0} \left[n - \frac{1}{f_2} (l_2 + l_3) \right] \quad (2.17)$$

$$l_1 = f_1 \left[1 - \frac{\theta}{\omega_0} (l_2 + \frac{l_3}{n}) \right]$$

Description of the Fundamental Mode Characteristics for Laser Resonators

We showed before that for laser operation a large value of the parameter $\gamma = \frac{\eta I_0}{h\nu}$ is preferable. But $I_0 = P_0/A$, where P_0 is the power incident and A the area of the pump beam in the laser material. Therefore, for laser operation we would prefer a small value of A . This value

is determined by the type of laser resonator.

A small area is not all that is required from a laser cavity. Alignment of the two beams is also a very important factor. For example, Nd:YAG was lased at $1.06 \mu\text{m}$ with a laser beam radius on the order of $100 \mu\text{m}$. If the pump beam forms an angle of approximately 0.8° with the laser beam, then 70% of the laser beam volume is unpumped. Therefore we also require appropriate sensitivity characteristics of the resonator to be able to obtain good alignment.

Another factor that has to be taken into account is diffraction losses. If the resonator has a very small beam waist, then the beam divergence will be large and would result in large diffraction losses.

Thus we see the necessity of studying the characteristics of the different resonators. In the discussion that follows we will assume that the laser rod is acting as a passive element in the cavity. Furthermore, since it was possible to lase the materials in the fundamental mode using the laser end-pumping technique, the discussion will only be limited to this mode. An excellent discussion on the subject of laser resonators can be found in the book of W. Koechner.⁽³⁾

The most commonly used laser resonators are composed of two spherical or flat mirrors facing each other. We will consider the generation of the fundamental mode by such a resonant structure.

The gaussian beam shown in Fig. 2.1 has a wavefront curvature of R_1 at a distance z_1 from the beam waist. If we put a mirror at z_1 whose radius of curvature equals that of the wavefront, then the mode shape has not been altered. To proceed further, we can go along the z axis to another point z_2 , where the fundamental mode has a radius of curvature R_2 , and place there a mirror whose radius of curvature R_2

equals that of the spherical wavefront at z_2 . Again the mode shape remains unaltered.

Therefore, to make a resonator, we simply insert two reflectors which match two of the spherical surfaces. Alternatively, given two mirrors separated by a distance, L , if the position of the plane $z = 0$ and the value of the parameter ω_0 can be adjusted so that the mirror curvatures coincide with the wavefront surfaces, we will have found the resonator modes. The most commonly used resonator geometries are indicated in Fig. 2.6. We will now give a brief discussion of the characteristics of the fundamental mode for different symmetrical cavities.

For mirrors of equal curvature, the beam waist occurs at the center of the resonator and its value is given by the equation:

$$\omega_0^2 = \frac{\lambda}{2\pi} [L(2R - L)]^{\frac{1}{2}} \quad (2.18)$$

where R is the mirror curvature and L the distance between mirrors.

A special case of symmetrical configuration is the spherical or concentric resonator which consists of two mirrors separated by twice their radiuses, that is, $R = L/2$. The corresponding beam consists of a mode whose dimensions are fairly large at each mirror and which focuses down to a diffraction limited spot at the center of the resonator.

It is clear that, in practice, the actual separation of the mirrors can never be quite as great as $2R$, since this would result in extremely large diffraction losses at the mirrors together with a "zero" mode dimension at the middle of the cavity, which is physically impossible. In practice one makes the mirror separation slightly less than $2R$ so that a value of ω_0 is obtained that gives reasonably small diffraction losses.

In a spherical cavity the mode is symmetric with respect to its

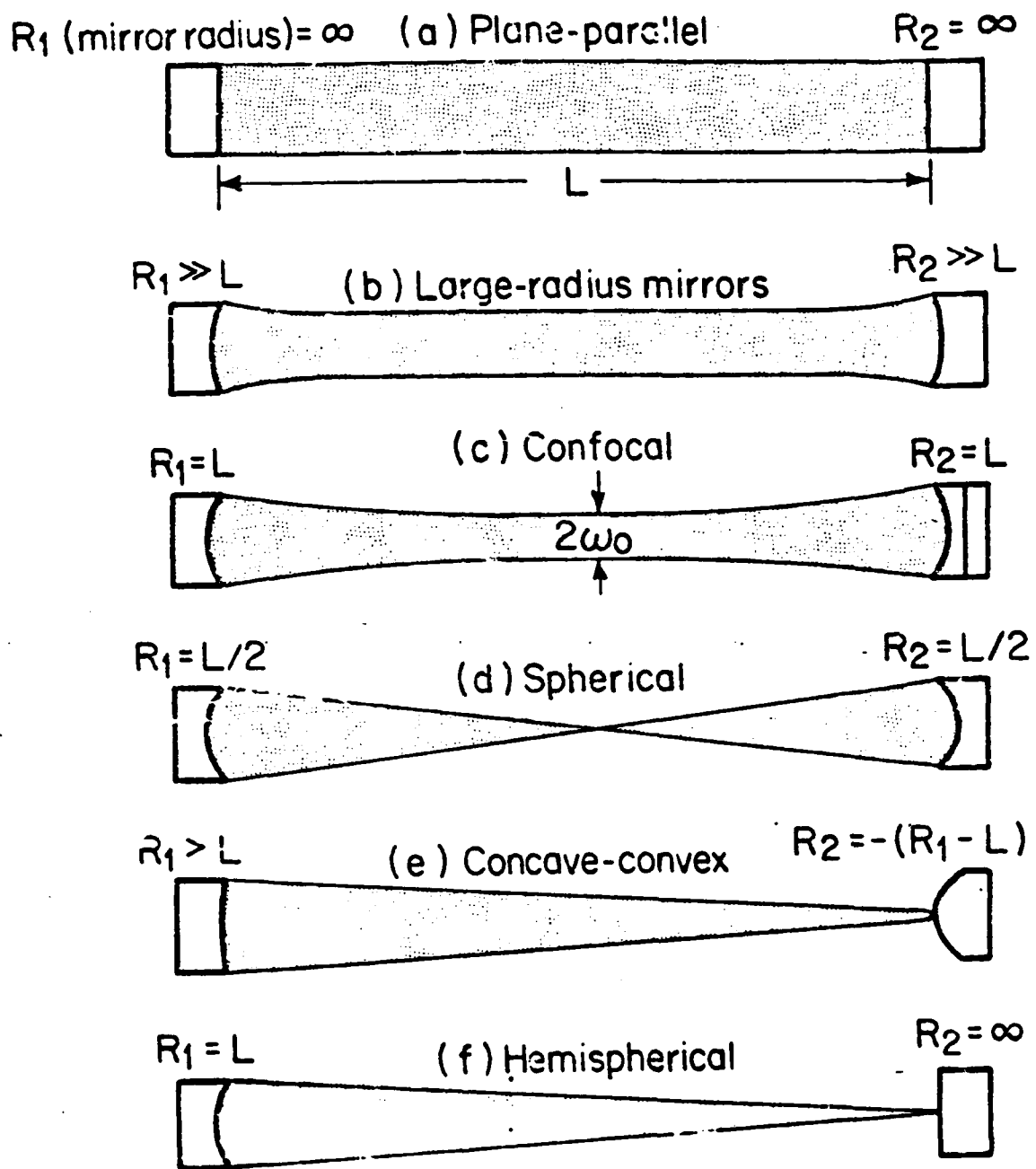


Fig. 2.6 Resonator configurations giving uniphase wavefronts (intracavity radiation pattern is shaded).⁽³⁾

center. Therefore, if a flat mirror is placed in the middle, the mode pattern will not be altered. But its stability and sensitivity will be different. This new type of cavity is called hemispherical.

Another important special case is the confocal resonator. The mirror separation equals the curvature of the mirrors, that is, $R = L$. From equation (2.18) we obtain

$$\omega_0 = (\lambda R / 2\pi)^{\frac{1}{2}} \quad (2.19)$$

The beam divergence is the smallest of any of the stable symmetric resonators.

Finally, we have the plane-parallel resonator for which the mirrors are plane and parallel. It can be considered as a special case of a large radius mirror configuration with $R_1 = R_2 = \infty$.

In any real laser resonator some part of the laser beam will be lost either by spillover at the mirrors or by limiting apertures, such as the lateral boundaries of the active material. These losses will depend on the diameter of the laser beam in the plane of the aperture and the aperture radius. If we take a finite aperture of radius a within the resonator into account, the diffraction losses depend on four parameters R_1 , R_2 , L and a , which describe the resonator, and on λ characterizing the particular optical beam present in the resonator. The losses depend only on certain combinations of these parameters. These parameters are the so-called Fresnel number:

$$N = a^2 / \lambda L \quad (2.20)$$

and the quantity g is defined by:

$$g = 1 - \frac{L}{R} \quad (2.21)$$

The parameter N can be thought of as the ratio of the acceptance angle (a/L) of one mirror as viewed from the center of the opposing mirror to the diffraction angle (λ/a) of the beam. Therefore, when N is small, especially if $N < 1$, the loss factor will be high because only a portion of the beam will be intercepted by the mirrors. When N is large, the losses will be low for the stable resonator configurations. In Fig. 2.7 we show the diffraction loss per transit for the fundamental mode for various symmetrical resonators.

Now we will study the stability of the different configurations. There are two contexts in which the term "stability" is used. First, laser resonators are said to be optically stable if low-loss modes can exist in the resonator. Second, the mode size and position are sensitive to mechanical and optical perturbations of the optical elements. We will refer to the stability of the mode against these perturbations as the resonator sensitivity.

When designing resonators for an optimum mode size, it will be of the utmost importance to consider the resonator sensitivity to these mechanical and optical perturbations. Usually one is interested in the sensitivity of the resonator to two common types of perturbations: first, a time-varying thermal lensing effect caused by the laser rod and, second, misalignments of the resonator mirrors. The former perturbation leads mainly to a change in mode size and beam divergence, whereas the latter perturbation leads to a lateral displacement and angular tilt of the output beam, which causes an increase of the diffraction losses and, more important, to misalignment of the pump and laser beams. First-order effects on the modes as a function of cavity perturbation are usually obtained by evaluation of the sensitivity matrix.⁽³⁾ The resonator

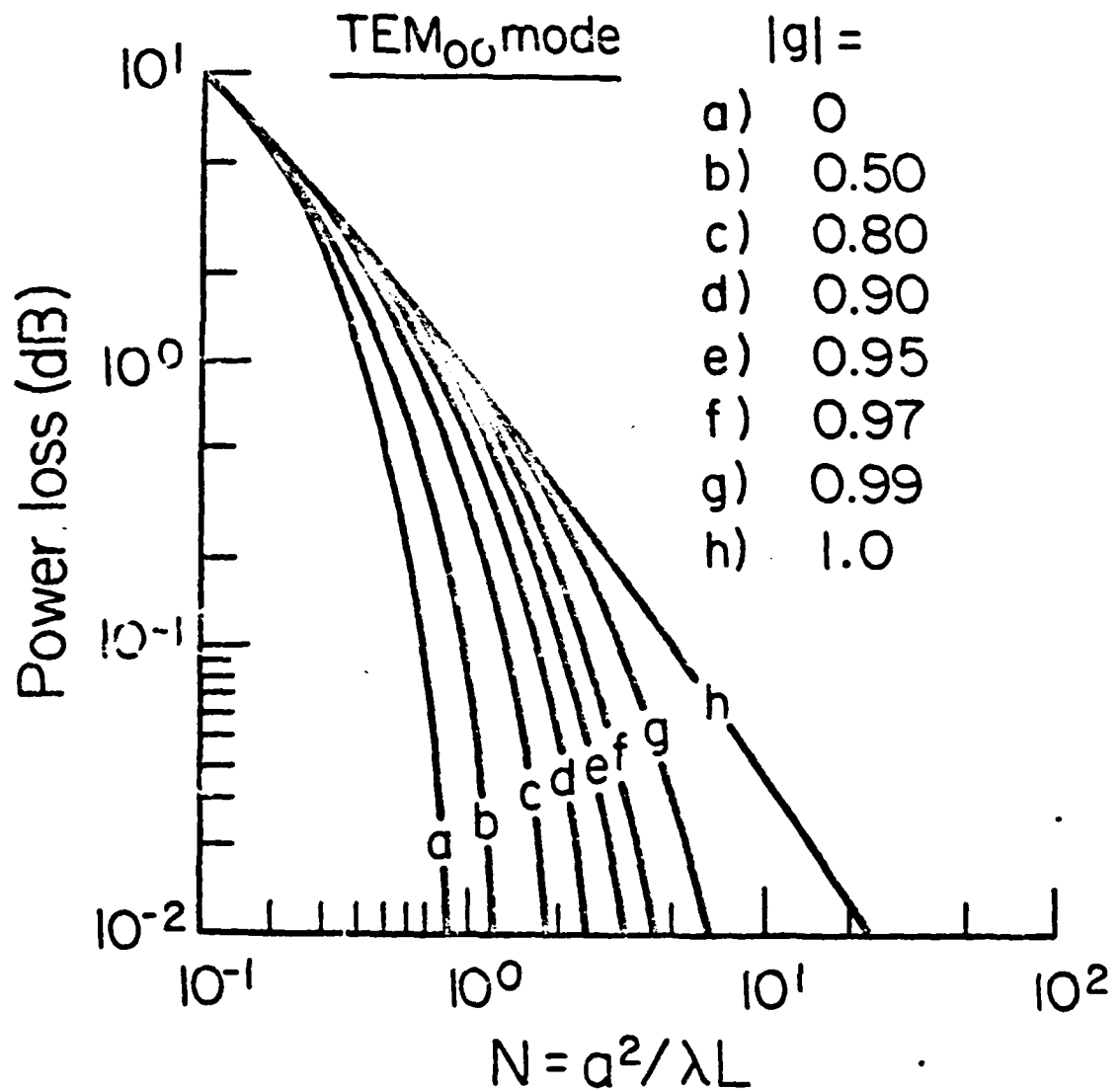


Fig. 2.7 Diffraction loss per transit for the TEM₀₀ mode of various symmetrical and stable cavities.⁽³⁾

sensitivity to mirror misalignment is related to the fact that the mode axis must be normal to each of the two mirrors. This can be satisfied only if the ray is incident along a line which passes through the center of curvature of the mirrors.

Measurements performed on various lasers have shown (see W. Koechner⁽³⁾): (1) A hemispherical resonator is more sensitive to misalignment than a resonator with two curved mirrors. (2) The confocal resonator is far more forgiving for mirror misalignment than the other types. (3) The alignment tolerances for a concentric type resonator ($L/R = 2$) and a resonator having a large radius mirror are about the same. (4) The plane parallel resonator is the most sensitive to misalignment.

CHAPTER III

EXPERIMENTAL RESULTS

3.1 Experimental Technique

Experimental Set-Up

The experimental set-up used to lase the materials is indicated in Fig. 3.1. The pump laser was an argon ion laser from Spectra Physics, Model 170, operated in the cw mode at 514.5 nm. The pump beam is first chopped to reduce the thermal load in the laser crystal. Then, with a beam splitter, a fraction of the beam is directed to a photodiode that triggers the dual trace oscilloscope. The beam is then focused with a lens L_1 into the laser cavity. The remainder of the beam that leaves the cavity is absorbed by the filter. The output of the laser is focused with the lens L_2 into a photodiode whose output is fed into the oscilloscope.

The optical elements were aligned by superimposing their reflections with the incident pump beam. To align the beams, a pinhole was placed at the output of the pump laser to limit its size. Then the reflection from the face of the input mirror nearest to the rod was reflected back and passed through the pinhole. The reflection was observed on a screen (not shown in Fig. 3.1) after reflection by the beam splitter. Then the laser rod, the face of the output mirror nearest to the rod, and the lens were aligned following the same procedure.

The reflections from the different surfaces will interfere with the incident beam and with each other, changing the intensities of the reflected and transmitted beams. These reflections produce a coupling of the laser and pump cavities and change the reflectivity of the laser cavity mirrors. These effects are explained in terms of the properties of a Fabry-Perot resonator, so a summary of its properties will be presented. A detailed

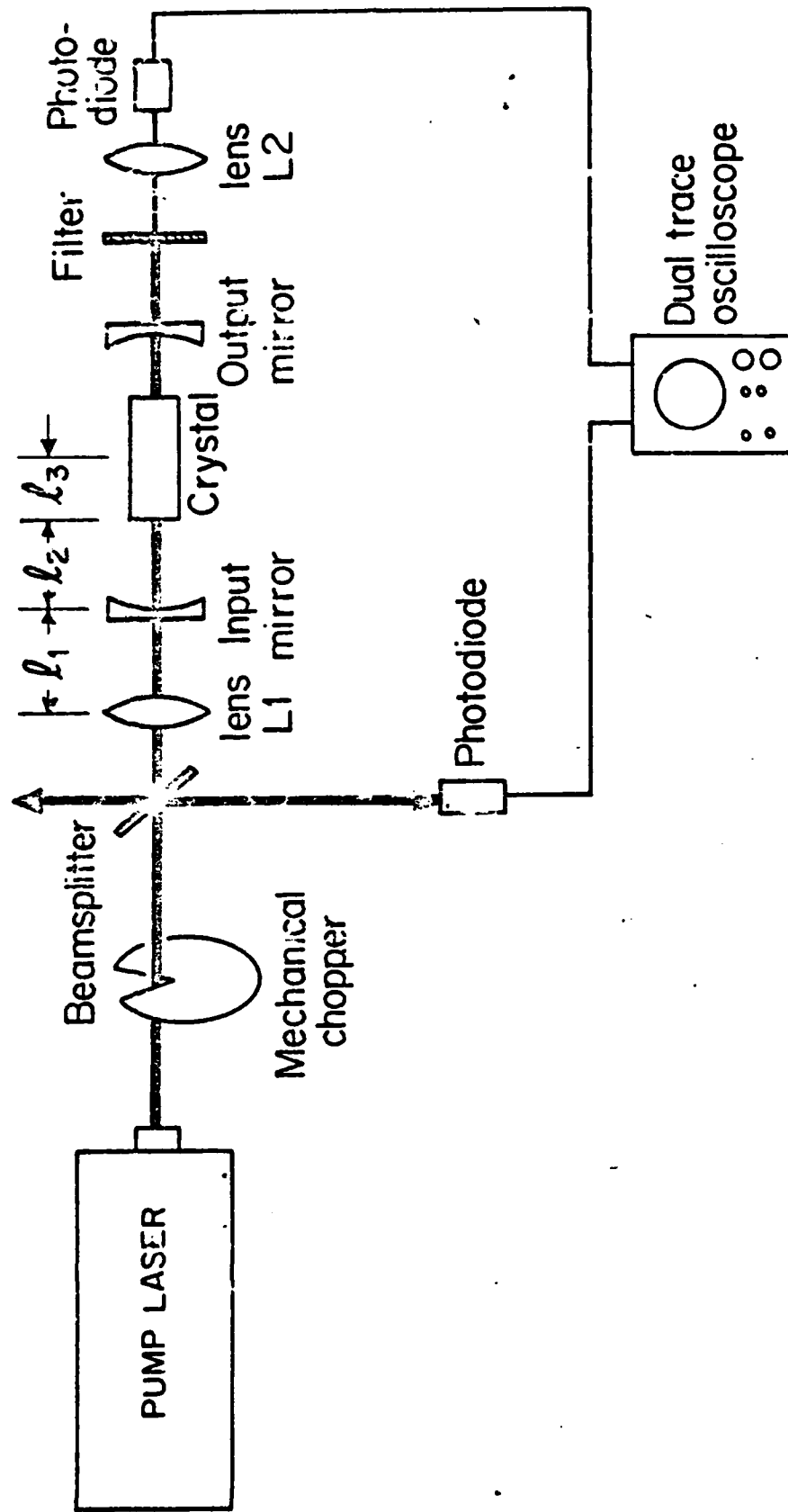


Fig. 3.1 Experimental set-up.

discussion is given in Burleigh's technical report on Fabry-Perots. ⁽¹²⁾

Fabry-Perot Resonator

A Fabry-Perot resonator consists of a plane-parallel plate of thickness L and index of refraction n . The reflectivities of the surfaces are R and r (see Fig. 3.2). Assuming plane-parallel faces and an incident plane wave, the reflectivity and transmissivity of the etalon are:

$$T = \frac{I_t}{I_i} = \frac{(1 - R)(1 - r)}{(1 - \sqrt{Rr})^2 + 4\sqrt{Rr} \sin^2(\delta/2)} \quad (3.1)$$

$$R = \frac{I_r}{I_i} = 1 - T$$

where I_i , I_r and I_t are the intensities of the incident, reflected and transmitted beams, respectively.

The phase difference δ is given by:

$$\delta = \frac{4\pi n\nu L \cos \theta}{c} \quad (3.2)$$

where θ is the angle of incidence of the incoming beam, ν the frequency of the wave and c the speed of light in vacuum.

The maximum transmissivity of the etalon occurs whenever

$$\nu_m = m \frac{c}{2nL \cos \theta} \quad m = 1, 2, 3, \dots \quad (3.3)$$

for fixed L and θ , the maximum transmission frequencies are separated by the so-called free spectral range.

$$\Delta\nu = \nu_{m+1} - \nu_m = \frac{c}{2nL \cos \theta} \quad (3.4)$$

The laser cavity, a Fabry-Perot resonator, has an infinite number of axial modes, as seen from the equation above. The number of modes

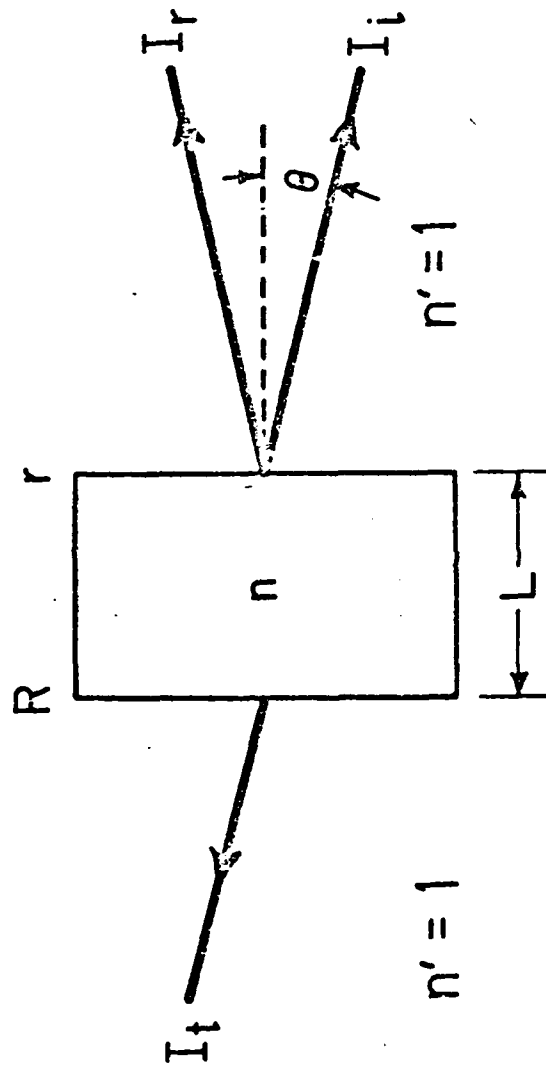


Fig. 3.2 Fabry-Perot resonator. The reflectivity of the faces is R and r . I_i and I_r are the intensity of the incident and transmitted beams, respectively.

in the laser is limited by the linewidth of the laser transition. Only those modes whose gain is above threshold will oscillate.

Summarizing, the transmission through a Fabry-Perot depends on: (1) Frequency of the incident beam. (2) Reflectivity of the faces. (3) Angle of incidence. (4) Length of the etalon.

In the next section we will discuss what are the consequences of this analysis on the reflectivity of the laser cavity mirrors.

Effective Mirror Reflectivities

The laser resonator is formed by several Fabry-Perots in tandem. The mirrors, quartz discs with a dielectric coating on one surface, form one etalon. The free spectral range of the 1 cm thick mirrors is 10 GHz. The laser rod, with uncoated faces, forms another. For a 2 cm rod with $n = 1.8$, the free spectral range is 4 GHz. Finally, a third one is the air gap, a few millimeters between the end faces of the rod and the mirror; the free spectral range is ~ 40 GHz. For Fabry-Perots in tandem, the free spectral range of the composite resonator is equal to the largest range of each of the individual etalons, i. e., in our case ~ 40 GHz.

The width of the gain at $1.06 \mu\text{m}$ for Nd:YAG at room temperature is 120 GHz. This width is larger than the free spectral range of the tandem Fabry-Perot. Therefore, the laser oscillates at the frequency for which the composite etalon has a maximum reflectivity. Due to this adjustment in the lasing frequency, the mirror reflectivity will not be that of the dielectric coated surface, but the maximum reflectivity of the tandem Fabry-Perot formed by the mirror and the air gap.

This new reflectivity, which we call "effective mirror reflectivity", is calculated in the following way. First, the maximum reflectivity of

the etalon formed by the air gap is calculated, call it R_{\max} . The total reflectivity is given by the maximum reflectivity of the etalon formed by the mirror, but now the reflectivity of the surface facing the rod is taken as R_{\max} .

Coupling of Laser and Pump Cavities

The pump beam reflected by the laser cavity re-enters the pump laser cavity, and this feedback changes the spectral properties and intensity of the beam. To analyze these effects a simple case will be studied, i.e., the coupling of the pump cavity with the input mirror.

The experimental set-up used to study this effect is shown in Fig. 3.3. The reflectivity of the coated surface of the $\frac{3}{8}$ -inch thick input mirror was 10% at the 514.5 nm pump wavelength; the other face was uncoated. The transmissivity and free spectral range are, from equations (3.1) and (3.4):

$$T_{\max} = 0.98 \quad T_m = 0.76 \quad \nu = 10 \text{ GHz}$$

A plot of transmission versus frequency is shown in Fig. 3.4.

The free spectral range of the argon laser cavity is 71.4 MHz. The doppler gain profile had a bandwidth of more than 5 GHz, so there is oscillation at more than 20 frequencies.⁽¹³⁾ When the etalon reflects the beam back into the laser cavity, it will be acting as an extra mirror. Since the free spectral range of the etalon is larger than that of the laser cavity, the frequency of the laser will be pulled towards the frequency region in which the etalon has highest reflectivity, i.e., minimum transmissivity.

Another important characteristic of the transmissivity of a Fabry-Perot is its dependence on the beam's angle of incidence. In Fig. 3.5 we

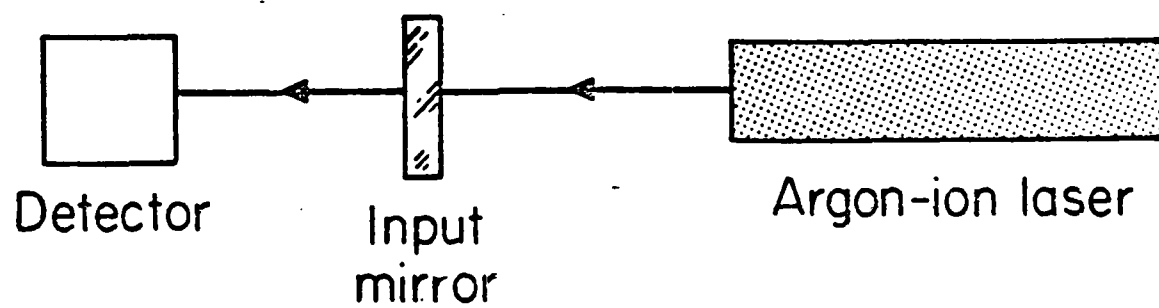


Fig. 3.3 Experimental set-up for measuring the dependence of transmission on angle of incidence.

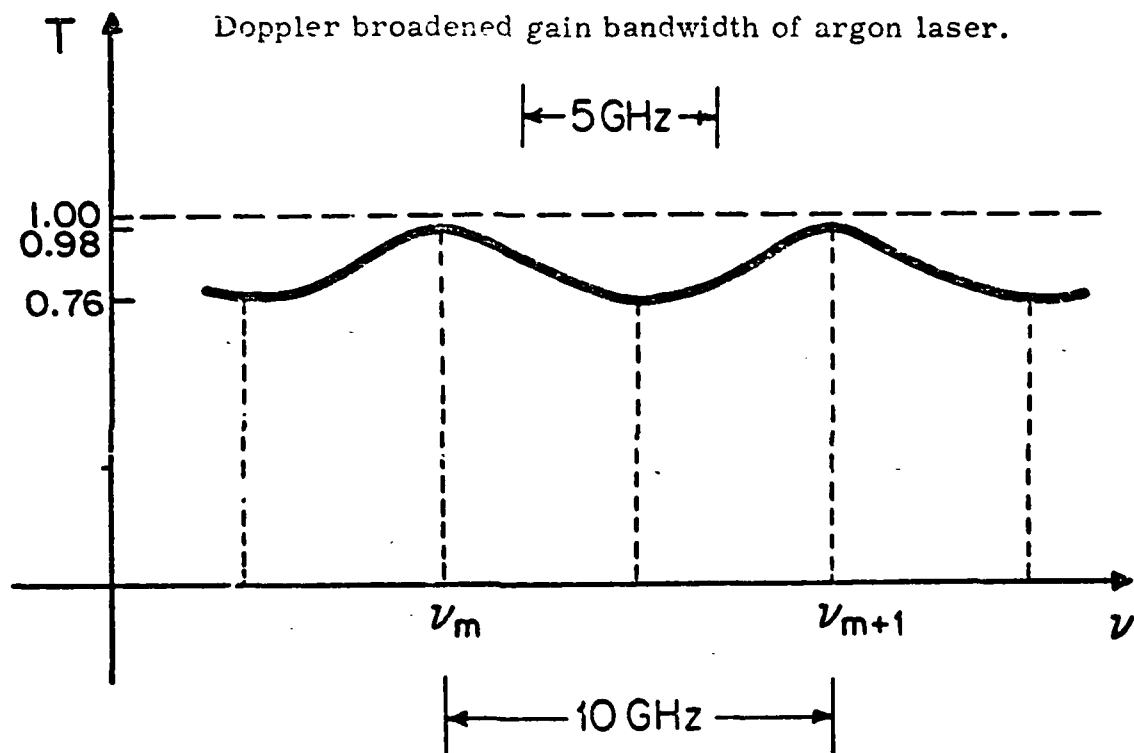


Fig. 3.4 Transmission versus frequency for the input mirror for an incident beam at the 514.5 nm wavelength.

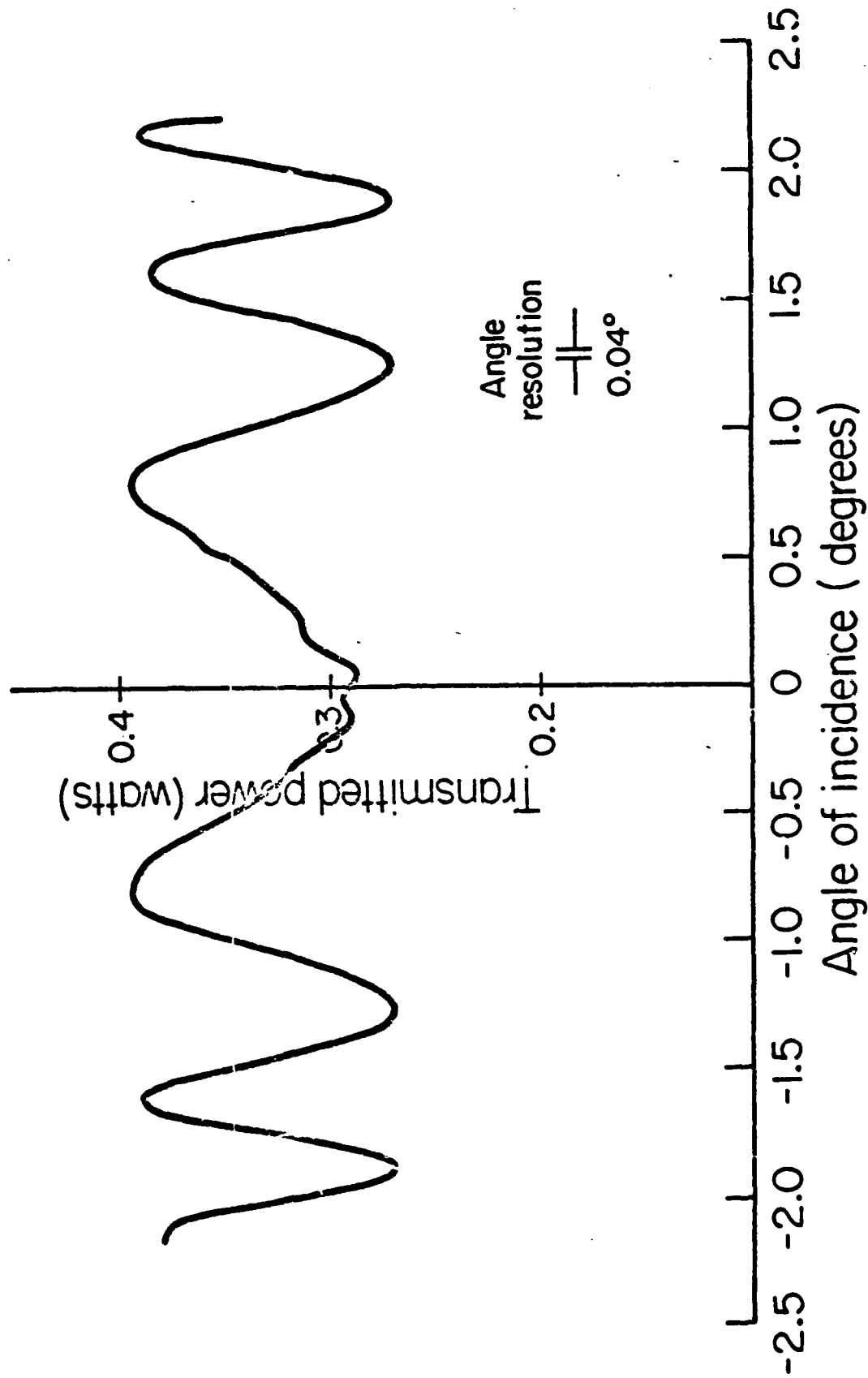


Fig. 3.5 Experimental plot of the transmitted power versus the angle of incidence.

show the experimental plot of transmitted power versus angle of incidence. The power output of the argon laser was constant (it was stabilized using a control built into the laser). For the input mirrors we are studying the calculated angle difference between the maximum and minimum transmission was 0.23° which, within the experimental error, is equal to the measured difference.

From these results we can draw the following conclusions: (1) For angles for which there is no reflection back into the laser cavity (larger than 0.10 in Fig. 3.5), the relation between transmission and angle of incidence is given by equation (3.1). (2) For small angles the beam is reflected back into the laser cavity, minimizing the transmitted intensity. This effect is explained by the frequency pulling mentioned before, that is, the laser will adjust its frequency of oscillation to the maximum mirror reflectivity. For small changes in angle of incidence the frequency at which the etalon has a maximum reflectivity will change, but the laser will readjust its frequency of oscillation to reach maximum reflectivity. This explains the flat region on the transmission curve for small angles.

The same effects will occur in the general case of reflections from the laser cavity. In this case the reflectivity will be determined by the tandem Fabry-Perot that forms the laser cavity.

Measurement of the Power Absorbed

As mentioned before, it is necessary to know the amount of power absorbed by the crystal. The following method was used. The output mirror was removed, but the rest of the elements that the pump beam crossed remained in the same position as when the cavity was lasing. Then the power of the pump beam transmitted through the rod, P_0 , was

measured. The laser rod is an etalon but, since approximately 60% of the pump beam power is absorbed in a single transit of the rod, we need consider only one internal reflection. The power absorbed, P_a , is given by:

$$P_a = \frac{1}{t} (e^{\alpha l} - 1)(1 + r e^{-\alpha l}) P_0 \quad (3.5)$$

where r and t are the Fresnel reflectivity and transmissivity of the rod end face, respectively. The factor $r e^{-\alpha l}$ is due to the reflection from the end face. This factor is small compared to 1. For example, for the Nd:YAG rod with $r = 8\%$, its value is 0.03. A linear relationship between the transmitted pump beam power and the power meter of the laser was obtained. Using this relation, the power absorbed was measured in terms of the power in the laser meter. With this technique, we do not have to measure how the pump beam intensity is changed by the etalons preceding the rod.

The power was measured with a Coherent Radiation Power Meter (Model 201). This detector was calibrated with respect to a calibrated power meter borrowed from the Spectroscopy Laboratory at M.I.T. which had an accuracy of $\pm 10\%$.

3.2 Properties of Nd:YAG and Nd:CAMGAR

Nd:YAG was lased at $1.06 \mu\text{m}$, and Nd:CAMGAR at $1.06 \mu\text{m}$ and $0.94 \mu\text{m}$. The $1.06 \mu\text{m}$ transition takes place between the $^4F_{3/2}$ and $^4I_{11/2}$ manifolds, the $0.94 \mu\text{m}$ transition between the $^4F_{3/2}$ and the upper level of the $^4I_{9/2}$ manifold. The energy level diagram for Nd:CAMGAR can be found in reference (5). The $^4F_{3/2}$ manifold is split by the crystal field into two components with the same degeneracy; for Nd:YAG the upper level transition has higher gain, for Nd:CAMGAR that of the lower

level.

The spectroscopic parameters of these materials are indicated in Table I. The Nd:YAG rod was obtained from a commercial supplier and the Nd:CAMGAR crystal used for the rod was grown by Dr. David Gabbe of M. I. T.

The stimulated emission cross sections indicated in the table were obtained by spectroscopic methods by Singh et al.⁽⁴⁾ for Nd:YAG, and by Jenssen and Aull⁽⁵⁾ for Nd:CAMGAR. These values are subject to much controversy, different authors giving values that differ much more than the claimed experimental error.⁽⁶⁾

The fluorescence light was monitored using the same experimental set-up of the laser end pumping technique, with the output mirror removed. The fluorescence lifetime was measured from the exponential decay of the fluorescence light after the end of the pump pulse.

The Nd concentration was obtained by comparing an absorption peak for the sample with that of a standard. The occupation factor of the upper laser level and the thermal lower level population were calculated from the energy of these levels. The rods were pumped with an argon ion laser at the 514.5 nm wavelength; the absorption coefficients at this wavelength were measured using a Cary 14-R spectrophotometer. Finally, we assume a quantum efficiency of unity for the transition from the pump band to the $^4F_{3/2}$ level in Nd:CAMGAR; it is unity for Nd:YAG.⁽⁹⁾

The laser rod specifications are shown in Table II. In the next paragraphs we discuss the importance of these specifications.

The importance of a good surface finish on the end faces is obvious, i. e., the scattering losses depend on it. A good surface finish was obtained by polishing with $\frac{1}{4}$ - μ m grit.

Table I
Spectroscopic Parameters of Nd:YAG and Nd:CAMGAR

Solid-State Laser Material	Stimulated Emission Cross Section, σ (cm^2)	Fluorescence Lifetime τ_2 (msec)	Quantum Efficiency η	Occupation Factor of the Upper Laser Level, f_B	Nd Concentration N_t (ions/ cm^3)	Thermal Lower Level Laser Population, N_1 (ions/ cm^3)	Absorption Coefficient α (cm^{-1})
Nd:YAG	1.06 μm transition 5.0×10^{-19}	0.24 ± 0.03	1	0.40	$1.01 \pm 0.1 \times 10^{20}$ (or 72%)	5×10^{15}	0.40 ± 0.05
Nd:CAMGAR	1.06 μm transition 8.5×10^{-20} ----- 0.94 μm transition 3.2×10^{-20}	0.31 ± 0.03	1	0.64	$0.91 \pm 0.1 \times 10^{20}$ (or 1.06%)	1.06 μm transition 3×10^{15} ----- 0.94 μm transition $0.91 \pm 1 \times 10^{18}$	0.42 ± 0.05

Table II
Nd:YAG and Nd:CAMGAR Rod Specifications

	Length (cm)		Surface Finish	Surface Flatness	End Faces Parallelism	Index of Refraction n
Nd:YAG	2.17	Diameter 3 mm	$\frac{1}{4}$ μ m diamond grit	Better than $\lambda/1$	10 sec	1.8
Nd:CAMGAR	2.70	Width, 5 mm Height, 4 mm	$\frac{1}{4}$ μ m diamond grit	$\lambda/1$	1 min	1.3

The lack of parallelism and flatness of the end faces of the crystal will decrease the effective reflectivity of the cavity mirrors. This effect can be analyzed by studying the finesse of the etalon formed by the rod end face and the opposing dielectric coated surface of the mirror. The finesse can be thought of as the effective number of interfering beams involved in forming the output of the Fabry-Perot. The factors which determine the net finesse are: (1) Reflectivity of the faces of the Fabry-Perot; the reflectivity finesse F_R is given by:

$$F_R = \frac{\pi(Rr)^{1/4}}{(1 - \sqrt{Rr})}$$

where r is the Fresnel reflectivity of the end face of the rod and R that of the dielectric coated surface of the mirror. (2) Lack of flatness of the faces; the flatness finesse is given by:

$$F_F = M/2$$

where M is the fractional wavelength deviation from flatness across the beam diameter. (3) Lack of parallelism of the faces; the parallelness finesse F_P is given by the same equation as for the flatness finesse, but now M is interpreted as the fractional wavelength deviation from parallelism of the faces within the beam diameter being used.

The net finesse is given by:

$$\frac{1}{F^2} = \frac{1}{F_R^2} + \frac{1}{F_F^2} + \frac{1}{F_P^2} \quad (3.6)$$

For a mirror reflectivity of $R = 90\%$ and with the 8% Fresnel reflectivity for the faces of the rods, we obtain $F_R = 2.2$. The flatness finesse for the rods is $F_F = 12$ for a beam radius of 100 μm . As indicated before, the input mirror and front face of the rod were made parallel by overlapping the reflections of the pump beam. The parallelism that

could be achieved with this procedure was on the order of a tenth of an arc second. If the reflection from the front face of the output mirror was also overlapped with the pump beam, then the angle between the end faces of the rod will be equal to the angle between the rear face of the rod and the output mirror. For the latter case, with a beam radius of $100\text{ }\mu\text{m}$, $F_P = 9$, where the worst case, 1 minute of angle between the end faces of rod, was taken. Substituting these values in equation (3.6) we obtain $F = F_R (1 - 0.03)$, that is, the net finesse of the etalon is decreased by 3% due to the lack of parallelness and flatness of the rod faces. Thus, these two effects are negligible for the rod specifications we have.

The non-flatness of the rod end faces has another effect, i. e., if they are not flat the rod will be acting as a lens. For the rods used in the experiments the faces were concave with a radius of curvature of $3 \times 10^1\text{ m}$, which implies that the rod had a focal length of $2 \times 10^1\text{ m}$. The change in the laser cavity characteristics produced by this focal length is negligible.

3.3 Results

Nd:YAG and Nd:CAMGAR were lased at $1.06\text{ }\mu\text{m}$ using three different types of cavities: confocal, hemispherical and plane parallel. Nd:CAMGAR was lased at $0.94\text{ }\mu\text{m}$ using a plane parallel cavity.

The specifications for each one of the cavities are indicated in Table III. The pump beam and laser beam waists were calculated assuming that the laser rod is acting as a passive element of the cavity.

First, a qualitative discussion of the characteristics of the different cavities will be given. It was found that the most important limitation of the laser end pumping technique is the precision with which

Table III
Laser Cavity Specifications

Type	Length	Mirrors, Radius of Curvature	Laser Beam Waist	Pump Beam Waist
Confocal	10.9 cm	10 cm	0.13 mm	0.14 ± 0.02 mm
Hemispherical	6.1 cm	Output mirror 10 cm; Input flat	At the input mirror, 0.13 mm; at the output mirror, 0.21 mm	0.12 ± 0.02 mm
Plane-parallel	3.2 cm	Flat	-	0.12 ± 0.02 mm

the laser and pump beams can be aligned. The power absorbed at threshold was measured for different mirror reflectivities for each one of the cavities. Using equation (2.14) the cross sections and losses were determined.

After lasing the material, the orientation of the mirrors was adjusted to obtain the minimum possible power absorbed at threshold. The confocal cavity was the most tolerant to mirror misalignment. If the pump power was well above threshold, i. e., twice its value, it was possible to change the orientation of the mirrors by a few tenths of a degree and still obtain lasing. The plane parallel cavity was very sensitive to misalignment; even when lasing well above threshold, a change of 1/10 of a degree was enough to prevent lasing. The hemispherical resonator had a sensitivity intermediate between the other two.

For the confocal cavity a 70% variation in the pump power at threshold could be obtained for different experiments, using the same experimental set-up and alignment process. The plane parallel cavity was more reliable; a difference of only 10% was found between different experiments. The hemispherical cavity had characteristics intermediate between the other two.

In Figs. 3.6, 3.7 and 3.8 we present the graph of the power absorbed at threshold versus $-\ln R_1 R_2$ for the plane-parallel, hemispherical and confocal cavities; R_1 , R_2 are the effective mirror reflectivities. The power absorbed at threshold for each set of mirrors was obtained from the plot of power output versus power absorbed. The values plotted correspond to the minimum values obtained for the pump power absorbed at threshold. In Table IV we present the coefficients of equation (2.14). Using nearly the maximum power output of the argon

laser, Nd:CAMGAR was lased at $0.94 \mu\text{m}$ with high reflectivity plane-parallel mirrors. The power absorbed at threshold was 2.8 ± 0.02 watts and $-\ln R_1 R_2 = 0.001$. These results will be analyzed in the next chapter.

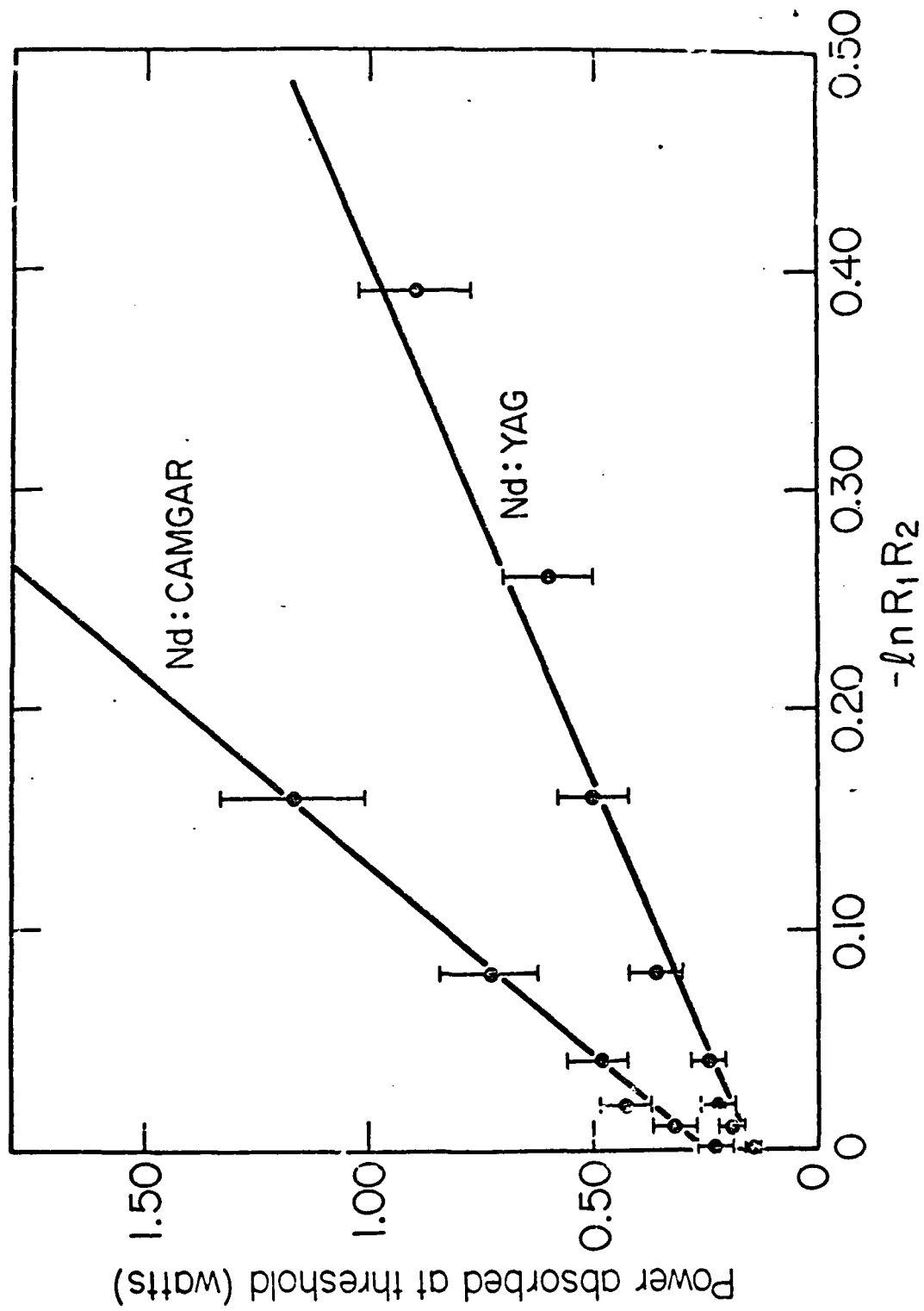


Fig. 3.6 Power absorbed at threshold versus $-\ln R_1 R_2$ for a plane-parallel cavity.

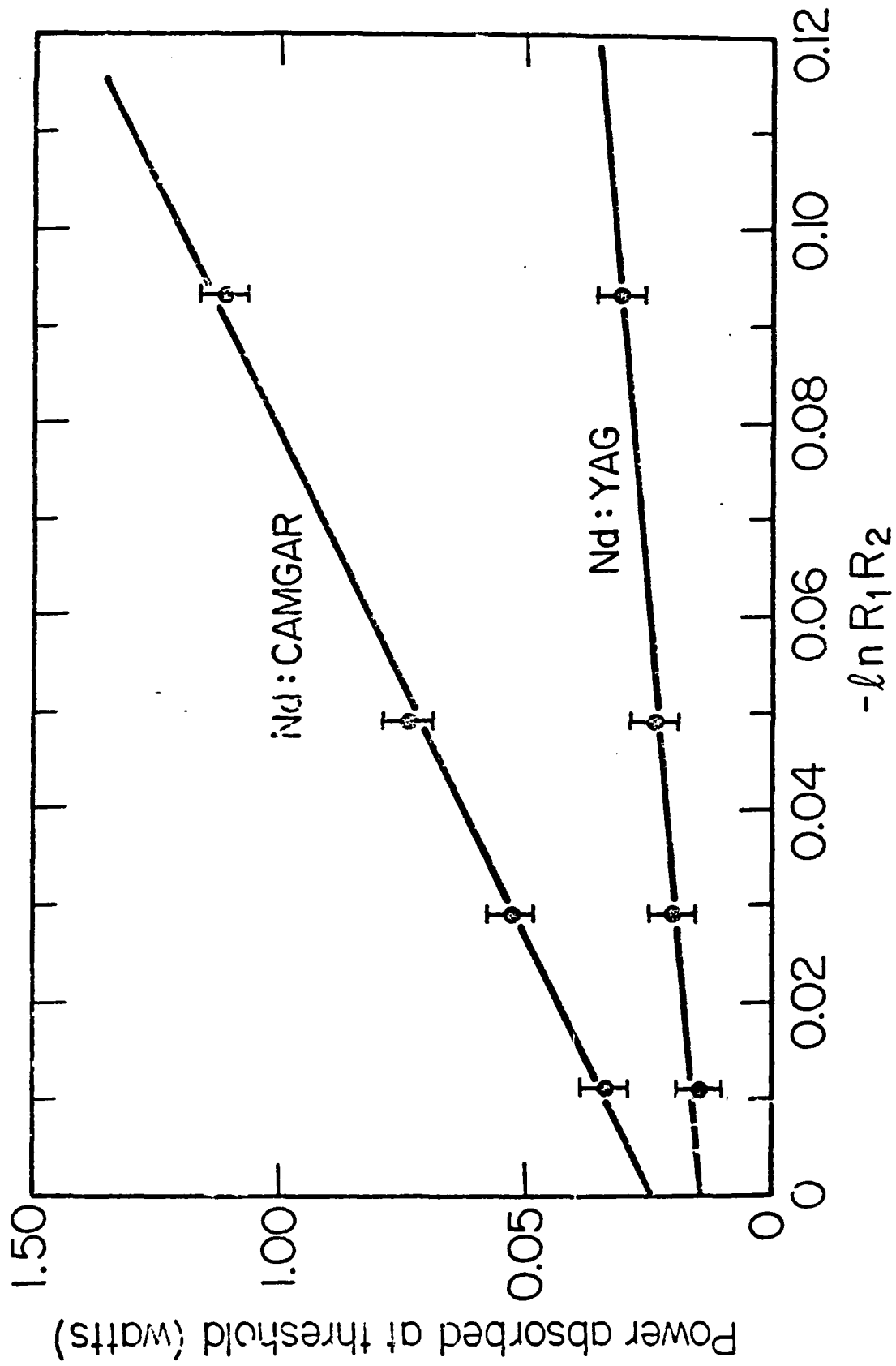


Fig. 3.7 Power absorbed at threshold versus $-\ln R_1 R_2$ for a hemispherical cavity.

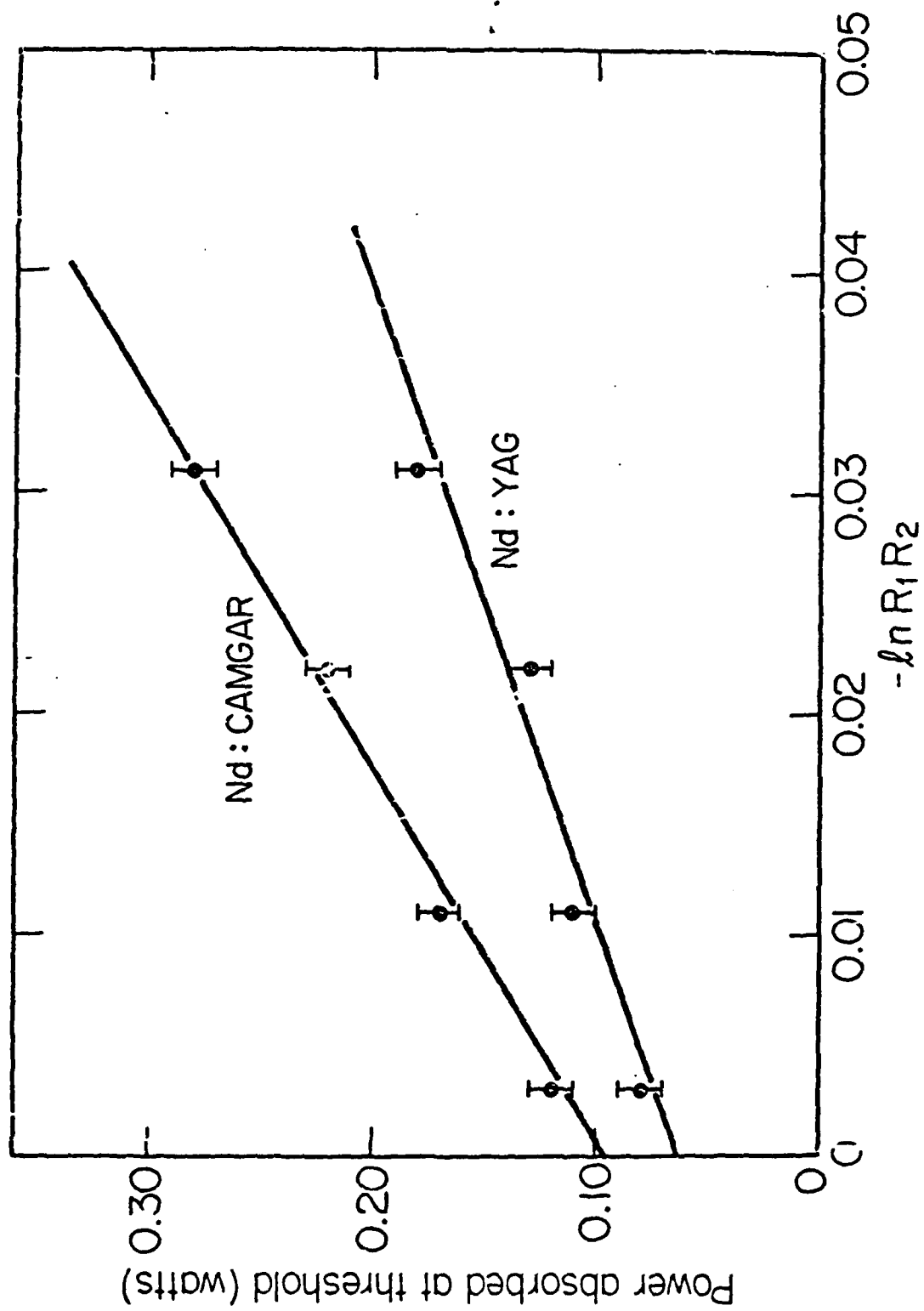


Fig. 3.8 Power absorbed at threshold versus $-\ln R_1 R_2$ for a confocal cavity.

Table IV

Slope and Intercept of the Line Fit to the Experimental P_{ath} versus
 $-\ln R_1 R_2$ for Nd:YAG and Nd:CAMGAR Lased at $1.06 \mu\text{m}$

Cavity Type	Laser Material	$\frac{h\nu A}{2\sigma\tau_2 f_B \eta}$ (watts)	$\left[\frac{h\nu A}{\sigma\tau_2 f_B \eta} \right] \Delta$ (watts)
Confocal	Nd:YAG	3.5 ± 0.5	0.06 ± 0.01
	Nd:CAMGAR	6.0 ± 0.9	0.095 ± 0.01
Hemispherical	Nd:YAG	1.7 ± 0.6	0.15 ± 0.05
	Nd:CAMGAR	9.4 ± 1.3	0.25 ± 0.05
Plane-parallel	Nd:YAG	2.1 ± 0.4	0.15 ± 0.05
	Nd:CAMGAR	5.8 ± 0.8	0.26 ± 0.05

CHAPTER IV

DISCUSSION

4.1 Thermal Effects in Laser Rods

Any solid-state laser material operating in the cw mode must dissipate an appreciable amount of heat. The heat arises because:

1. The excited electrons lose their energy through non-radiative phonon transitions from the pump to the upper laser level and from the lower laser level to the ground state.
2. The quantum efficiency of the fluorescence processes involved in the laser transition is less than unity; therefore some of the photons lose their total energy to the host lattice.

Thermal effects in laser rods are brought about by a combination of heat generation due to absorption of pump radiation and heat flow due to cooling processes. Heating and cooling of the laser material leads to a nonuniform temperature of the rod, which results in a distortion of the laser beam due to a temperature and stress dependent variation of the index of refraction. The type of optical distortions which occur in a laser rod as a result of a nonuniform temperature distribution are thermal lensing and thermally induced birefringence due to the photoelastic effect of thermal strains. In addition, optical distortions can arise as a result of an elongation and bending of the rod.

Before starting with an exact calculation of the temperature distribution in the laser rod, let us make some order of magnitude calculations to find the thermal regime in which the laser is operating. The thermal

regime is characterized by the thermal relaxation time τ ; for a cylindrical rod it is given by

$$\tau = \frac{r^2}{4k} \quad (4.1)$$

where r is the radius of the rod and k the thermal diffusivity. For example, for Nd:YAG, $k = 0.046 \text{ cm}^2 \text{ sec}^{-1}$.

The relaxation time of the whole rod and of the pumped filament are the relevant times if the laser end-pumping technique is used. For example, for the Nd:YAG rod which had a radius of 1.5 mm, $\tau = 0.5 \text{ sec}$; for the pumped filament, assuming a radius equal to $\omega_0 = 100 \text{ }\mu\text{m}$, $\tau = 2 \text{ msec}$.

To calculate the temperature rise in the rod we assume a longer time period between pump pulses than the relaxation time of the rod. If the rod is in good thermal contact with a heat sink, it will return to room temperature by the time the next pulse occurs. This is equivalent to single-shot operation. The duration of the pump pulse, T , has to be longer than the fluorescence lifetime to guarantee cw operation. For example, in the experiments done we used $T = 5 \text{ msec}$.

An approximate calculation of the rise in temperature in the rod follows. Since the pump pulse is much shorter than the relaxation time of the rod, the heat generated will only have time to "spread" over a small radius. From equation (4.1) with $t = T$ we obtain $r = \sqrt{kT}$. For example, for Nd:YAG, $r \approx 150 \text{ }\mu\text{m}$ and, assuming no heat flow out of this radius, all the heat produced by the pump pulse is dissipated in this region, increasing the temperature by:

$$\Delta T = \frac{T \epsilon P_a}{c \rho \pi r^2} \quad (4.2)$$

where P_a is the power absorbed per unit length, ϵ the fraction of this power converted into heat, c the specific heat, and ρ the density. As a further approximation we take $P_a = P_0 \alpha$, where P_0 is the power incident on the crystal and α the absorption coefficient. For Nd:YAG pumped with an argon ion laser, $\epsilon = 0.52$, $\alpha = 0.42 \text{ cm}^{-1}$, $P_0 = 3 \text{ watts}$, $c = 0.59 \text{ J g}^{-1} \text{ K}^{-1}$, and $\rho = 4.56 \text{ g/cm}^3$; then $\Delta T = 1.6^\circ \text{K}$.

An exact solution will now be derived. Note that lasing action occurs during or at the end of the pump cycle; therefore the optical distortion arises from thermal gradients produced during the pump cycle and not from the heat flow as a result of cooling. So we only need the temperature distribution during the pump pulse, i.e., for the time interval $[0, T]$.

We want to find $\Delta T(r, t)$, the temperature increase as a function of the radius in the time interval $[0, T]$. To solve the problem the following assumptions will be made:

1. A uniformly pumped cylinder of radius ω_0 .
2. A rod of infinite length.
3. That during the pump pulse the radius of the heated region is much smaller than the radius of the rod. Thus we assume that the rod radius is infinite.
4. Single-shot operation, i.e., before the onset of the pump pulse the rod is at room temperature.

The two-dimensional heat equation satisfied by $\Delta T(r, t)$ is:

$$\frac{\partial \Delta T}{\partial t} = k \left[\frac{\partial^2 \Delta T}{\partial x^2} + \frac{\partial^2 \Delta T}{\partial y^2} \right] + H(x, y, t) \quad (4.3)$$

where $H(x, y, t)$ is the heat source. Taking the two-dimensional Fourier transform of the above equation, we obtain:

$$\frac{d\Delta\tilde{T}}{dt} + k^2 \rho^2 \Delta\tilde{T} = \tilde{H} \quad (4.4)$$

where the wiggle denotes the Fourier transform of the function. The above equation was obtained by assuming that $\Delta\tilde{T}$ and all its space derivatives vanish at great distances from the origin.

Solving equation (4.4) with the initial condition $\Delta\tilde{T}(\rho, 0) = 0$, and taking the inverse transform of this solution, we obtain:

$$\Delta T(\vec{r}, t) = \frac{1}{2\pi} \int_0^t \frac{dt'}{t-t'} \int e^{-k\rho^2(t-t') - i\vec{\rho} \cdot \vec{r}} H(\vec{\rho}, t') d\vec{\rho} \quad (4.5)$$

But $F(\vec{\rho}) = e^{-k^2\rho^2(t-t')}$ is the Fourier transform of the function

$$f(\vec{r}) = \frac{1}{2k(t-t')} e^{-r^2/4k(t-t')}.$$

Using this result and the convolution theorem for Fourier transforms, we obtain:

$$\Delta T(\vec{r}, t) = \frac{1}{4\pi k} \int_0^t \frac{dt'}{t-t'} \int e^{-\frac{|\vec{r} - \vec{r}'|^2}{4k(t-t')}} H(\vec{r}', t') d\vec{r}' \quad (4.6)$$

But

$$H(\vec{r}, t) = \begin{cases} \frac{\epsilon P_a}{c\rho\pi\omega_0^2} & \text{if } 0 \leq r \leq \omega_0 \\ 0 & \text{otherwise} \end{cases}$$

And using polar coordinates we obtain:

$$\Delta T(\vec{r}, t) = \frac{\epsilon P_a}{4\pi^2 c\rho\omega_0^2 k} \int_0^t \frac{dt'}{t-t'} \int_0^{\omega_0} \int_0^{2\pi} e^{-\frac{|\vec{r} - \vec{r}'|^2}{4k(t-t')}} r' dr' d\theta' \quad (4.7)$$

From the equation we see that the temperature rise will be largest at the origin. To calculate its value we obtain for $r = 0$:

$$\Delta T(o, t) = \frac{\epsilon P_a}{c\rho\pi\omega_o^2} \left[t(1 - e^{-\frac{\omega_o^2}{4k} \frac{1}{t}}) + (\frac{\omega_o^2}{4k}) \int_{\frac{\omega_o^2}{4k} \frac{1}{t}}^{\infty} \frac{dx}{x} \right] \quad (4.8)$$

Note that if $t \rightarrow \infty$, then $\Delta T(o, t) \rightarrow \infty$, since $\int_0^{\infty} e^{-x} \frac{dx}{x} \rightarrow \infty$. For Nd:YAG we obtain $\omega_o^2/4k = 0.53$ msec, and with $t = T = 5$ msec we have $(\omega_o^2/4k)(1/T) = 0.11$ and $\int_{0.11}^{\infty} e^{-x} \frac{dx}{x} = 1.3$. Substituting these values in equation (4.8), we obtain $\Delta T(o, T) = 4^\circ K$.

Another case for which an explicit expression can be found is when $r \gg \omega_o$. Then $|\bar{r} - \bar{r}'|^2 \approx r^2$, and equation (4.7) becomes:

$$\Delta T(r, t) = \frac{\epsilon P_a}{r\pi c\rho k} \int_{\frac{r^2}{4k} \frac{1}{t}}^{\infty} e^{-x} \frac{dx}{x} \quad (4.9)$$

At this distance the rise in temperature is negligible for $t = T$. For example, take $r = 5 \omega_o$, then for Nd:YAG:

$$\Delta T(r, t) = (0.4^\circ K) \int_{11}^{\infty} e^{-x} \frac{dx}{x} < 10^{-5}$$

The temperature rise during the pump pulse is negligible for a radius larger than a few ω_o .

We now obtain the solution for $r \leq \omega_o$, which is the most important one since the maximum stresses and optical distortions occur in this region. Integrating equation (4.7) with respect to time, we obtain:

$$\Delta T(\bar{r}, t) = \frac{\epsilon P_a}{4\pi^2 c\rho\omega_o^2 k} \int_0^{\omega_o} r' dr' \int_0^{2\pi} d\theta' \int_{\frac{|\bar{r} - \bar{r}'|^2}{4k} \frac{1}{t}}^{\infty} e^{-x} \frac{dx}{x} \quad (4.10)$$

From this equation we see that, as expected, ΔT increases as t increases. For $r \leq \omega_0$ and $t = T$, we have $\frac{|\bar{r} - \bar{r}'|}{4k} \frac{1}{T} \leq \frac{\omega_0^2}{4kT}$. Since, for Nd:YAG, $\omega_0^2/4kT = 0.4$, the time integral can be approximated by:

$$\int_{\frac{|\bar{r} - \bar{r}'|}{4k} \frac{1}{T}}^{\infty} e^{-x} \frac{dx}{x} = \int_{\frac{|\bar{r} - \bar{r}'|}{4k} \frac{1}{T}}^1 \frac{1-x}{x} dx = -\ln \left[\frac{|\bar{r} - \bar{r}'|^2}{4k} \frac{1}{T} \right] + \left[\frac{|\bar{r} - \bar{r}'|^2}{4k} \frac{1}{T} - 1 \right]$$

But $\ln x \approx (x - 1) - \frac{1}{2}(x - 1)^2$, so

$$\int_{\frac{|\bar{r} - \bar{r}'|}{4k} \frac{1}{T}}^{\infty} e^{-x} \frac{dx}{x} \approx \frac{1}{2} \left[\frac{|\bar{r} - \bar{r}'|^2}{4kT} - 1 \right]^2 = \frac{1}{2} \left[\frac{r^2 + r'^2 - 2rr' \cos \theta'}{4kT} - 1 \right]^2$$

Substituting this equation in equation (4.10), we obtain:

$$\Delta T(r, t) = \frac{\epsilon P_a}{8\pi c \rho k} \left\{ \left[1 - \frac{\omega_0^2}{4kT} + \frac{1}{3} \left(\frac{\omega_0^2}{4kT} \right)^2 \right] + 2 \left[-1 + \left(\frac{\omega_0^2}{4kT} \right) \right] \left(\frac{r^2}{4kT} \right) \right\} \quad (4.11)$$

From this equation we see that the temperature difference depends quadratically on the radius. Using this temperature distribution we will calculate the thermal stresses and optical distortions in the rod. We start with the thermal stresses.

Thermal stresses are important because they limit the maximum power absorbed by the rod. It will be shown that the stress depends not on the power absorbed, P_a , but on the power absorbed per unit length,

and is independent of the area of the pump beam. Therefore the product $\cdot P_o \alpha$ is the factor that determines the maximum power input, where P_o is the power input.

On the other hand, the optical effects depend on the power absorbed per unit area, but not on the length of the laser rod. As mentioned before, we are interested in operating the laser with the maximum possible power absorbed per unit area. Thus these effects will play a major role in the design of the laser.

The temperature gradients generate mechanical stresses in the laser rod, since the hotter inside area is constrained from expansion by the cooler outer zone. The highest stress occurs at the center of the rod. If the temperature depends quadratically on the radius, the order of magnitude of the stress at the center of the rod is: ⁽³⁾

$$\tau = \left[-\frac{\alpha_o E}{16\pi k(1-\nu)} \right] (\epsilon P_o \alpha) \quad (4.12)$$

where α_o is the thermal coefficient of expansion, E the Young's modulus, and ν the Poisson ratio. For Nd:YAG, $\alpha_o = 6.9 \times 10^{-6}/K^{-1}$ at 300°K, $E = 3.3 \times 10^{12}$ dynes/cm², $\nu = 0.3$. With these values we obtain $\sigma = 3 \times 10^6$ dynes/cm². On the other hand, the tensile strength of Nd:YAG is 2×10^8 dynes/cm². Thus we are well below the rupture stress.

Having explored the stresses in the laser rod, we now turn to the optical distortions which are a result of both temperature gradients and stresses. As a result of these effects the laser rod will be acting as a lens in the resonator. This effect is called thermal lensing.

W. Köechner ⁽³⁾ has shown that for Nd:YAG the temperature-dependent variation of the refractive index constitutes the major contribution to thermal lensing, so we will only analyze this problem.

To illustrate the importance of this effect, consider the following example. Using a cavity with plane-parallel mirrors Nd:YAG was lased. Assuming that the laser rod is a passive element of the cavity, the limiting aperture is the pump beam. With $\lambda = 1.06 \mu\text{m}$, $a = \omega_0 = 0.1 \text{ mm}$ and the separation between mirrors, $L = 3.1 \text{ cm}$, we find that the Fresnel number is $N = 0.30$. From Fig. 2.7, with $g = 1$, we find that the power loss per pass is 4.5 dB and thus the diffraction loss per unit length 0.33 cm^{-1} . The experimental value of the losses was 0.033 cm^{-1} .

The temperature-dependent change of refractive index can be expressed as:⁽³⁾

$$\Delta n(r) = [T(r) - T(0)] \left(\frac{dn}{dT} \right)$$

From equation (4.11) we obtain:

$$\Delta n(r) = - \frac{\epsilon P_a}{4\pi c \rho k} \left[1 - \left(\frac{\omega_0^2}{4kT} \right) \right] \left(\frac{dn^2}{dT} \right) \left(\frac{r^2}{4kT} \right)$$

The focal length for a lens-like medium whose index of refraction varies quadratically with the radius is given by:⁽³⁾

$$f \approx \frac{2c\rho k}{\epsilon} \left(\frac{4kT\pi}{P_a} \right) \left(\frac{4kT}{4kT - \omega_0^2} \right) \left(\frac{dn}{dT} \right)^{-1} \quad (4.13)$$

where P_a is the total power absorbed in the rod. This expression is an approximation where it was assumed (1) that the focal length is very long in comparison to the rod length, and (2) that the pump power was absorbed uniformly along the rod axis. Note that in this equation $4kT\pi$ is the area over which the heat had time to "spread". So the focal length is inversely proportional to the power absorbed per unit area of the heated region.

The theory necessary to analyze resonators that contain optical elements other than the end mirrors has been developed by Kogelnik.⁽¹⁴⁾ The theory will be applied to the laser rod as an active element of the laser resonator. We will assume that it acts as a thin lens at the center of the cavity whose focal length is given by the equation above. For flat mirrors the stability parameters of the new resonator are:

$$g = 1 - L/2f \quad (4.14)$$

and

$$\omega_1^2 = \omega_2^2 = \left(\frac{\lambda L}{\pi}\right) (1 - g^2)^{-\frac{1}{2}} \quad (4.15)$$

The geometry of the resonator is shown in Fig. 4.1. For $f = \infty$ the resonator configuration is plane parallel, for $f = L/2$ we obtain the equivalent of a confocal resonator, and for $f = L/4$ the resonator corresponds to a spherical configuration.

Let us apply these results to the example considered before. For Nd:YAG, $\frac{dn}{dT} = 7.3 \times 10^{-6} \text{ } ^\circ\text{K}^{-1}$,⁽³⁾ and substituting the numerical values of the other constants in equation (4.13) we obtain $f \approx 2.1 \times 10^2 \text{ cm}$. Using this value in equation (4.14) we obtain $g = 0.993$. In this case the limiting aperture is the size of the thermal lens which is focusing the beam; its radius is $a = \sqrt{4kT}$. Using this value we obtain a Fresnel number of $N = 3$.

With these values of g and N and Fig. 2.7, a power loss per transit of 0.17 is obtained. This is equivalent to a diffraction loss of 0.01 cm^{-1} . This result is of the same order of magnitude as the observed losses of 0.03 cm^{-1} obtained experimentally (see Table VI).

Summarizing, the thermal effects are the following:

AD-A137 610

SPECTROSCOPIC EVALUATION OF ND(3+): CAMGAR AND
HO(3+): YLF AS 094 MICROMETERS LASERS(U) MASSACHUSETTS
INST OF TECH CAMBRIDGE A LINZ ET AL. 12 DEC 83

2/2

UNCLASSIFIED

OSP86111 N00014-78-C-0133

F/G 20/5

NL

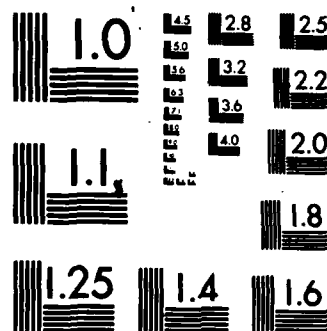
END

1

FORMED

3

DTIC



MICROCOPY RESOLUTION TEST CHART
NATIONAL BUREAU OF STANDARDS-1963-A

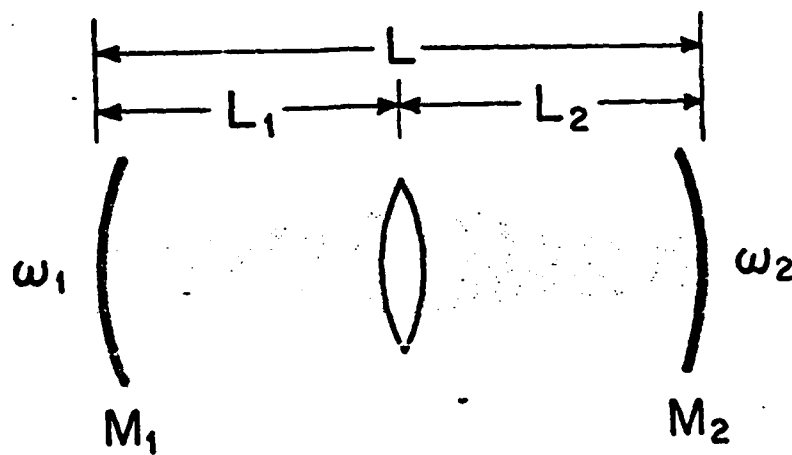


Fig. 4.1 Geometry of a cavity containing a thin positive lens. ⁽³⁾

1. The maximum power input is limited by the power absorbed per unit length and the tensile strength of the laser material; it is independent of the area of the beam.
2. The laser rod acts as a lens in the cavity due to heating by the pump beam. Its focal length is inversely proportional to the power absorbed per unit area and is independent of the length.
3. There is an optimal focal length to match the pump and laser beams. If the focal length is large the beam radius is large, and thus the diffraction losses small. But then the power absorbed per unit area is also small. Then high power is required to achieve threshold. If the focal length is small, the beam radius is small and then the diffraction losses are large. So once more high power is required to achieve threshold. Thus there is an optimum focal length for which a minimum pump power is obtained.

4.2 Measurement of the Effective Cross Section of the Laser Transition and Losses

Using the values obtained in section 3.3 and equation (2.14), the effective cross section of the laser transition and losses were calculated for Nd:YAG and Nd:CAMGAR for the different cavities at $1.06 \mu\text{m}$. These calculations were made assuming that the pump beam volume is enclosed by the laser beam volume and a uniformly pumped area of radius ω_0 . The results obtained are shown in Tables V and VI.

Nd:CAMGAR was lased at $0.94 \mu\text{m}$ with the same plane-parallel cavity used for lasing at $1.06 \mu\text{m}$. The power output of the argon laser was just enough to lase the material with high reflectivity mirrors. The power absorbed at threshold was 2.8 ± 0.2 watts for $-\ln R_1 R_2 = 0.001$.

From Table I we see that the lower level laser population, N_1 , at the $0.94 \mu\text{m}$ transition for Nd:CAMGAR is 0.91×10^{18} ions/cm³. Assuming the same losses as when it was lased at $1.06 \mu\text{m}$, the cross section was calculated using equation (2.11); its value is shown in Table V.

The scattering losses reported in the literature are on the order of hundredths of cm⁻¹; for example, for Nd:YAG, $\delta_s \approx 0.002 \text{ cm}^{-1}$.⁽³⁾ The total loss obtained for the confocal cavity was on this order of magnitude (see Table VI); thus the diffraction losses are very small for this cavity.

From Table V we see that, except for Nd:CAMGAR at $0.94 \mu\text{m}$, the values of the cross sections are smaller than those obtained from spectroscopic measurements. The large error in the value of the cross section of Nd:CAMGAR at $0.94 \mu\text{m}$ is a consequence of the fact that it was only possible to lase the material with plane-parallel cavities with high mirror reflectivities. A lower value of the cross section is not unexpected; due to the lack of overlap of the beams, part of the power absorbed is not actually used to produce a population inversion in the laser volume. Therefore the cross section will be smaller than its true value. This lack of overlap is the major source of error in the measurement. The precision could be improved if it was possible to measure the actual power absorbed in the laser beam volume. As mentioned before, we found that the cavity for which less variation occurred in the power absorbed at threshold in different experiments with the same mirror reflectivities was the plane-parallel cavity. Also, the closest overlap of pump and laser beams was obtained with this type of cavity. Therefore, the cross sections measured with this cavity are more reliable than for the others.

Table V
Effective Cross Section of the 1.06 μm Transition of Nd:YAG
and the 1.06 μm and 0.94 μm Transitions of Nd:CAMGAR

Laser Material	Estimated Emission Cross Section from Spectroscopic Measurements in cm^2	Effective Cross Section of the Laser Transition in cm^2		
		Plane-Parallel Resonator	Confocal Resonator	Hemispherical Resonator
Nd:YAG at 1.06 μm	5.0×10^{-19} (4)	$2.1 \pm 2 \times 10^{-19}$	$1.5 \pm 3 \times 10^{-19}$	$2.6 \pm 2 \times 10^{-19}$
Nd:CAMGAR at 1.06 μm	8.5×10^{-20} (5)	$3.4 \pm 3 \times 10^{-20}$	$4.2 \pm 8 \times 10^{-20}$	$2.3 \pm 2 \times 10^{-20}$
Nd:CAMGAR at 0.94 μm	3.5×10^{-20} (5)	$6 \pm 10 \times 10^{-20}$	-	-

Table VI
Total Losses for the Plane-Parallel, Hemispherical
and Confocal Cavities

Laser Material	Δ , Total Losses in a Single Transit (cm^{-1})		
	Plane-Parallel Cavity	Confocal Cavity	Hemispherical Cavity
Nd:YAG at 1.06 μm	0.033 ± 0.03	0.008 ± 0.02	0.041 ± 0.04
Nd:CAMGAR at 1.06 μm	0.015 ± 0.02	0.006 ± 0.02	0.010 ± 0.04

Another effect that will decrease the measured value of the cross section compared to the spectroscopic one is reabsorption of the laser radiation. It will occur if there is a transition from the $^4F_{3/2}$ manifold to a higher excited level and/or from the ground level to an excited level.

For Nd:YAG and Nd:CAMGAR, as seen in the energy level diagrams shown in Fig. 2.5 and reference 5, there are no levels for which a transition from the ground level to an excited level could occur at either the 1.06 or 0.94 μm wavelengths.

Reabsorption by a transition from the $^4F_{3/2}$ manifold to a higher level can occur if there are levels at the required energies. Of course, the magnitude of the reabsorption will depend on the strength of the transition. Let us see if the required energy levels exist for the materials we are studying.

Reabsorption of the 0.94 μm radiation in Nd:CAMGAR might occur if there is either a level with an energy of $22,191\text{ cm}^{-1}$ or of $22,070\text{ cm}^{-1}$. The first energy corresponds to a transition from the upper level of the $^4F_{3/2}$ manifold, and the second from the lower level. At room temperature, no absorption was obtained at the second energy (within an experimental error of $\alpha = \pm 0.05\text{ cm}^{-1}$); the absorption coefficient for the second was $\alpha = 0.14\text{ cm}^{-1}$. The absorption at the wavelength corresponding to this energy fell in the high energy side of a group of peaks. From the shape of the absorption spectra and the chart of energy levels of Nd in LaCl_3 obtained by Dieke,⁽¹⁵⁾ it was concluded that this group of peaks was due to absorption into the $^4G_{11/2}$ manifold. Therefore, the absorption at the wavelength corresponding to the $22,070\text{ cm}^{-1}$ energy is most likely due to a transition from the ground state into one of the upper $^4G_{11/2}$ levels.

For Nd:YAG, reabsorption of the $1.06 \mu\text{m}$ radiation can occur if there is either a level with an energy of $20,893 \text{ cm}^{-1}$ or of $20,805 \text{ cm}^{-1}$. The first energy corresponds to a transition from the upper level of the $^4\text{F}_{3/2}$ manifold and the second from the lower level. The absorption coefficients at the wavelengths corresponding to these energies were 0.18 cm^{-1} and 0.12 cm^{-1} , respectively. At these wavelengths, the absorption fell between two groups of absorption peaks. From the shape of the absorption spectra and Dieke's chart,⁽¹⁵⁾ it was concluded that the groups corresponded to absorption due to the $^4\text{G}_{11/2}$ and $^2\text{D}_{3/2}$ manifolds. Since the absorption spectra of these two manifolds partially overlapped, it is not possible to reach any definite conclusion about the existence of an energy level for reabsorption. It is possible that the absorption is due to the high energy levels of the $^2\text{D}_{3/2}$ manifold and so an energy level for reabsorption might exist. The issue can be solved by measuring the absorption spectra at low temperatures.

Energy levels of $20,992 \text{ cm}^{-1}$ and $20,871 \text{ cm}^{-1}$ are required for reabsorption of the $1.06 \mu\text{m}$ radiation in Nd:CAMGAR. At this wavelength the qualitative features of the spectra were analogous to the Nd:YAG spectra. Therefore, a definite conclusion about the existence of a reabsorption level cannot be reached.

The cross section measured experimentally is not the stimulated emission cross section between the upper and lower laser levels σ_{21} , but an effective cross section σ_{eff} which is related to the former by the equation

$$\sigma_{\text{eff}} \Delta N = \sigma_{21} \Delta N - \sigma_{\text{ra}} N_2 \quad (4.16)$$

where σ_{ra} is the cross section for the transition from the $^4\text{F}_{3/2}$ manifold to higher excited levels. Experimental values for σ_{ra} are not available.

It is not possible to give a good estimate of σ_{ra} because the value of σ_{21} is still subject to much controversy. Besides, the experimental errors in the measurement of σ_{eff} were large. Nevertheless we can draw some important conclusions from an estimate of its value. Take Nd:YAG as an example, and let us calculate the best case, that is, the minimum value of σ_{ra} that we could possibly obtain. To do this we take the largest value of σ_{eff} obtained for the plane-parallel-cavity within the experimental error, i.e., $\sigma_{eff} = 4 \times 10^{-19} \text{ cm}^2$. We choose the lowest value of σ_{21} given by references 4 and 6 of $5 \times 10^{-19} \text{ cm}^2$. Then from equation (4.16) we obtain $\sigma_{ra} = 1 \times 10^{-19} \text{ cm}^2$ with $\Delta N \approx N_2$. From this example we see that σ_{ra} and σ_{21} have values on the same order of magnitude. So inexact values of these cross sections or changes in the environment of the Nd ions will change the effective cross section in a significant manner. Thus, even if spectroscopic techniques have shown that a solid-state material is a good candidate for a laser, the decisive proof is the actual lasing of the material. The end-pumping technique offers such a possibility.

Finally, another effect that has not been considered is the absorption of the pump light by the $^4F_{3/2}$ manifold. The cross section for the laser transition we obtained should be larger if this effect is important. The energy level required for this absorption process is $3.1 \times 10^4 \text{ cm}^{-1}$. The energy levels of Nd in LaCl_3 have been determined by Dieke.⁽¹⁵⁾ The energy of the $^2L_{7/2}$ level is close to this value, so some absorption into this level could occur. Absorption of the pump radiation by the upper laser level will decrease the fraction of the pump power absorbed that is used to build up the population inversion. This effect can play an important role if the cross section for absorption is large. For example,

consider Nd:YAG lased with the plane-parallel cavity. In this case $\delta = 0.033 \text{ cm}^{-1}$ and with high reflectivity mirrors, $-\ln R_1 R_2 = 0.001$, we obtain from the laser threshold equation (1.7) a population of the ${}^4F_{3/2}$ manifold of $9 \times 10^{16} \text{ ions/cm}^3$. Assuming that the cross section for the transition from the ${}^4F_{3/2}$ manifold to the level whose energy is $3.1 \times 10^4 \text{ cm}^{-1}$ is $\approx 10^{-2} \text{ cm}^{-1}$. The absorption coefficient at the pump wavelength without population inversion is $\alpha = 0.40 \text{ cm}^{-1}$. Thus approximately 10% of the pump power will be absorbed by the ${}^4F_{3/2}$ population. Since the power absorbed at threshold is inversely proportional to the cross section (see equation (2.14)), if the power that was actually used to build up the population inversion is 10% lower than the power absorbed at threshold, then the cross section of the laser transition should be increased by the same percent.

The largest source of error in the calculation of the cross section is the value of the volume lased. A way to decrease this error is to calculate the ratio of the cross section of Nd:CAMGAR to Nd:YAG at $1.06 \mu\text{m}$. Then, assuming the same pumped volume, the ratio is independent of the value of the volume, as seen from the laser threshold equation. These values are given in Table VII for the different cavities. Since the thermal properties of the two crystals are different, the pumped volumes will not be equal. Nevertheless, we take this ratio as a better approximation for the cross section than the absolute value. The most reliable results were obtained with the plane-parallel resonator, so the 0.16 ratio is more reliable than the others.

4.3 Stability and Sensitivity of Laser Cavities

In this section we will determine which is the best type of cavity to be used with the laser end-pumping technique. But first, let us see how

Table VII

Ratio of the Cross Section of Nd:YAG to Nd:CAMGAR
at 1.06 μm for the Plane-Parallel, Hemispherical
and Confocal Cavities

Spectroscopic Measurements	0.17
Plane-Parallel Cavity	0.16
Hemispherical Cavity	0.09
Confocal Cavity	0.28

the power absorbed can be reduced by decreasing the laser beam waist.

The population inversion at threshold is proportional to the power absorbed per unit area. Then, if the pump power output is not large enough to obtain lasing, the beam area can be reduced to obtain the required population inversion. Therefore, a cavity for which a small beam area can be obtained is desirable. For a given mirror radius of curvature, the concentric and hemispherical cavities have a smaller waist than the confocal cavity. But this is not a disadvantage of the latter since, by choosing cavity mirrors with small radius of curvature, a small beam waist is obtained (see equation (2.19)). If the radius of the rod is decreased, then also the length of the confocal cavity has to be decreased. Thus the length of the rod limits the minimum radius that can be used.

For a plane-parallel cavity the beam waist is determined by thermal lensing. The focal length of the thermal lens determines the beam radius at the mirrors through equations (4.14) and (4.15). Assuming that the rod is acting as a thin lens, the beam radius of the mirrors, ω_{12} , is related to the beam radius of the center of the rod, ω_0 , through equation (2.15) with $z = L/2$. From these equations we obtain:

$$\omega_0 \approx \omega_{12} \approx \left(\frac{\lambda}{\pi} \sqrt{fL} \right)^{\frac{1}{2}} \quad (4.17)$$

if $\frac{\lambda L}{2} / \pi \omega_0^2 \ll 1$ and $\frac{L}{f} \ll 1$. For example, for Nd:YAG we obtain $\omega \approx 3 \times 10^2 \mu\text{m}$.

From equation (4.17) we see that the beam radius could be decreased by shortening the focal length. From equation (4.13) we see that it is not possible to reduce the focal length of the thermal lens since all the quantities appearing in the equation are parameters

characteristic of the laser material, except for the factor $4kT/(4kT - \omega_0^2)$. But for any ω_0 smaller than $4kT$ this factor will never be less than unity.

Summarizing, we see that the confocal cavity is better than the plane-parallel cavity because the laser beam radius can be made smaller.

Now let us analyze the diffraction losses of laser cavities. This analysis will be made using the stability diagram for a passive cavity shown in Fig. 4.2. In the figure the stability parameters $g_1 = 1 - \frac{L}{R_1}$ and $g_2 = 1 - \frac{L}{R_2}$ are drawn as the coordinate axes, where R_1 , R_2 are the radiuses of curvature of the mirrors and L is the length of the cavity. All the cavity configurations are unstable unless they correspond to points lying in the area enclosed by a branch of the hyperbola $g_1 \cdot g_2 = 1$ and the coordinate axes. The points representing the confocal, hemispherical, plane-parallel and concentric resonators are given in Fig. 4.2. In this diagram the symmetrical resonators ($g_1 = g_2$) are represented by a 45° angle line. From Fig. 2.7 we see that if a stable resonator approaches the unstability region the diffraction losses increase.

If there is thermal lensing, the stability parameter g for a symmetrical cavity becomes:⁽³⁾

$$g = 1 - \frac{L}{2f} - \frac{L}{R}$$

where the approximation that the thermal lens is a thin lens of focal length f and $Rf \gg L^2$ was made.

Let us analyze how the stability properties are changed thermal lensing. (1) For the confocal cavity the stability parameter becomes $g = -\frac{L}{2f}$. Thus, the cavity remains near the origin in the

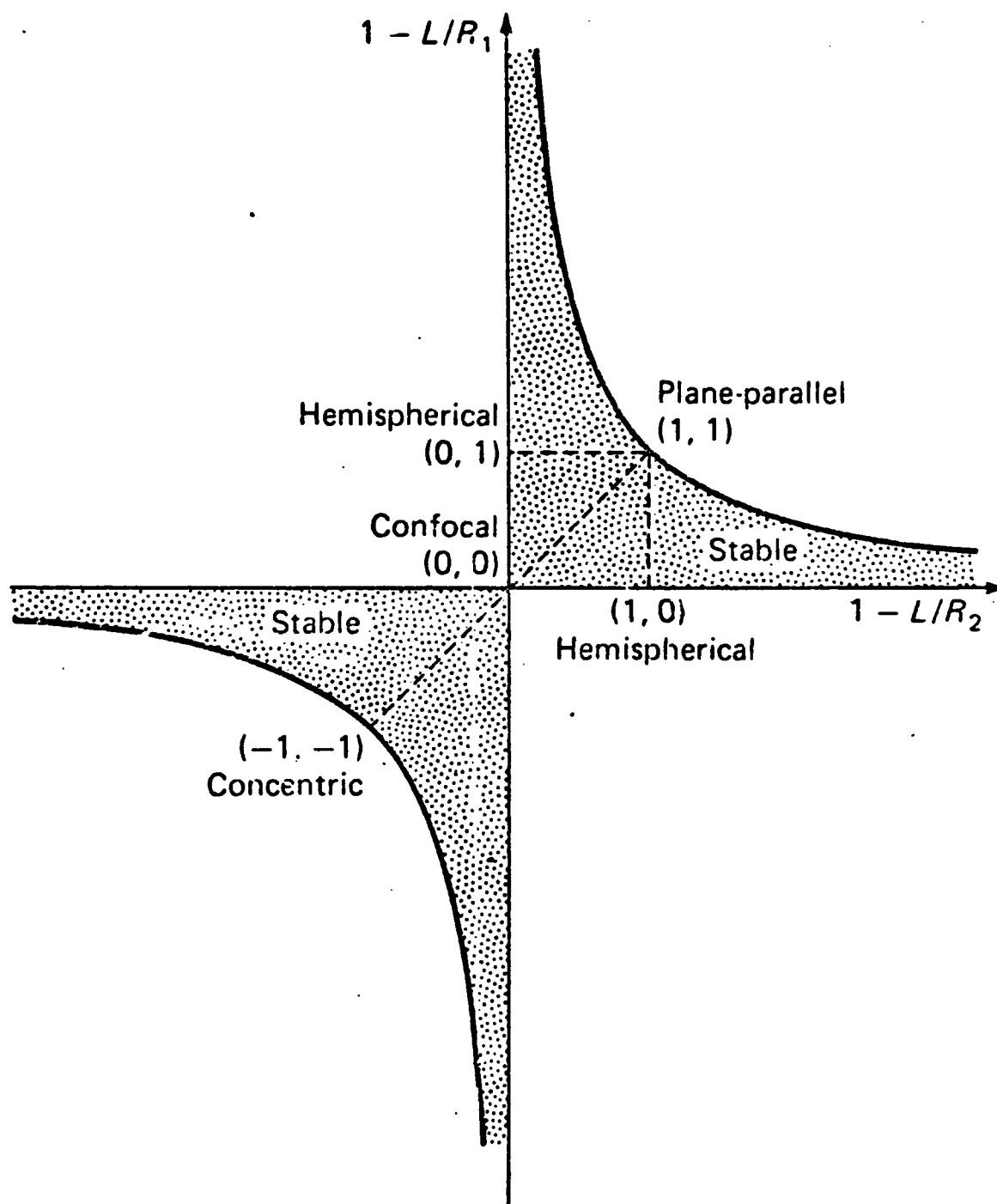


Fig. 4.2 Stability diagram for a passive laser cavity. (3)

stability diagram and the diffraction losses will be small. As shown in section 4.2, this is indeed the case. (2) The plane-parallel cavity is at a point between the stable and unstable regions. Thermal lensing makes the cavity stable, with $g = 1 - \frac{L}{2f}$. Nevertheless, the diffraction losses are still large, and therefore the total losses will also be large. This was indeed the case, as seen in Table VI. (3) The concentric cavity is also at a point between the stable and unstable regions. With thermal lensing $g = -1 - \frac{L}{2f}$; thus this effect will put the cavity in the unstable region. (4) The hemispherical cavity is also between the stable and unstable regions. For this unsymmetrical cavity the stability parameters are given by the equations: ⁽³⁾

$$g_1 = -\frac{L_1}{f} \qquad g_2 = 1 - \frac{L_2}{f}$$

where the approximation that the thermal lens is a thin lens with $f \gg L_1 L_2$ was made. L_1 is the distance from the thin lens to the curved mirror and L_2 from the thin lens to the plane mirror. From the equations above we see that g_1 will be negative and g_2 will move to the left of 1, the value it would have had if no lens had been placed in the cavity. From the stability diagram we see that the cavity moves into the unstable region. If the cavity is shortened to avoid this unstable region, the diffraction losses will still be large. This was indeed the case, as seen in Table VI.

Summarizing, we see that the confocal cavity is better than the others because it remains stable when thermal effects are considered and its diffraction losses are small.

A cavity for which alignment of pump and laser beams can be easily obtained is desirable. Alignment is important, e.g. at an angle of 1 minute

between the two beams, approximately 10% of the pump beam volume does not overlap the laser beam volume. Then the power output of the pump laser has to be increased (other factors remaining equal) by this percent to compensate for the mismatch. So a cavity for which parallelism of the beams could be achieved is desired. For the hemispherical, confocal and concentric cavities, the position and orientation of the laser beam is determined by the orientation of the cavity mirrors. For the plane-parallel cavity the position of the laser beam is determined by the pump beam itself, and the orientation is determined by the plane mirrors.

The laser power output was maximized by tilting the cavity mirrors. It might seem that this process will make the beam parallel, but it is not so for the confocal, concentric and hemispherical cavities. For example, if one of the mirrors of the confocal cavity is tilted, the laser beam is tilted, with the point at which the beam is reflected at the tilted mirror as the pivot for rotation.⁽³⁾ Hence, the fraction of the laser beam in which there is overlap with the pump beam remains approximately constant, and therefore the power output of the laser will also remain constant. A displacement of the cavity perpendicular to the beam will not be helpful either. This effect explains the variation in the pump power at threshold which we obtained in different experiments (see section 3.3). The power output depends on the initial alignment of the beam, which varied from experiment to experiment. To obtain parallelism, a rotation of the cavity is required.

For the hemispherical and concentric cavities, if one of the mirrors is slightly tilted the entire laser beam is displaced parallel to the cavity axis.⁽³⁾ Thus, in this sense, they are no better than the

confocal cavity.

Parallelism of the beam is easier to achieve with a plane-parallel cavity, since the laser beam is tilted by a tilt of the mirror. The disadvantage of this cavity is its sensitivity to mirror misalignment. On the other hand, the confocal cavity is the least sensitive to mirror misalignment.

Summarizing the results obtained in this section, we see that the requirements for laser operation with the end-pumping technique are best satisfied by the confocal cavity.

Finally, we calculate the pump power input if the optimal length and a confocal cavity has been used for lasing Nd:CAMGAR at $0.94 \mu\text{m}$ instead of the plane-parallel cavity. At this wavelength the optimal length is 0.26 cm (see section 2.2). If a confocal cavity of 5 cm length is used to lase the material, the beam waist will be $86 \mu\text{m}$ (see equation (2.19)). With high mirror reflectivities, i.e., $-\ln R_1 R_2 = 0.01$, and losses of 0.006 cm^{-1} , we obtain from equation (2.14) a power absorbed at threshold of 0.15 watts . The pump power incident is given by $P_i = \frac{P_{\text{ath}}}{(1 - e^{-\alpha l})} = 1.5 \text{ watts}$ with $\alpha = 0.42 \text{ cm}^{-1}$. This value is smaller than the 4 watts that can be obtained with the argon laser.

4.4 Evaluation of Nd:CAMGAR as a potential high power, Q-switched laser at $0.94 \mu\text{m}$

A limitation on the use of Nd:CAMGAR as a high power, Q-switched laser at $0.94 \mu\text{m}$ is the competition between the 0.94 and $1.06 \mu\text{m}$ transitions. The upper laser level is snared by both transitions. If the $1.06 \mu\text{m}$ transition has a larger cross section, it will deplete the population inversion. A mechanism has to be provided to selectively increase the losses at this wavelength during the Q-switched

pulse - for example, mirrors with higher reflectivity at $0.94 \mu\text{m}$ than at $1.06 \mu\text{m}$.

For Q-switched laser applications the required stored energy per unit area is $E/A \approx 1 \text{ J/cm}^2$. This value is smaller than the maximum stored energy obtained from equation (1.12), which is $E_{\text{max}}/A = 24 \text{ J/cm}^2$. The population inversion required to obtain the first value is:

$$N_2 = N_1 + \frac{E}{A} \frac{1}{h\nu l} \quad (4.16)$$

For a typical rod of length $l = 7 \text{ cm}$ and for $\lambda = 0.94 \mu\text{m}$, we obtain $N_2 = 1.6 \times 10^{12} \text{ ions/cm}^3$, where N_2 is the total population of the ${}^4F_{3/2}$ level. The whole ${}^4F_{3/2}$ population is depleted by the pulse since the relaxation time between levels of the manifold is shorter than the duration of the Q-switch pulse.

Lasing at $0.94 \mu\text{m}$ will be obtained if the gain at this wavelength is larger than that at $1.06 \mu\text{m}$. From equations (2.8) and (2.11) we obtain:

$$2L\sigma_{0.94}\Delta N - 2L[\delta_s + \sigma_{0.94}N_1] - 2L\delta_d + \ln(R_1R_2)_{1.06} > \\ 2L\sigma_{1.06}\Delta N - 2L\delta_s - 2L\delta_d + \ln(R_1R_2)_{1.06}$$

where $(R_1R_2)_{1.06}$ and $(R_1R_2)_{0.94}$ are the reflectivities at 0.94 and $1.06 \mu\text{m}$ respectively. With x as the factor by which the reflectivity of the mirror at $1.06 \mu\text{m}$ has to be decreased, compared to the reflectivity at $0.94 \mu\text{m}$, i.e., $R_{1.06} = xR_{0.94}$, the following result is obtained:

$$L\sigma_{0.94} \left[\left(\frac{\sigma_{1.06}}{\sigma_{0.94}} - 1 \right) \Delta N + N_1 \right] < -\ln x \quad (4.17)$$

The diffraction and scattering losses do not appear in the equation since they are the same at both wavelengths. Substituting the numerical values of the worst case, that is, the higher value of the cross section at $1.06 \mu\text{m}$

which was $8.5 \times 10^{-20} \text{ cm}^2$ ⁽⁵⁾, and the lowest value at $0.94 \mu\text{m}$ which was $3.2 \times 10^{-20} \text{ cm}^2$ ⁽⁵⁾, we obtain $x < 0.43$.

Thus the reflectivity of the mirrors at $1.06 \mu\text{m}$ has to be smaller than 40% of the reflectivity at $0.94 \mu\text{m}$ to prevent lasing at $1.06 \mu\text{m}$. It is possible to obtain mirrors with these specifications from commercial suppliers.

Now we check if it is possible to obtain this value of the stored energy with conventional flashlamps. Assuming that 7.5% of the electrical input to the lamp is absorbed by the crystal and, as for Nd:YAG, that 40% of the absorbed energy is converted to stimulated emission,⁽⁷⁾ the lamp input is approximately 4.5 J/cm^3 . It is possible to obtain this rating from commercial flashlamps.

There is another problem if the $1.06 \mu\text{m}$ transition has higher gain. The cavity losses before the Q-switch pulse depend on the wavelength. Then, even if they are large enough to prevent pre-lasing at $0.94 \mu\text{m}$, they might not be large enough to do so at $1.06 \mu\text{m}$. An analysis of the problem will be made with a Pockels cell as the Q-switch element.

The cell is located between a polarizer and the high reflectivity mirror, the polarizer between the cell and the laser rod. The inclusion of the polarizer is not essential if the laser radiation is polarized. The sequence of operation is as follows. During the flashlamp pulse a voltage, V , is applied to the electro-optic cell such that the linearly polarized light passed through the polarizer is circularly polarized. After being reflected at the mirror, the radiation again passes through the cell and undergoes another $\lambda/4$ retardation, becoming linearly polarized but at 90° to its original direction. This radiation is ejected from

the laser cavity by the polarizer, thus preventing optical feedback. Towards the end of the flashlamp pulse, the voltage on the cell is switched off, permitting the polarizer-cell combination to pass a linearly polarized beam without loss. Oscillation within the cavity will build up, and after a short delay a Q-switch pulse will be emitted from the cavity.

The phase shift δ and the transmitted light intensity I are related by:

$$I = I_0 \cos^2 \delta \quad (4.18)$$

where I_0 is the input light intensity. The phase shift is related to the cell voltage by the equation

$$\delta = \frac{2\pi}{\lambda} n_o^3 rV \quad (4.19)$$

where n_o is the ordinary index of refraction and r a constant characteristic of the material of the cell.

If the voltage in the cell is adjusted to have zero transmission at the wavelength λ_1 , then the phase shift at the wavelength λ_2 will be

$$\delta_2 = \frac{\pi}{2} \left(\frac{\lambda_1}{\lambda_2} \right) \left(\frac{n_{o2}}{n_{o1}} \right)^2 \quad (4.20)$$

If $\lambda_1 = 0.94 \mu\text{m}$, then the phase shift at $\lambda_2 = 1.06 \mu\text{m}$ is $\delta_2 = \frac{\pi}{2} (0.89)$ and the percentage of transmission through the Pockels cell, $\frac{I}{I_0} = 3\%$.

Assume 100% and 50% reflectivities at $0.94 \mu\text{m}$ for the high reflectivity and output mirror, respectively. If that reflectivity is reduced by 40% at $1.06 \mu\text{m}$ and, taking into account that only 3% of the reflected light from the high reflectivity mirror is transmitted, then the reflectivities of the high reflectivity mirror and output mirror at $1.06 \mu\text{m}$ are 1% and 20%, respectively. Substituting these values in equation (1.7), assuming no diffraction losses and $\sigma = 8.5 \times 10^{-20}$, we obtain $\Delta N = 5.1 \times$

10^{18} ions/cm³ and so the $^4F_{3/2}$ population at room temperature is $N_2 = 8.0 \times 10^{18}$ ions/cm³. This value is larger than the population required to store 1 J/cm²; therefore pre-lasing does not occur.

Summarizing, we see that Nd:CAMGAR at 0.94 μ m looks like a good candidate for Q-switched operation.

CHAPTER V

SUMMARY AND CONCLUSIONS

Solid-state laser materials can be evaluated using spectroscopic techniques. But even if such an evaluation indicates that the material can be lased, the definitive proof is actual lasing of the material.

Spectroscopic techniques can be used to measure the important laser parameters of the material.⁽⁵⁾ The stimulated emission cross section is the parameter which is more difficult to measure with these techniques; different values have been obtained with different techniques. For example, the values obtained by different authors^(4, 6) for the stimulated emission cross section of the 1.06 μm transition in Nd:YAG differ by 50%.

The effective gain for the laser transition is determined by the stimulated emission cross section of the laser transition and by the cross section of reabsorption of the laser radiation. For example, for a four level laser

$$\sigma_{\text{eff}} = \sigma - \sigma_{\text{ra}}$$

where σ_{eff} is the effective cross section of the laser transition, σ the stimulated emission cross section, and σ_{ra} the cross section for reabsorption of the laser radiation. σ and σ_{ra} are on the same order of magnitude and so small changes in these quantities can drastically change σ_{eff} . It can even become negative, that is, no laser operation is possible. Therefore a method for actually lasing the material and for measuring the effective cross section is required. The laser end pumping technique was studied as a method for lasing optically pumped solid-state laser materials in the cw mode and for measuring the effective cross section of

the laser transition. This technique is applicable if the absorption coefficient at the pump wavelength is small; if not, transverse pumping has to be used.

Another method that can be used to lase optically pumped solid-state laser materials is with a lamp. The major advantages of the laser end pumping technique over this method are: (1) Shorter laser rods are required. (2) In both methods the pump power absorbed has to be measured to calculate the cross section of the laser transition. This measurement can be made with more precision for the laser end pumping technique than for lamp pumping.

The maximum pump power output might be insufficient to obtain the required pump power absorbed for laser threshold operation with a given cavity. The problem could be solved by the proper choice of laser pump, rod length and laser cavity.

A large value of the following quantities is desirable in a laser pump:

1. Pump power output.
2. Absorption coefficient of the laser material at the pump wavelength.
3. Quantum efficiency for the transition from the pump level into the upper laser level.

We found that for Nd:YAG and Nd:CAMGAR an argon ion laser at the 514.5 nm wavelength is a better laser pump than a cw dye laser.

For a given laser pump, losses and mirror reflectivities, the laser rod length can be optimized to obtain laser threshold operation with minimum absorbed pump power. For example, with the argon ion laser as a pump, high mirror reflectivities and zero diffraction losses, the

optimal length for Nd:YAG and Nd:CAMGAR operated at the $1.06 \mu\text{m}$ transition is 0.83 cm. For Nd:CAMGAR operated at the $0.94 \mu\text{m}$ transition it is 0.26 cm.

To reduce the power absorbed required to obtain threshold operation, a cavity with small diffraction losses is desired. The heat dissipated by the pump beam produces thermal lensing of the laser rod. This effect determines the diffraction losses of the plane-parallel, concentric and hemispherical cavities, because they are in the boundary that separates the stable from the unstable cavities. The large diffraction losses of the plane-parallel cavity are reduced by the thermal lens. The diffraction losses of the concentric and hemispherical cavities are increased by thermal lensing. For the confocal cavity thermal lensing is not as important because this cavity is in the middle of the stability region. It was found that the confocal cavity had negligible diffraction losses.

An additional variable that can be changed is the laser beam radius in the laser rod. The population inversion is proportional to the pump power absorbed per unit area. Therefore, if the cross section of the laser beam is decreased, a larger population inversion can be obtained.

The laser end pumping technique requires overlap of pump and laser beams in the laser rod. The method used to obtain the closest overlap of the two beams is by tilting the cavity mirrors in order to maximize the laser power output for a given pump power input. Tilt of the cavity mirror produces a change in orientation and position of the laser beam. Therefore, the fraction of the laser beam volume on which there was overlap with the pump beam in the laser rod will change. The

laser power output will increase if the overlap is better and decrease if worse. On the other hand, the mirror tilt also changes the alignment of the laser cavity itself. Mirror misalignment causes an increase in the diffraction losses and, therefore, a reduction of output power. We need a cavity for which a close overlap of the two beams can be obtained and with tolerance for mirror misalignment.

The cavity that best satisfies these two requirements is the confocal cavity. It is the cavity with the highest tolerance for mirror misalignment. By tilting the cavity mirrors and rotation of the cavity it is possible to align the beams. It was not possible to rotate the confocal cavity with the experimental set-up used, so that for this case the plane-parallel cavity was better than the confocal because the position of the laser beam is determined by the pump beam. For future work a rotatable confocal cavity should be used.

Nd:YAG was lased at $1.06 \mu\text{m}$ and Nd:CAMGAR at $1.06 \mu\text{m}$ and $0.94 \mu\text{m}$, using as a pump an argon ion laser operated in the cw mode at the $514.5 \mu\text{m}$ wavelength. Both materials were lased in the cw mode at room temperature. The cross section of the $1.06 \mu\text{m}$ transition was measured from the slope of the line fit of the pump power absorbed at threshold versus $-\ln R_1 R_2$, where R_1 , R_2 are the effective mirror reflectivities. For Nd:YAG the cross section was $2.1 \pm 2 \times 10^{-19} \text{ cm}^2$ and for Nd:CAMGAR it was $3.4 \pm 3 \times 10^{-20} \text{ cm}^2$ at $1.06 \mu\text{m}$.

These cross sections are smaller than those obtained from spectroscopic measurements. The following processes might have been the cause for this behavior:

1. Reabsorption of the laser radiation.
2. Absorption of the pump radiation by the $^4F_{3/2}$ manifold.

3. The cross sections were obtained assuming that 100% of the pump power absorbed was used to build up a population inversion in the laser beam volume. Since the two beams are not perfectly aligned, only a fraction of the pump power absorbed will be actually used to build up the population inversion in the laser beam volume. As a consequence of this loss, the cross section will have a smaller value than with perfect alignment. Misalignment of the two beams is the largest source of uncertainty in the measurement of the cross section.

Nd:CAMGAR was lased at $0.94 \mu\text{m}$ with a plane-parallel cavity (only plane mirrors were available). Using almost the maximum power output of the argon ion laser, the material was lased with high reflectivity mirrors. The value of the cross section obtained from this experiment was $6 \pm 10 \times 10^{-20} \text{ cm}^2$.

In Nd:YAG and Nd:CAMGAR, the upper laser level of the $1.06 \mu\text{m}$ and $0.94 \mu\text{m}$ transitions is a level in the $^4F_{3/2}$ manifold. Therefore, competition between the two laser transitions will occur. The cross section of the $0.94 \mu\text{m}$ transition in Nd:YAG is $1.9 \times 10^{-19} \text{ cm}^2$, (3) smaller than the cross section of the $1.06 \mu\text{m}$ transition. Therefore, a mechanism has to be provided to selectively increase the losses at $1.06 \mu\text{m}$ if lasing at $0.94 \mu\text{m}$ is desired. On the other hand, for Nd:CAMGAR we found that the cross section at $0.94 \mu\text{m}$ is bigger than at $1.06 \mu\text{m}$. Since this measurement was only made on the basis of one experiment, the errors were quite large. Spectroscopic measurements give a value of $3.2 \times 10^{-20} \text{ cm}^2$ (5) for the $0.94 \mu\text{m}$ transition, which is approximately equal to the cross section at $1.06 \mu\text{m}$. A definite

conclusion cannot be reached, but if the cross section at $0.94 \mu\text{m}$ is indeed larger than at $1.06 \mu\text{m}$, then it would not be necessary to have a mechanism to selectively increase the losses at $1.06 \mu\text{m}$.

A better estimate of the cross section of Nd:CAMGAR at $0.94 \mu\text{m}$ could be obtained if it were lased with several different mirror reflectivities. This would be possible if a laser rod of the optimal length and a confocal cavity with a mirror radius of curvature of 5 cm were used.

In this thesis, the population inversion on the laser beam volume was calculated from the pump power absorbed. We made the hypothesis that 100% of the pump power is used to build up this population inversion. A method to measure this population inversion more precisely would be desirable.

REFERENCES

1. L. Esterowitz, R. Allen, M. Kruer, F. Bartoli, L. S. Goldberg, H. P. Jenssen, A. Linz, and V. O. Nicolai, "Blue Light Emission by a $\text{Pr}:\text{LiYF}_4$ Laser Operated at Room Temperature", *J. Appl. Phys.* 48, 650⁴ (1977).
2. L. F. Johnson and H. J. Guggenheim, "Laser Emission at $3\ \mu\text{m}$ from Dy^{3+} in BaY_2F_8 ", *Appl. Phys. Lett.* 23, 96 (1973).
3. W. Koechner, *Solid-State Laser Engineering* (Springer-Verlag, New York, 1976).
4. S. Singh, R. G. Smith, and L. G. Van Uitert, "Stimulated-Emission Cross Section and Fluorescent Quantum Efficiency of Nd^{3+} in Yttrium Aluminum Garnet at Room Temperature", *Phys. Rev. B* 10, 2566 (1974).
5. B. Aull and H. P. Jenssen, "Spectroscopic Evaluation of $\text{Nd}^{3+}:\text{CAMGAR}$ as a $0.94\ \mu\text{m}$ Laser", Letter Report, Department of the Navy, O.N.R., Boston, Mass. 02210.
6. T. Kushida, H. M. Marcos, and J. E. Geusic, "Laser Transition Cross Section and Fluorescence Branching Ratio for Nd^{3+} in Yttrium Aluminum Garnet", *Phys. Rev.* 167, 289 (1968).
7. W. Koechner, "Absorbed Pump Power, Thermal Profile and Stresses in a cw Pumped Nd:YAG Crystal", *Appl. Opt.* 9, 1429 (1970).
8. S. R. Chinn, J. W. Pierce, and H. Heckscher, "Low-Threshold, Transversely Excited $\text{NdP}_5\text{O}_{14}$ Laser", *IEEE J. Quantum Electron.* QE-11, 747 (1975).
9. R. A. Brandewie and C. L. Telk, "Quantum Efficiency of Nd^{3+} in Glass, Calcium Tungstate, and Yttrium Aluminum Garnet", *J. Opt. Soc. Am.* 57, 1221 (1967).
10. M. Birnbaum, A. W. Tucker, and C. L. Fincher, "CW Ruby Laser Pumped by an Argon Ion Laser", *IEEE J. Quantum Electron.* QE-13, 808 (1977).
11. A. Yariv, *Introduction to Optical Electronics* (Holt, Rinehart and Winston, Inc., 1971).
12. Burleigh Instruments Inc., "Tech Memo for Fabry-Perot Interferometry", No. FP 140 475.
13. Spectra Physics, Inc., "Model 170 Argon Ion Laser Instruction Manual", A/170 7/73.
14. H. Kogelnik, "Imaging of Optical Modes - Resonators with Internal Lenses", *Bell Syst. Tech. J.* 44, 455 (1965).

15. G. H. Dieke, Spectra and Energy Levels of Rare Earth Ions in Crystals (Wiley Interscience, New York, 1968).

END

FILMED

3-84

DTIC